# ČESKÉ VYSOKÉ UČENÍ TECHNICKÉ V PRAZE

**Fakulta stavební**

Doktorský studijní program: **STAVEBNÍ INŽENÝRSTVÍ**

Studijní obor: **Konstrukce a dopravní stavby**

## Ing. Vít Šmilauer

## ELASTICKÉ VLASTNOSTI HYDRATUJÍCÍ CEMENTOVÉ PASTY URČENÉ Z MODELŮ HYDRATACE

## ELASTIC PROPERTIES OF HYDRATING CEMENT PASTE DETERMINED FROM HYDRATION MODELS

## DISERTAČNÍ PRÁCE K ZÍSKÁNÍ AKADEMICKÉHO TITULU Ph.D.

Školitel: **Prof. Ing. Zdeněk Bittnar, DrSc.**

Praha, prosinec, 2005

# TABLE OF CONTENTS

# LIST OF FIGURES

# LIST OF TABLES

# ACKNOWLEDGMENTS

Czech Technical University in Prague

Faculty of Civil Engineering

Abstract

# Elastic properties of hydrating cement paste determined from hydration models

by Vít Šmilauer

This Ph.D. thesis attempts to apply elastic homogenization methods for the prediction of elastic properties of the microstructures of cement-based materials. The latter may be analyzed on four independent scales, based on a characteristic length criterion; C-S-H level, cement paste level, mortar level and concrete level. The thesis focuses on the cement paste level, where the majority of changes occurs during the hydration. The homogenization procedure is complicated by the fact that the liquid suspension of the cement mixture is transformed to a solid, load-bearing structure, being in the category of porous materials.

The reconstruction of cement paste microstructures is based purely on the 3D discrete hydration program called CEMHYD3D, released by NIST organization. At this level, it is possible to capture the particle size distribution, effect of cement chemical composition, curing temperature or curing water regime. Other vector models based on Avrami equation are proposed and compared on a few examples with the NIST model. The effect of various initial microstructure sizes on statistical descriptors is examined throughout. Moreover, the variations of degree of hydration among differently sized microstructures lead to the definition of reasonable sizes of representative volume element, too. A new model of C-S-H$_{LD}$ and C-S-H$_{HD}$ evolution at the microscale is presented and validated with the results from porosimetry.

Recent advances in nanoindentation provided the intrinsic elastic properties of major constituents of unhydrated and hydrated cement paste. The homogenization in this thesis is based on three approaches. The first one assumes certain special morphological configurations resulting in analytical methods as the Mori-Tanaka or the self-consistent scheme. Perfect results were obtained at the C-S-H level for upscaling from C-S-H building units. The second approach is based on the FEM where static, kinematic or periodic boundary conditions are applied. The periodic conditions were found as the best approximation of reality, even in small representative volumes. Special mesh generator accounting for the percolation in early hydration ages is designed, enabling homogenization from the final set point of the cement paste.

The third homogenization method is based on FFT transformation of periodic strain and stress fields on a periodic microstructure. Compared to FEM, field approximations are not limited by any shape functions, also no assemblage of stiffness matrix has to be carried out.

The results are mutually comparable with significant savings in both computational time and memory.

Several examples from the literature are validated showing the potential of homogenization methods. Microstructures from $C_3S$ paste as obtained from two different hydration models are compared and the differences are discussed. Beyond the homogenization of standard cement pastes, the leached cement pastes are analyzed. The mortar level is treated analytically, including the interphase transition zone around the fine aggregates. Similar approach at the concrete level leads to good estimations of elastic properties during the whole hydration period of concrete.

České vysoké učení technické v Praze

Fakulta stavební

Abstrakt

## Elastické vlastnosti hydratující cementové pasty určené z modelů hydratace

Vít Šmilauer

Tématem této práce je použití elastických metod homogenizace pro předpověď elastických vlastností mikrostruktur materiálů založených na cementu. Tyto materiály mohou být analyzovány ve čtyřech nezávislých úrovních na základě kritéria charakteristické délky: C-S-H úroveň, úroveň cementové pasty, úroveň malty a betonu. Práce se soustřeďuje na úroveň cementové pasty, kde se odehrává většina změn během hydratace. Homogenizace je komplikována faktem, že kapalná suspenze cementové směsi se mění do pevné fáze, která je schopna přenášet zatížení, a která spadá do skupiny porézních materiálů.

Vytvoření mikrostruktury cementové pasty je čistě založeno na prostorovém diskrétním hydratečním programu CEMHYD3D, poskytnutým organizací NIST. Na této úrovni je možno zachytit křivku zrnitosti, účinek chemického složení cementu, účinek teploty nebo vodního režimu. Jsou formulovány další spojité hydratační modely založené na Avramiho rovnici a porovnány na několika přikladech s NIST modelem. Účinek různých počátečních velikostí mikrostruktur na statistických ukazatelích je podrobně prozkoumán. Navíc variace stupně hydratace mezi různými velikostmi mikrostruktur vede rovněž k definici vhodných velikostí reprezentativních objemů pro simulaci. Je uveden nový model pro vývoj C-S-H$_{LD}$ a C-S-H$_{HD}$ na mikroměřítku a porovnán s výsledky z porozimetrie.

Nedávné pokroky v nanoindentaci poskytly údaje o charakteristických elastických vlastnostech hlavních složek nehydratované a zhydratované cementové pasty. Homogenizace je v této práci založena na třech přístupech. První předpokládá určitou speciální konfiguraci morfologie, která ústí do analytických metod jako Mori-Tanaka nebo "samokonzistentní" (self-constistent). Výborné výsledky byly dosaženy na úrovni C-S-H při škálování z C-S-H stavebních jednotek. Druhý přístup je založen na metodě konečných prvků, kde jsou uplatněny statické, kinematické či periodické okrajové podmínky. Periodické podmínky se nejlépe blíží skutečnému chování a to dokonce v malých reprezentativních objemech. Je vytvořen speciální generátor sítí zahrnující perkolaci v raných stádiích hydratace, který umožňuje homogenizaci již od konce tuhnutí.

Třetí homogenizační metoda je založena na Fourierově transformaci periodických polí deformací a napětí na periodických mikrostrukturách. V porovnání s metodou konečných prvků nejsou aproximace polí omezeny interpolačními funkcemi posunů ani není potřeba sestavovat

matici tuhosti. Výsledky jsou srovnatelné s podstatně menšími nároky na čas a paměť.

Schopnosti homogenizačních metod jsou ověřeny na množstvích příkladů z literatury. Miktostruktury $C_3S$ pasty ze dvou rozdílných homogenizačních modelů jsou porovnány a rozdíly vysvětleny. Kromě homogenizace obyčejných cementových past jsou analyzovány vyluhované pasty. Úroveň malty je řešena analyticky se zahrnutím přechodové zóny okolo zrn písku. Podobný přístup na úrovni betonu vede k dobrým odhadům elastických vlastností během celé hydratace.

# NOTATION

### *Material elastic properties*

$E$   Young's modulus

$\nu$   Poisson's ratio

$k$   bulk modulus

$\mu$   shear modulus

### *Tensor notation*

$\boldsymbol{u}$   first-order tensor, e.g. a displacement tensor

$\boldsymbol{\sigma}$   second-order tensor, e.g. a stress tensor

$\mathbf{C}$   fourth-order tensor, e.g. a stiffness tensor

### *Matrix algebra notation*

$\boldsymbol{r}$   vector, e.g. a displacement vector

$\boldsymbol{K}$   matrix, e.g. a stiffness matrix

### *Cement terminology*

*w/c*   water-to-cement ratio (the mass fraction of water to cement)

*w/b*   water-to-binder ratio (in case not only cement is used as a binder)

ITZ   interfacial transition zone

PSD   particle size distribution

OPC   ordinary Portland cement

CH   calcium hydroxide or portlandite

C-S-H   calcium silica hydrates

C-A-H   calcium aluminate hydrates

### *Cement chemistry abbreviation*

| | | | | | | | | | | |
|---|---|---|---|---|---|---|---|---|---|---|
| $Al_2O_3$ | = | A | $Fe_2O_3$ | = | F | MgO | = | M | $SiO_2$ | = | S |
| CaO | = | C | $H_2O$ | = | H | $Na_2O$ | = | N | $SO_3$ | = | $\overline{S}$ |
| $CO_2$ | = | $\overline{C}$ | $K_2O$ | = | K | $P_2O_5$ | = | P | $TiO_2$ | = | T |

Chapter 1

# INTRODUCTION AND STATE OF THE ART

Concrete is undoubtedly one of the most demanded, favorite and universal engineering material today. The term "concrete" symbolizes a wide range of composite materials starting from asphalt matrix and going to fly-ash mixtures. Concrete belongs to the category of porous materials where the capillary porosity may attain values up to 30 % in the case of normal hardened Portland cement paste. The next discussion will deal dominantly with the Portland cements and derived composites such as mortar or concrete. Since concrete is a complex material, a wide range of science disciplines is needed for comprehensive understanding; cement and physical chemistry, image processing techniques, modeling, computer science or mechanical engineering.

The historical origin of cement is unclear but documented that Assyrians, Babylonians, Chinese and Egyptians used clay or lime materials for constructions several thousands years BC. Around 200 BC, the Romans started to use pozzolanic volcanic ash which significantly improved material durability and for the reason that it hardened under water. Little progress occurred during the middle ages until the mid of 18th century, when John Smeaton from England discovered excellent properties of cement made from clay-rich limestone. He rebuilt Eddystone Lighthouse in Cornwall, England. Vicat prepared artificial hydraulic lime in 1812–13 from synthetic mixture of limestone and clay. Joseph Aspdin of England invented in 1824 Portland cement, named after the building stones quarried at Portland, England. Joseph Monier reinforced flower pots in 1867 with iron bars. In 1887, Henri Le Chatelier established oxide ratios for proper dosing of lime to produce Portland cement. He is considered as the founder of cement chemistry. The gypsum was introduced in 1890 in the USA to act as a retardant of concrete setting. In 1930, the entrained air is firstly used to decrease freeze-thaw damage. In 1940's Powers and Brownyard formulated macroscopic hydration model that was able to quantify hydration products and separate non-evaporable, gel, and capillary water [92]. Neville summarized the comprehensive knowledge about concrete in a famous book in 1963, reprinted and extended several times [79]. Lea from 1935 and Taylor from 1963 summarized knowledge of cement chemistry resulting in the well-known books, several times reprinted [66, 110]. The silica fume, as a pozzolanic additive, and superplasticizers were introduced in 1980's.

Concrete is a living material due to the interaction with the water, even after many years

after the placing. The process of hardening is known as hydration where calcium silicates and aluminates form hydration products, called hardened cement paste. The chemical composition of the latter differs strongly on the source composition and usually in Portland cements consists of calcium silica hydrates (C-S-H), calcium hydroxide, ettringite, and pores. The hardened cement paste determines to a great extent various resulting properties of concrete such as mechanical response or permeability. The aggregates in concrete are rather intact by surrounding reactions with an exception of detrimental alkali-silica reactions.

Today's limits of mechanical properties of concrete lie somewhere in reactive powder concrete (RPC) sometimes called ultra-high performance concrete (UHPC). Large aggregates are replaced by small steel fibers that inhibit the weak contact zone and stress concentration. Sand fraction of concrete is carefully selected in order to increase the packing of particles and under normal circumstances the maximum sand diameter is $600 \ \mu$m. As a consequence, these compact brittle materials attain compressive strength up to 800 MPa and are very durable compared to ordinary concrete. Tensile strength lies between 6–13 MPa, even maintained when a first crack occurs due to distributed steel fibers. On the other hand, the elastic properties of RPC were found for mature concrete as low as 60 GPa regardless of fiber presence [125]. The studied material behaved very closely to the isotropic state.

Generally, elastic properties limit the concrete application in large-span structures, e.g. bridges or large slabs. The modification of elastic properties during fabrication is a very difficult task and with very limited improvements, demonstrated by Fig. 1.1. The mechanism of interaction between different mechanical phases in cement paste and consequently in concrete is described by intrinsic properties that remain in narrow ranges for the variety of concretes and curing conditions [17]. Therefore, the micromechanical analysis of various concretes seems to be accurate enough worldwide.

## 1.1  *Microstructure observation*

Advances in observation techniques often coincide with the progress of understanding concrete performance and underlying principles. Some properties known from the macroscale can be found on the lower scale in the microstructure.

Concrete porosity spans typically several orders of magnitude, ranging from nanometer gel pores to the millimeter air voids. The porosity changes even the hydration was ceased and may become later refined [101]. Porosity determines to a great extent almost all of the engineering properties. For the purpose of pore or microstructure reconstruction, various techniques were used extensively. The first group that requires a dried specimen is based on intrusion, e.g. mercury intrusion porosimetry, pyknometry, gas sorption. More-advanced, non-destructive
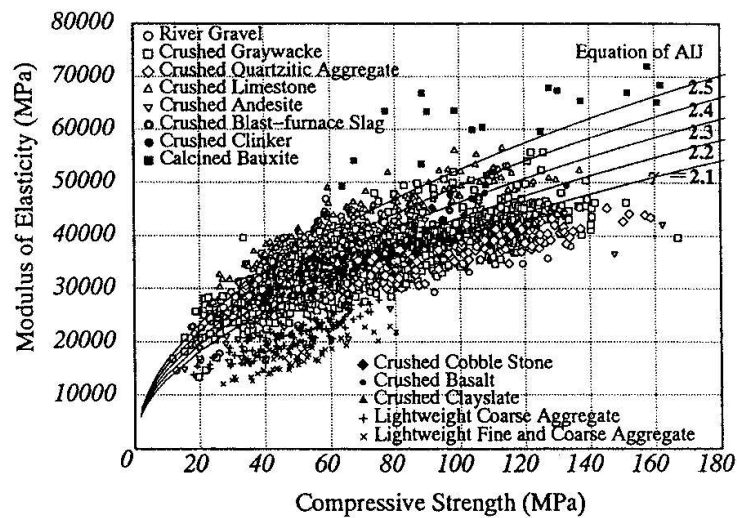
Figure 1.1: The correlation between compressive strength and modulus of elasticity for high-strength concrete [114]

methods use probing particles or fields (small-angle scattering, NMR, image analysis).

The mercury intrusion porosimetry (MIP) has been commonly used tool for obtaining pore size distribution. It was observed, that revealed pore structure does not correspond to the real structure due to inappropriate assumptions. The measured results of surface area of cement paste using porosimetry differs in the order of two magnitudes, depending on the interpretation and used intrusion agent [113]. Using the high pressures up to 300 MPa for MIP, the microstructure is often damaged. On the other hand, the gas sorption technique is reliable up to 30 nm pore size [113].

The non-destructive image analysis, based on stereological principles, came into favor later. When material is of isotropic and random nature, the 2D area is equal to the 3D volume fractions. The pioneering work of image analysis was laid down by Scrivener and Pratt [104]. The same technique was extended to access the geometric features of various chemical phases, especially within easily distinguishable unhydrated cement particles, CH crystals, C-S-H and capillary porosity [64]. Image analysis formed the basis of vector and digital hydration models and by today is very efficient in microstructure reconstruction, extended by means of statistical functions. The limit of image analysis using back-scattered electrons is around 500 nm for the cement paste. Correlation between phase amount and the microstructure was found to be in a good agreement with the Powers hydration model [53].

Small angle scattering is based either on a diffraction of neutrons (SANS) or X-rays (SAXS). The thickness of cement paste specimen is around 0.5 mm and the resolution can be in the order of nanometers or higher. The important contribution of the technique is the fact, that C-S-H

exhibit a disordered fractal structure [112]. In addition, an increase of C-S-H surface area occurs with increasing *w/c* in the range from 0.35 to 0.7 at 28 days, as opposed to a nearly constant value of $H_2O$ sorption data [101].

Nuclear magnetic resonance has been used for measuring the chain length of C-S-H. The average length increases with the higher initial amount of silica fume or fly ash [90]. The pore structure of the reactive powder concrete via NMR was found to have a fractal dimension [91].

The hydration products, often denoted as C-S-H gel, are responsible for the majority of concrete properties: strength, brittleness, elasticity, permeability, aging, shrinkage. The high surface area of hundreds of meters per gram also generates high disjoining pressures due to hindered absorbed water and is probably the origin of creep. This concept of microprestress was found successful in creep prediction models [3]. Experimental observation of Le Chatelier in 1887 noted unhydrated clinker minerals and gelatinous character of hydrates. A groups of researchers led by T.C. Powers from 1936 found the gel pore volume to be around 28 % and formulated a colloidal C-S-H model with the particle radius of 5 nm [92]. Today, the radius of C-S-H globule is estimated as 3.3 nm and the gel pore volume occupies 42 % in a low density type of C-S-H [101]. Taylor presented the layered model of C-S-H that was capable of describing a disordered structure and a pore network [110]. Brunauer thought of a sheet C-S-H structure that changes in a rolled fiber upon a lack of water, explaining the irreversible C-S-H shrinkage. Feldman and Sereda proposed a similar layered model of C-S-H made of irregular sheets [33]. According to this model, the water can re-enter the interlayer space. Although the C-S-H originate is various types of cements, physical characteristics of C-S-H are influenced to a minor extent by chemical composition [41].

Tennis and Jennings proposed a more quantitative colloid model of two C-S-H types in year 2000 [113]. Building units have approximately 5.6 nm across in the diameter. Depending on the stereological configuration and confinement during hydration, the low (LD) or high density (HD) type of C-S-H is formed. The more-opened fractal structure of the C-S-H$_{LD}$ is more permeable, unstable and with lower elastic modulus, as verified by mechanical nanoindentation of the C-S-H gel [24]. The model is consistent with various commonly used techniques for accessing the surface area, can predict the water content and density in dependence on a relative humidity. The structure of C-S-H gels is not throughout completely examined and more advanced models may show up [113].

## 1.2 Cement hydration models

The first coherent and quantitative model for the hydration of cement was deduced by T.C. Powers and his co-workers from data based on water adsorption isotherms [92]. Powers has al-

ready distinguished *capillary*, *gel* and *non-evaporable* water. Powers calculated that the 1 cm$^3$ of Portland cement under the room temperature curing produces 2.13 cm$^3$ of hydration products, on average. He stated that for the complete filling of available capillary pore space with hydration products, the *w/c* of 0.36 is the threshold value. Powers also calculated the porosity of cement gel to be 28 %. Knowing the degree of hydration or indirectly the fraction of non-evaporable water, the volumetric fractions of cement gel, gel water, non-evaporable water, unhydrated cement may be quantified. Two restraints on the hydration process were formulated

- depletion of available space for hydration products,
- insufficient water supply.

The consequence of these facts results in the maximum available degree of hydration for a given *w/c*. By today, these finding are valid for the Portland cements cured at a room temperature.

The Powers model was later refined by Feldman and Sereda [33]. All of the above-mentioned models determined to a more or less sophisticated level the volumetric fractions of cement paste components. However, the time evolution of hydration and the kinetics of ongoing processes were formulated later based on the Avrami-Erofeev and Kolmogorov-Erofeev models [2, 19]. Today, these models result in equation, referred to as Kolmogorov-Johnson-Mehl-Avrami (KJMA). These models aimed at describing the evolving crystals during recrystallization and were successfully transferred to the cement-based materials. The formulation is based on the following assumptions

- random distribution of particles in space,
- growing volume is decreased proportionally with the fraction that has already been transformed.

After mixing with water, cement undergoes dissolution and ions are immediately liberated into the pore water. A very thin layer of C-S-H surrounds now each cement grain, defending the progress of reaction. The mechanism of subsequent dormant period remains the topic of many debates and probably the secondary C-S-H growth causes the cement to thicken. Basically, the theories attempting to explain this phenomenon fall in two categories: protective coating theories and delayed nucleation theories [93, 110].

The first subclass of coating theories is based on observation that C-S-H appear in many morphological forms. Different C-S-H morphologies are linked with various permeabilities, therefore controlling the hydration progress. Jong *et al.* [56] proposed a mechanism where the C-S-H experience three phase transformations, in dependence on the CH content. Since the phase transformation is accompanied by e.g. heat flow or ion consumption, experimental data

would verify these hypotheses. However, these changes were unnoticed by many researchers, by means of chemical, physical or mechanical testing, e.g. [24, 30, 38, 93, 110], and this theory seems now to be out of date.

The osmotic pressure or membrane hypothesis belongs to the subclass of protective coating theories. Powers [92] again assumes the thin C-S-H shell around the grains, later elaborated by Double *et al.* [28]. Smaller ions, such as water or calcium, may easily diffuse through the shell but the larger silica ions remain captured. At the end of the induction period, the osmotic pressure causes a rupture of the thin shell and secondary C-S-H formation.

Delayed nucleation theories are a common name for many theories where calcium ions concentration in the solution stimulates the C-S-H growth. CH precipitates at the end of the induction period from supersaturated solution and subsidies C-S-H formation. Another insight supports a hypothesis that CH is in a metastable stage and therefore not in the equilibrium. Due to the energy barrier of nucleation, the C-S-H nucleation is delayed. Many researchers agree that calcium ions play the most important role in $C_3S$ hydration, e.g. [93, 110].

The hydration models, as a prerequisite for the microstructure reconstruction, fall in two categories: vector and discrete. Historically, the conceptually simpler vector models were found capable of microstructure and hydration kinetics predictions, e.g. $C_3S$ hydration model of Preece *et al.* [93], HYMOSTRUC by van Breugel [21], $C_3S$ model of Pignat and Navi [87] or DuCOM hydration model by Maekawa [70]. The advantage of these models was found in simplicity, computational speed and vector space; tight governing physical processes and restricted material inputs are the disadvantages.

Kondo, Taplin, Bezjak [19], Knudsen, van Breugel [21], among others, applied the KJMA equation for the simulation of cement hydration. They noted that after some hydration time, the reactions change from the boundary to the diffusion-controlled ones. A decrease of diffusion was ascribed to the densification of hydration products due to confined space. In a polyphase system, two extremes were formulated: independent hydration of components and equal fractional rates concept. The reality seems to be somewhere between and without an explicit modeling one concept remains a necessary assumption [21].

Work of De Schutter and Taerwe [103] is an example of empirical model that described a released heat of reaction. They superimposed reactions of Portland cement with slag reactions, yielding two sets of three parameters. The physical meaning of fitted parameters remains usually unclear in empirical hydration models.

Several principles from vector models were extended and the microstructure discretized enabling more local control over the physical processes and chemical reactions. Tzschichholz *et al.* [119] formulated a heterogeneous reaction-diffusion model for the setting and hydration

of cement. The physical principles of diffusion ion transport and chemical dissolution and precipitation reactions frame the model. The initial digital microstructure is used as well with the size typically between 1 and 100 $\mu$m. Having for example the reaction of C-S-H formation, the inequality of equilibrium solubility product and ion concentration determines the dissolution or precipitation of C-S-H within each volume element of the model. The dissolution reactions possess the dissolution constants of individual phases.

One of the most remarkable model is CEMHYD3D, developed in 1990's at NIST [8]. The model has provided valuable data about microstructure depercolation and found an unique relationship between the capillary porosity and percolation for the various *w/c*'s [11]. Similarly, the model found that alkali-rich cements cause sooner depercolation of microstructure thus probably the change of C-S-H morphology to the lath-like type [13].

Park *et al.* [86] used neural networks to predict kinetic parameters for another hydration model. For a clinker composition, average radius, *w/c* and cement density, the neural network predicts parameters that serve in the second stage of microstructure simulation. Any spherical particle is transformed to a cube-like shape allowing the prediction of evolving microstructure and by another fit the prediction of relative humidity.

## 1.3 Intrinsic properties

A recent development of nanoindentation provided considerable amount of intrinsic elastic values of various phases in cement-based systems, for a comprehensive summary, see e.g. [17].

Acker [1], Velez *et al.* [123] measured four clinker minerals by means of nanoindentation and resonance frequency method. All results testified the high stiffness of these synthesized or natural minerals.

Acker [1], Constantinides and Ulm [24] measured intrinsic elastic properties of various C-S-H gels. They concluded that the properties are more or less dependent on mix proportioning. Moreover, two different morphologies of C-S-H were obvious from the scatter of elastic moduli [24]. At the same time, Thomas and Jennings [112] formulated a model of both C-S-H morphologies corresponding to different globule packing.

Beaudoin [5] and Wittmann [128] measured a deflection in a three-point bending test on CH compacts with various porosities. Extrapolating to a zero porosity, they obtained consistent results with Acker [1] and Constantinides and Ulm [24]. Disregarding ettringite, the only dominant phase that exhibits anisotropic behavior is portlandite, where Laugesen determined the symmetry and stiffness tensor [65].

### 1.4  Homogenization theory

Concrete strength is the most important property in civil engineering. It is true that concrete without expected strength is useless but in many structures elastic properties are even more dominating. It is a common practice in engineering to replace highly heterogeneous concrete at nano, micro or macroscale level with a homogeneous material. A whole area of solid mechanics was developed more than forty years ago to predict effective properties of composites. Knowing the properties of individual components and their distribution in some representative volume, various techniques may be employed during the homogenization.

Almost all of homogenization theories rely on a concept of statistical homogeneity. The properties of constituents vary from place to place in a composite therefore possess a random spatial function. An "average" in the ensemble sense is defined over a sample volume of a composite. When the "average" property is independent on a location of sample volume, the medium is considered to be statistically homogeneous. Then, the "average" properties are termed as effective (in some situations apparent) over a sample volume. Such sample is usually recalled as a representative volume element (RVE), by some definitions;

> Hashin [42]: The RVE is a model of the material to be used to determine the corresponding effective properties for the homogenized macroscopic model. The RVE should be large enough to contain sufficient information about the microstructure in order to be representative, however it should be much smaller than the macroscopic body.

> Drugan and Willis [29]: The RVE is the smallest material volume element of the composite for which the usual spatially constant "overall modulus" macroscopic constitutive representation is a sufficiently accurate model to represent a mean constitutive response.

Strictly speaking, the optimal RVE corresponds to the size of studied material. In such particular case the advantage of the effective properties disappears. However, the smaller RVE than the material volume is usually analyzed and even considerably smaller volume analysis makes sense, e.g. [40, 52]. Drugan and Willis demonstrated that the RVE size may be unexpectedly small for non-overlapping identical spheres [29].

The RVE is associated with a given precision of effective properties and the size depends at least on the five parameters: physical property, contrast of properties, volumetric fractions of components, wanted precision, number of realizations [58]. To determine the appropriate RVE size, numerical studies over many realizations at the same RVE size may take place [58]. The

variance of results, depending on periodic or on other type of boundary conditions, is linked to the appropriate RVE size. Also, the effective properties on a large RVE may be replaced by many realizations on a considerably smaller one. On the other hand, the small RVE is more susceptible to the type of boundary conditions.

The transition from a heterogeneous material at a lower level to a homogeneous material at a higher level requires statistically homogeneous material, in other words an appropriate size of RVE. When $d_0$ is the smallest size under which continuum mechanics is not valid, $d$ is the characteristic length of inhomogeneities or deformation mechanisms, $l$ is the RVE size, $L$ is the dimension of the whole body of material and $\lambda$ is the fluctuation length, following inequality of length separation must be kept

$$d_o \ll d \ll l \ll L, \quad l \ll \lambda. \tag{1.1}$$

Three basic types accounting for different levels of homogenization may be applied to certain group of composites where the level separation is possible

- *micro/meso approach* - each material phase is modeled separately as discrete elements or as inhomogeneous continuum (continuum with material domains). In cement, the terminology of levels depicts the phases or materials appearing at that level: C-S-H, cement paste, mortar, concrete,
- *macro approach* - a material is considered to be a homogeneous continuum. There is no information about a lower microstructure beyond that explicitly stated,
- *multi-scale approach* - a coupled analysis is performed. Certain material locations are selected and upscaling of material properties is performed. The selection of appropriate levels must comply with Eq. (1.1).

The early homogenization theories considered only the volumetric fractions, in today terms so called one-point probability functions [117]. In 1887 Voigt introduced the first theory of "law of mixtures" corresponding to a parallel configuration of phases, assuming perfect bonding among them. Reuss in 1929 formulated the second mixture theory that represents a serial configuration of phases. These bounds lie usually far apart and the aim was to narrow them. Moreover, it was found that the assumption of equal stress violates continuous displacements on the interface among phases in general.

Hill is often considered as a founder of a continuum mechanics [49]. He proved by using various energy considerations that Voigt and Reuss assumptions lead to the lower and upper bounds on $k$ and $\mu$. In addition, Hashin and Shtrikman [44] developed closer bounds using

variational principles, adding an assumption of statistically isotropic and homogeneous material. Walpole removed an assumption of the well-ordered materials in terms of their moduli [120].

Next analytical group of homogenization methods relies on the Eshelby finding in 1957 that the stress field is uniform in an ellipsoidal inclusion when the far applied stress is also uniform [31]. Inclusion and host strains are therefore in algebraic relation. This led consequently to an improvement of dilute approximation theories, resulting in effective-medium approximations, e.g. matrix-inclusion morphologies. There are, to mention a few of them, the explicit Mori-Tanaka method [75], the implicit self-consistent scheme of Hershey and Kroner, later elaborated by Hill [51] or the explicit Kuster-Toksöz scheme [63]. The real microstructure configuration may be improved by selecting an inclusion shape in the form of sphere, ellipsoid, disc or penny-like cracks [18].

## 1.5  *Elastic homogenization of cement composites*

The hydrating cement paste is a very porous medium at the beginning, exhibiting high material contrast values with governing percolation characteristics. Therefore, the homogenization process and the RVE size need a special caution and a careful treatment.

The goal of this work is to explore an application of homogenization techniques to the cement paste and consecutive composites such as mortar and concrete in a linear elastic regime. This topic was analyzed rarely at the microscale level since both the hydration models and homogenization rely on the availability of models. De Schutter and Taerwe [102], among others, described a relationship of compressive strength and elastic properties to the degree of hydration in various concrete samples. A notice must be carried out about a measurement of the elastic properties. At the structural level, the elastic properties are often recalculated from a secant modulus after a short time load where also short-term creep takes place. Therefore, the experimental data from such measurements underestimate the true instantaneous elastic behavior, notable especially at early ages.

The Young's modulus is very often found to be linear with the degree of hydration, in a wide *w/c* and types of cement paste [32, 109]. Till today, explanation and possible mechanism of this phenomenon were proposed by only a few researchers and are based only on hydrating phase [32]. The linearity is astonishing when we consider porous evolving material with the solid phases having the maximal difference among elastic moduli by approximately five, Tab. 4.3, not talking about curing, water availability or temperature. The elastic behavior of concrete is typically time-dependent and non-linear therefore the mechanical loading at high strains is preferred. The complex interaction between the hard aggregates and soft cement paste

determines the extent of the above-mentioned phenomena. Mehta [71] postulates that the modulus of elasticity of hydrated cement paste is generally, for various porosity, between 7-28 GPa. Indeed, homogenization techniques came to similar values with the upper limit around 50 GPa [57].

Nadeau [77] formulated a micromechanical model incorporating interfacial transition zone (ITZ), aggregate size distribution and entrapped air voids. The homogenization model is of the generalized self-consistent $n$-layer type [47] where a gradient of elastic properties in ITZ is approximated by a series of constant values. Three uncoupled homogenization levels take place. The first one consists of fine aggregates, ITZ and a fraction of cement paste, the second level incorporates in addition the entrapped air, associated cement paste and ITZ, the third similarly coarse aggregates. Results from an analytical homogenization support the common observation that for a typical mature concrete the Poisson ratio is more or less invariant [77].

Recently, Bernard and Ulm [17] used simple cement hydration model for the prediction of the volumetric phases during hydration. The four-level homogenization scheme, utilizing the Mori-Tanaka and the self-consistent scheme, was able to predict elastic properties at the concrete level.

The numerical homogenization techniques exhaust generally large quantities of computer memory, resulting in a limited size of RVE. Neubauer, Jennings and Garboczi [81] analyzed the elastic and shrinkage properties of mortar in 2D. Garboczi [36] presented an application for linear elastic properties of cement paste, based on the finite difference method. Kamali *et al.* [57] examined experimentally and numerically the influence of portlandite dissolution on the elastic properties of cement paste.

It was showed in the NIST cement hydration model that the statistical fluctuation of cement microstructure does not play a major part in hydrating cement paste of the RVE size $100 \times 100 \times 100$ $\mu$m with the resolution of 1 $\mu$m in terms of hydration heat [37]. Moreover, the percolation and released heat in the digital model of the same size yielded no different quantitative behavior in many random realizations. These conclusions were found valid when the particle size distribution (PSD) is generally broad [37].

Digital resolution of the model represents a more serious problem. Generally, the resolution should be comparable with a characteristic length scale of the studied properties. The study on the effect of resolution in the NIST model concluded that the resolution strongly influences the percolation phenomena, i.e. phase connectivity, diffusion, or permeability [37]. When the resolution of NIST model has increased, the higher discrepancy with an experiment in terms of set point was observed. The authors suggested to use the resolution of 1 $\mu$m as the best resolution for percolation [37]. A very good agreement with experiments at the resolution level

of 1 $\mu$m was found for electrical conductivity measurements [85].

### 1.6 Percolation theory

The percolation theory, which topologically describes the effect of connectivity, found its application in concrete engineering as well. Randomly distributed cement grains are disconnected at the beginning, especially when certain amount of superplasticizer is present in the mixture. Since hydration products occupy more space than reactants, the side effects of expansion are connected clusters of various phases. The cluster size gradually increases on an average. When the solid cluster firstly spans across the system, sudden change of various physical properties occurs. This point is referred to as *percolation threshold of solids*, $p_c$.

Broadbent and Hammersley [22] introduced the term percolation for a fluid flow in a porous medium. In fact, they described a lattice system and showed rigorously that there is no fluid transport until certain fraction of channels is opened. This phenomenon is termed as *bond percolation* as opposed to *site percolation* where the connectivity of channel junctions is considered. Hence, the percolation $p$ is a number between 0 and 1 defined as a fraction of connected bonds or sides respectively. The differences between 2D and 3D systems as well as the geometrical configuration are summarized in, e.g. [117]. For example, the numerical results for *bond percolation threshold* for 2D squares and 3D cubes are 0.5 and 0.249 respectively. Generally, the percolation starts sooner in 3D systems since there exist more possible connection paths. This is another reason for 3D analysis of hydrating cement paste as already discussed for mortar in [12].

In the vicinity of percolation threshold, it was observed that many physical quantities exhibit a power-law scaling in the form

$$\text{Quantity} \sim (p - p_c)^{\beta}, \tag{1.2}$$

where the quantity is now considered in a geometrical sense, e.g. mean cluster size. The critical exponent $\beta$ is in geometrical case independent of microstructure details and till today the numerical analysis on bond or site percolation yield the same exponent for various geometrical cases [117]. Indeed, the critical exponent is the same for the lattice and continuum percolation in the same dimension. Moreover, in the vicinity of percolation threshold the system is invariant under scaling transformation. However, the amplitudes in the scaling laws depend on the system details and are not universal.

The physical quantity in Eq. (1.2) may be extended to effective conductivity, fluid permeability or effective Young's modulus in discrete systems, for example. Numerical analysis in

2D and 3D random system yields the critical exponent for Young's modulus of elasticity as 3.96 in 2D and 3.75 in 3D. Surprisingly, the same exponent is valid for bulk or shear modulus [115].

As already mentioned, the critical exponent of physical quantities, such as modulus of elasticity, depends on discrete or continuous type of system. The necks connecting phases approach to a singular width in a continuum around percolation threshold [34]. Feng *et al.* [34] studied Swiss-cheese (spherical voids) and inverted Swiss-cheese (spherical solid phase) percolation of overlapping spheres. They found the lowest bound for critical exponent of modulus of elasticity $\beta \sim 1.25$. Rintoul and Torquato [97] performed an extensive numerical study in the system of identical overlapping spheres, resulting in $p_c = 0.2895 \pm 0.0005$. The percolation threshold changes when the particle size distribution (PSD) is taken into account. Many authors found weak dependence on PSD, see [117] and the reference therein, but in the case of two distinct diameters the threshold lies as high as $p_c \sim 0.703$.

Boumiz *et al.* [20] measured experimentally the evolution of elastic properties on white cement pastes. Applying Eq. (1.2), he found $\beta$ for the shear modulus in the range from 1.92 to 2.13 for *w/c* in the range from 0.34 to 0.4. The definition of percolation was circumvented by the definition of critical time, from which the elastic properties emerge and the time corresponds to a critical degree of hydration; 0.015 for $w/c = 0.35$ and 0.021 for $w/c = 0.4$. More detailed study and validation across percolation will be given in section 4.2 and is in a perfect accordance with the Boumiz data [20].

Ye *et al.* [132] applied Eq. (1.2) for the estimation of elastic properties of cement pastes. For the simulation, HYMOSTRUC model of cement hydration was utilized to account for percolation [21]. They found the solid percolation threshold $p_c$ as 0.38 and 0.41 for *w/c* 0.6 and 0.41, respectively. For the accurate predictions within 300 minutes of hydration, the bulk modulus was calculated for $\beta = 1.35$ and the coefficient of linearity as 26.72 after 40 hours [132].

### 1.7 Organization of thesis

Chapter 2 reviews the basic characteristic of raw cement, describes the mechanisms of hydration of individual chemical phases. The properties of hydration products are captured for ordinary Portland cement. A concept of *degree of hydration* is introduced.

Chapter 3 presents the cement hydration models, from the most simple affinity models to the NIST discrete model based on cellular automata. The reconstruction of cement microstructure and the appropriate size for hydration is outlined and validated. The percolation in different volumes is studied as well. The new models for C-S-H$_{LD}$ and C-S-H$_{HD}$ morphology are presented and calibrated.

Chapter 4 deals generally with the theory of homogenization, describing the assumptions,

uncoupled approach of homogenization and percolation in homogenization routines. Intrinsic elastic properties of constituents are defined.

Chapter 5 explores the potential of analytical homogenization methods for the assessment of elastic properties at various levels.

Chapter 6 outlines the numerical homogenization methods via FEM loaded by eigenstrains and the FFT-based method. The implementation of percolation with mesh generation is discussed as well.

Chapter 7 validates the methods from the previous chapters and compares the results for the *w/c* in the range from 0.25 to 0.5. Plain Portland cement paste, degraded cement paste, mortar and ordinary concrete are analyzed. The bounds from different loading conditions are showed. A comparative study of the homogenized elastic values from two different hydration models is carried out. Cement pastes are analyzed for the initial equivalent stress using MHH condition of plasticity.

Chapter 8 closes the work and suggests the way of future research.

# Chapter 2

# HYDRATION OF CEMENT

## *2.1 Chemical properties*

| Compound name | Formula | Mol. weight [g/mol] | Density [g/cm$^3$] | Molar volume [cm$^3$/mol] |
|---|---|---|---|---|
| Tricalcium silicate | $C_3S$ | 228 | 3.21 *3.15* | 71 *72.4* |
| Dicalcium silicate | $C_2S$ | 172 | 3.28 | 52.4 |
| Tricalcium aluminate | $C_3A$ | 270 | 3.03 | 89.1 |
| Tetracalcium aluminoferite | $C_4AF$ | 486 | 3.73* | 128* *130* |
| Gypsum anhydrate | $C\bar{S}$ | 136 | 2.61 | 52.1 |
| Gypsum hemihydrate | $C\bar{S}H_{0.5}$ | 145 | 2.73 | 53.1 |
| Gypsum dihydrate | $C\bar{S}H_2$ | 172 | 2.32 | 74.1 |
| Ettringite (trisulphate, AFt), sat | $C_6A\bar{S}_3H_{32}$ | 1254 | 1.71 *1.75* | 735 *717* |
| Ettr. monosulphate (AFm), sat | $C_4A\bar{S}H_{12}$ | 622 | 1.99 | 313 |
| Hydrogarnet | $C_3AH_6$ | 378 *407* | 2.52 *2.67* | 150 *153* |
| Iron hydroxide | $FH_3$ | 214 | 3.1 | 69.8 |
| Calcium silicate hydrate (20°C) | $C_{1.7}SH_4$ | 227 | 2.12 | 108 |
| Pozzolanic C-S-H | $C_{1.1}SH_{2.1}$ | 159.4 | 1.97 | 81 |
| C-S-H$_{LD}$, *dried* | *$C_{3.4}S_2H_3$* | *365* | *1.44* | *252* |
| C-S-H$_{HD}$, *dried* | *$C_{3.4}S_2H_3$* | *365* | *1.75* | *211* |
| Calcium hydroxide (portlandite) | $CH$ | 74 | 2.24 | 33.1 |
| Syngenite | $KC\bar{S}_2H$ | 328 | | |
| Stratlingite | $C_2ASH_8$ | 418 | 1.94 | 215.6 |
| Silica | $S$ | 60 | 2.2 | 27 |
| Aluminosilicate | $AS$ | 162 | 3.25 | 49.9 |
| Calcium chloride | $CaCl_2$ | 111 | 2.15 | 51.6 |
| Freidel's salt | $C_3A(Ca$ $Cl_2)H_{10}$ | 561 | 2.97 | 189 |
| Calcium aluminosilicate | $C_2AS$ | 274 | 3.05 | 89.9 |
| Calcium aluminodisilicate | $CAS_2$ | 278 | 2.77 | 100.4 |
| Calcium carbonate | $C\bar{C}$ | 100 | | |
| Water | $H$ | 18 | 1.00 | 18 |

Table 2.1: Compound properties used in cement chemistry, data from [9],* with approximate values. *Slanted* values are according to Tennis and Jennings [113]

### 2.2 Definitions

The water-to-cement ratio, further denoted as *w/c*, is the mass ratio in the initial mixture of water to cement

$$w/c = \frac{m_w^0}{m_c^0} = \frac{\rho_w \cdot V_w^0}{\rho_c \cdot V_c^0}, \tag{2.1}$$

$$
\begin{aligned}
m_w^0 \quad &= \quad \text{initial water mass content,} \\
m_c^0 \quad &= \quad \text{initial cement mass content,} \\
\rho_w \quad &= \quad \text{water density,} \\
\rho_c \quad &= \quad \text{cement density,} \\
V_w^0 \quad &= \quad \text{initial water volume,} \\
V_c^0 \quad &= \quad \text{initial cement volume.}
\end{aligned}
$$

When the mixture contains certain replacement of cement such as fly ash, silica fume, or contains various admixtures, the term water-to-binder ratio is used

$$w/b = \frac{m_w^0}{m_b^0} = \frac{\rho_w \cdot V_w^0}{\rho_b \cdot V_b^0}, \tag{2.2}$$

$$
\begin{aligned}
m_b^0 \quad &= \quad \text{initial binder mass content} = m_c^0 + m_{SF}^0 + m_{FA}^0 + ..., \\
\rho_b \quad &= \quad \text{binder density,} \\
V_b^0 \quad &= \quad \text{initial binder volume.}
\end{aligned}
$$

The overall density of a material can be expressed as the inverse sum of mass ratios multiplied by inverse component densities

$$\rho_{tot} = \frac{1}{\sum \frac{m_i}{m_{tot}} \cdot \frac{1}{\rho_i}}, \tag{2.3}$$

$$
\begin{aligned}
m_i \quad &= \quad \text{mass of } i\text{-th component,} \\
m_{tot} \quad &= \quad \text{total mass,} \\
\rho_i \quad &= \quad \text{density of } i\text{-th component.}
\end{aligned}
$$

Eq. (2.3) may be reformulated by relating the mass fraction to the volume fraction of individual components

$$\frac{m_i}{m_{tot}} = \frac{\rho_i}{\rho_{tot}} \cdot \frac{V_i}{V_{tot}}. \tag{2.4}$$

The degree of hydration, denoted with $\alpha$, generally quantifies the progress of chemical reaction. The most straightforward definition in the cement chemistry is the amount of hydrated

cement to the total initial one or expressed as the fraction of chemically bound water. In this work, the gypsum is not accounted for

$$\alpha = \frac{m_{c,hydrated}}{m_{c,initial}} = \frac{m_{w,n}}{m_{w,n}^0},$$ (2.5)

$m_{w,n}$ = mass of non-evaporable (chemically) bound water,

$m_{w,n}^0$ = mass of non-evaporable (chemically) bound water in completely hydrated paste.

The Portland cement paste may be broken down to the components: unhydrated cement, hydration products, together with non-evaporable, gel and capillary water.

### 2.3 Portland cement prior to hydration

Portland cement contains tricalcium silicate ($C_3S$) in addition to the hydraulic lime. Tricalcium silicate originates in the kiln temperatures over $1250°C$ during sintering of a lime-rich mixture. Sintering results in a microstructure where clinker minerals are melted together and mineral domains at micrometer scale may be identified. Typical Portland cement composition with potential heat release of clinkers and comparison with other types of cements is in Tab. 2.2.

| Chemical mineral Cement type | Mass amount % Min-average-max | Potential heat [J/g] |
|---|---|---|
| $C_3S$ | 45 - 63 - 80 | 500 |
| $C_2S$ | 5 - 20 - 32 | 250 |
| $C_3A$ | 4 - 8 - 16 | 1340 |
| $C_4AF$ | 3 - 7 - 12 | 420 |
| Free $CaO$ | 0.1 - 1 - 3 | 1150 |
| Free $MgO$ | 0.5 - 1.5 - 4.5 | 840 |
| Generic Portland cement | - | 375–525 |
| Blast furnace slag cement | - | 355–440 |
| Sulphate-resistant cement | - | 350–440 |
| Pozzolanic cement | - | 315–420 |
| High alumina cement | - | 545–585 |

Table 2.2: Typical composition of silicate clinker or cement and the potential amount of heat [110]

The major constituent phase of Portland cement is *alite*, i.e. $C_3S$ with some small impurities built in its crystals. Seven forms of alite were proved: three monoclinic, three triclinic and one rhomboedric. The monoclinic form is present in commercially available cements [110].

Belite, i.e. $C_2S$ with impurities, is present in commercial cements exclusively in its $\beta - C_2S$ modification.

$C_3A$ crystallizes in a cubic shape. This aluminate constituent is known for high amount of potential heat and quick hydration.

$C_4AF$ known as *brownmillerit* is a solid solution with summation formula in the range of $C_6A_2F - C_6AF_2$.

The amount of gypsum, typically up to 5.0 % vol., is added during grinding in order to control the setting of cement, mainly the $C_3A$ phase. Without that, the $C_3A$ would develop a flash set, resulting in a loss of workability. On the other hand, there is a danger of gypsum expansion if higher amounts are used.

$Na_2O$ and $K_2O$ as alkalis, typically up to 1.5 % vol., influence the setting time of cement and early kinetics of reactions. Their effect on following hydration is not significant from the point of view of heat release or strength gain, but may be shifted as reactions are sped up.

Free lime in higher content, as the result of improper reaction during burning or artificially added, may result to delayed hydration or microstructure disintegration. The free lime may absorb water, creating portlandite in later stages.

Since cement is made from various calcite sources, considerable amount of impurities may be present. Equivalent oxides such as MgO, periclase or kaolin are typical examples of impurities. The simulation of hydration usually neglects an effect of these substances. However, in certain cases they may be detrimental to the microstructure, e.g. delayed expansion in cements made from dolomitic limestone [66].

### 2.4   Hydration of constituents of Portland cement

After contact with water, cement hydrates and hardens and the microstructure forms. The rate of hydration (kinetics) of particular minerals can be sorted in Portland cement as

$$(\text{rhomb.} > \text{triclin.} > \text{monoclinic}) \; C_3A > C_3S > C_4AF > C_2S. \tag{2.6}$$

#### 2.4.1   Hydration of $C_3S$

The most common mineral in Portland cement is $C_3S$, Tab. 2.2. The major part of it hydrates during 30 days and is responsible for early strength gain. The Portland cement is often reduced in models to only $C_3S$ mineral due to middle kinetics and high content in the cement [87, 93]. The hydration can not be exactly expressed in stoichiometric terms due to the variations in cement gel composition

$$C_3S + (3 - x + y)H \rightarrow C_xSH_y + (3 - x)CH. \tag{2.7}$$
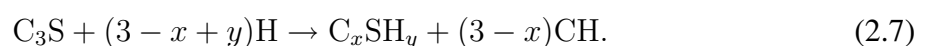
The C-S-H composition is only approximate and may vary in different cement, see section 2.5. If x$\in \langle 0.5, 1.5 \rangle$ and y$\in \langle 0.5, 2.5 \rangle$ C-S-H type I forms, if x$\in \langle 1.5, 2.0 \rangle$ and y$\in \langle 1.0, 4.0 \rangle$ C-S-H type II forms [25, 66]. It becomes convenient to simplify the coefficients to the average values of $x = 1.7$ and $y = 4.0$ [8].

The concept of the $C_3S$ hydration according to Jawed *et al.* [54] can be seen as the five stage process and is summarized in Tab. 2.3.

| Stage | Degree of reaction | Time | Characteristics |
|---|---|---|---|
| Initial | I. preinduction period | Minutes | Initial hydrolysis stage, ions are released |
| | II. induction (dormant) period | 1/3–2 h | C-S-H begin to form, continuous dissolution |
| Middle | III. acceleratory period | 2–11 h | Growth of hydration products |
| | IV. deceleration period | 11–26 h | Steady growth of hydration products, origin and evolution of microstructure |
| Late | V. diffusion period | >26 h | Evolution of microstructure |

Table 2.3: Stages in the hydration process of $C_3S$
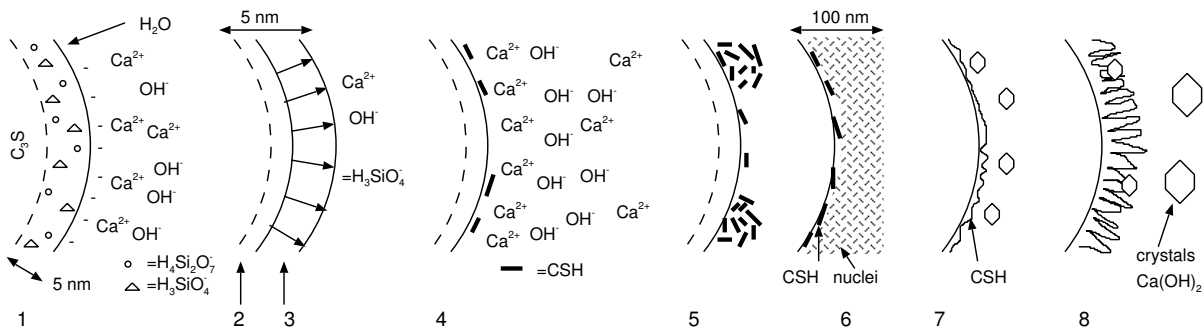


Figure 2.1: Hydration of $C_3S$ from the first contact with water to its late period

The theories aiming at explaining the behavior in the induction period fall in two categories: protective coating theories and delayed nucleation theories. The first one will be described further [110].

In the *initial* period, after a short contact with water, ions $Ca^{2+}$ and $OH^-$ are released forming electric double-layer at supersaturated solution, Fig. 2.1-1. As a counterpart, $H_3SiO_4^-$ and $H_4Si_2O_7^{2-}$ ions become active. $Ca^{2+}$ ions quickly penetrate easily through the immobile silicate

layer, e.g. the condition after 1 s of water contact is in Fig. 2.1-2. Water coats the surface with a thin film layer, Fig. 2.1-3, and after a few minutes the first C-S-H begin to form, Fig. 2.1-4. The degree of hydration is very low after the induction period, typically up to one percent.

The presence of the electric double-layer during the *dormant* period is an obstacle for migrating ions and the rate of reaction is slowed down. Ions also penetrate into distant areas in forming cement microstructure. The similar findings were observed by abrupt heat release succeeded by the dormant period.

After a few hours C-S-H begin to form clusters near to the surface of $C_3S$, figure Fig. 2.1-5. C-S-H with low density (LD) starts to evolve. The degree of hydration after induction period is very low but this changes now rapidly. Chemically controlled reactions are typical for the *acceleratory* period. Nuclei formed close to the grain surface are $Ca^{2+}$, $OH^-$ and silicate ions; CH or C-S-H evolve depending on the quantity of ions, figure Fig. 2.1-6. The rate of hydration is governed by the dissolution of $C_3S$ accompanied by heat release and $Ca(OH)_2$ crystallization in a pore space. The water entering into the grains is governed by diffusion through the cement gel and water transport is much more important than the rate of reactions. The nuclei have to overcome minimal size in order to grow, Fig. 2.1-7. The crystals of $Ca(OH)_2$ are formed and grow either separately, so called Ostwald ripening, or are engulfed into progressing C-S-H, Fig. 2.1-8.

As a result of excessive grow and the build-up of the reaction products, the *deceleration* period is more controlled by the diffusion. Fibrilar C-S-H phase is getting into capillary pore space, connecting mutually other particles, CH crystals grow together.

In the *diffusion* period the gel densifies without any substantial structural changes. The growth of C-S-H and CH is reduced since the reactions are rather diffusion-based.

Admixtures have a big influence on the rate of $C_3S$ hydration and emerge as a problem in the modeling of cement hydration. The majority of inorganic substances causes the acceleration, organic admixtures generally retard the hydration. The impact of admixtures is remarkable during the middle stages of hydration: the acceleratory and deceleration period. For example, calcium salts supply cations stimulating the dissolution of $CaO$ or CH thus accelerating the dissolution of silica or alumina. Alkaline cations such as sodium, potassium and ammonium play a similar role.

### 2.4.2 Hydration of $C_2S$

During the hydration of $\beta$-$C_2S$ (further $C_2S$), the same products are formed as in the case of $C_3S$; C-S-H and CH. The whole reaction proceeds much slower compared to $C_3S$; the majority reacts as late as one month, continuing even after one year. Because of the slow reaction, the

rate of released heat is low. The reaction can be approximately summarized with a coefficient of $x = 4$

$$C_2S + (0.3 + x)H \rightarrow C_{1.7}SH_x + 0.3CH. \tag{2.8}$$
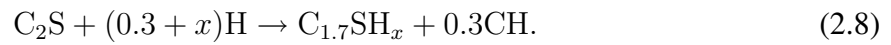
### 2.4.3 Reactions of $C_3A$

The amount of $C_3A$ contained in cement varies strongly depending on the input materials for clicker production. The hydration proceeds differently with gypsum/$C_3A$ ratio, Tab. 2.4 and Fig. 2.2.

| $C\overline{S}H_2/C_3A$ | Hydration products |
|---|---|
| $> 3$ | Trisulphate and gypsum, resupply |
| 3.0 | Trisulphate |
| 1.0–3.0 | Trisulphate and monosulphate |
| 1.0 | Monosulphate |
| $< 1$ | Monosulphate and $C_4AH_{13}$, $C_2AH_8$ or $C_3A(C\overline{S}, CH)H_{12}$ |
| 0 | $C_3AH_6$ |

Table 2.4: The effect of gypsum on $C_3A$ hydration products
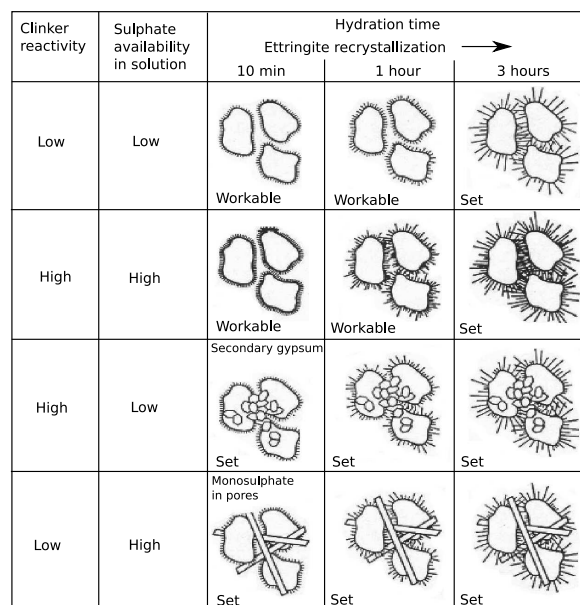


Figure 2.2: Locher's mineralogical model of early $C_3A$ hydration [69]

The reaction of pure $C_3A$ with water is accompanied by significant heat release. The first products are unstable hexagonal hydrates that later change to cubic hexahydrates $C_3AH_6$. If RH is less than approximately 88 %, $C_4AH_{19}$ loses six molecules of bound water. Especially higher temperature promotes its conversion to the hexagonal form, being very rapid above $30°C$. If the hexagonal nuclei have been already formed, the crystal growth is visible even below $30°C$ [25]. The life of hexagonal hydrates at room temperature is around 24 h. The conversion itself might increase a porosity resulting in decreased mechanical properties. On the other hand, experiments above $80°C$ have testified direct conversion to hexahydrate in the cement paste with no increase in porosity [25]. The pure hydration, with interproducts and in the shortened form, reads

$$2C_3A + 27H \rightarrow C_4AH_{19} + C_2AH_8 \quad \rightarrow \quad 2C_3AH_6 + 15H, \tag{2.9}$$

$$C_3A(270) + 6H(108) \quad \rightarrow \quad C_3AH_6(378).$$
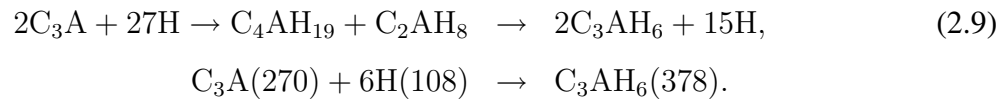
Moreover, in the presence of CH and in the absence of gypsum, hydration leads to the false setting

$$C_3A(270) + CH(74) + 12H(216) \rightarrow C_4AH_{13}(560). \tag{2.10}$$
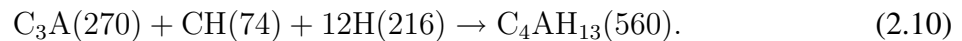
The hydration of $C_3A$ is normally attended by the presence of the sulphate in the mixing water. Sulphates are derived mainly from gypsum and with aluminates form a crystal ettringite $3CaO \cdot Al_2O_3 \cdot 3CaSO_4 \cdot 32H_2O$, visible as needle-like structures, occupying as much as 15–20 % vol. in mature concrete [25]. Ettringite attaches to the surface of $C_3A$, defending easy water access and starting the induction period. After about 1 day, the sulphate is consumed by ettringite and therefore disappears from the mixing water. $C_3A$ then decomposes the ettringite further

$$C_3A(270) + 3C\overline{S}H_2(516) + 26H(468) \quad \rightarrow \quad C_6A\overline{S}_3H_{32}(1254), \tag{2.11}$$

$$2C_3A(540) + C_6A\overline{S}_3H_{32}(1254) + 4H(72) \quad \rightarrow \quad 3C_4A\overline{S}H_{12}(1866). \tag{2.12}$$
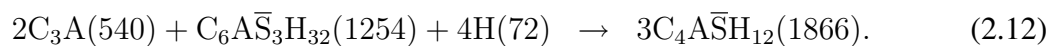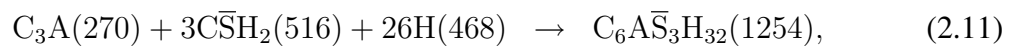
The product is monosulphate with greater permeability, considered to be stable in hardened cement paste and visible as platelets. If no more sulphate is available in a mixing water, the formation of C-A-H occur in many steps up to the chemically stable product $C_3AH_6$ according to Eq. (2.9).

### 2.4.4  Reactions of $C_4AF$

The hydration of $C_4AF$ is much slower than that of $C_3A$ and strongly depends on the content of iron. $C_4AF$ is a convenient simplification of many kinds of solid solutions. The hydration

takes approximately the form

$$C_4AF(486) + 10H(180) \rightarrow C_3AH_6(378) + CH(74) + FH_3(214). \qquad (2.13)$$
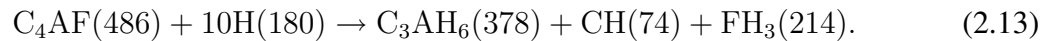
The ferrite reaction is probably slowed down by the presence of sulphate, at the beginning of the hydration [25]

$$C_4AF(486) + 3C\bar{S}H_2(516) + 30H(540) \rightarrow C_6A\bar{S}_3H_{32}(1254) + CH(74) + FH_3(214). \quad (2.14)$$

If insufficient sulphate is no longer present or if the temperature is higher than 70°C, the AFt converts to AFm phase [25]. The compressive strength of $C_4AF$ as a pure compound is very low, approximately 1 MPa after one year of hydration [25].

## 2.5 Characterization of hydration products

The hydration of Portland cement is different from the sum of reaction of its individual components. The mutual interaction of reactions gives different equilibrium conditions being compelled to the different amount of products. The whole reactions of cement proceed in a similar manner as the $C_3S$ hydration with the five distinguished periods, see section 2.4.1. Such similarity suggests that the cement hydration process can be studied by much simpler silicate systems itself.

It is no doubt that C-S-H is the major hydration product in Portland cement systems. The importance to various physical behavior was emphasized many times [66, 110, 112, 113]. Portlandite is important in degradation processes and in promoting alkalinity of the cement paste [101].

### 2.5.1 Calcium hydroxide

Calcium hydroxide, or portlandite, CH, is the product of silicates hydration where $C_3S$ releases approximately three times more CH than $C_2S$, see Eq. (2.7), (2.8). The total product volume of a well-hydrated cement is comprised by 20–25 % [65]. Under the microscope, the CH crystals are observed as hexagonal platelets, embedded within the C-S-H matrix [101, 110]. During the first burst of ions, calcium hydroxide buffers the solution to a pH $\sim 12.5$. The contribution to the strength due to van der Waals forces is small because of the low surface area.

The size of CH crystals may reach up to hundreds of micrometers. If possible, the crystals grow in the pore space. When no big pores are available, the portlandite is intimately mixed with C-S-H which evolves simultaneously.

The leaching of cement paste easily attacks and dissolves portlandite, consequently reducing mechanical properties. A homogenization results showed clear reduction of Young's modulus by 50 % in matured cement pastes due to the dissolution, section 7.1.9 [57].

### 2.5.2   *Calcium silicate hydrates*

Calcium silicate hydrates (C-S-H) are the main hydration product with an internal complex structure that can be visualized with many imperfections sometimes in almost amorphous phases. C-S-H evolves exclusively from silicate minerals or pozzolanic reactions in cement.

C-S-H consist of the elementary tetrahedron monomer $SiO_4^{4-}$ creating polymeric chains terminated by water molecules. $Ca^{2+}$ ions preserve electrical neutrality. The typical chain length for ordinary hardened cement is 2–3, increasing to 4 with decreasing *w/c* and with the addition of silica fume [100]. If only tetrahedron anion and calcium cation are considered, then the ratio C/S is $3:2 = 1.5$ for dimers and $4/3 = 1.33$ for trimers in order to balance electrical charge. In reality, $OH^-$ anion outbalances the positive charge too and the ratio is around 1.7 (from 1.2–2.3 for neat cement pastes). Al atoms can substitute Si preserving the same polymer structure. The Ca/(Si+Al) ratio in cement slag pastes is then in the range from 0.7 to 2.4 [113]. Free electrons on Si atoms can cross-link the polymer chains resulting in the spatial structure. The condensation can be written in a simple form

$$\cdot \dot{S}i - OH + HO - \dot{S}i\cdot \ \rightarrow \ \cdot\dot{S}i - O - \dot{S}i \cdot + H_2O. \tag{2.15}$$
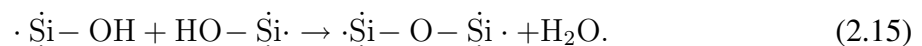
Aging can be measured by the degree of silicate polymerization; dimers dominate at early times and over decades convert to pentamers or so [112]. Under higher temperature polymeric species with more than 100 units can form [66]. C-S-H are sorted on their relations into different main groups [66]

**wollastonite** with prismatic crystals, nekoit, okenit, xonotlit, foshagit, hillebrandit; wollastonite acts as microfiber reinforcement in hardening cement,

**tobermorite** found from crystal to amorphous structure in the forms of foil, truss, and threads,

**C-S-H I.** are imperfectly crystallized structures with ratios C/S $= 1 - 1.5$ that appear as foil or platelets and originate from the reaction of $Ca(OH)_2$ with silica acid,

**C-S-H II.** are imperfectly crystallized structures with ratios C/S $= 1.5 - 2$ that appear as threads and originate from the hydration of $C_3S$ ,

**nearly amorphous tobermorite phases** referred to as hydrosilica gel, appearing in the electron microscope as isometric mutually connected particles, foils, threads; surface area around 250 m$^2$/g ,

**other** minor phases not too important for cement hydration can be found, e.g. [110].

Direct measurements of microstructure, surface area and pore size distribution yield no commonly acceptable values for C-S-H. The usage of different techniques complicates the

whole research, e.g. the specific surface area for highly hydrated paste ranging from about 25–700 m$^2$/g. This value is almost equal to the surface area of hardened cement paste since the contribution by other hydration products is negligible. All formed C-S-H are not significantly different in X-ray properties. Even naturally formed tobermorite with lime/silica ratio 0.8:1 is not different in X-ray structure. Physical properties of hydrates and their dependency on the relative air humidity were studied on the scale of 1–10 nm and several models were proposed. The J-T model predicts characteristic length of C-S-H microstructure in the range from about 1 to 100 nm and aims at interpreting the values measured from a gas porosimetry [55].

C-S-H is responsible for important properties of concrete: strength, volume stability, permeability, shrinkage, creep. The bonding to other products of cement hydration is generally good [95]. C-S-H are true fractals having similar properties spread over nanometric sizes (1–100 nm) thus modeling C-S-H as the building blocks is not accurate enough [55]. The polar water may greatly pack around the surface giving the high values for gel density.

It was observed in the past decades that the C-S-H, as the main hydration product, may be differentiated in two groups. The pairs were called inner - outer [95], middle - late product, phenograins - groundmass [26], low - high density (C-S-H$_{LD}$ - C-S-H$_{HD}$) [55, 113]. Though these pairs are not equivalent, they are closely related. A Jennings - Tennis (J-T) model was derived, based on the building block with a diameter of 2.4 nm, which is responsible for both types of C-S-H [55]. The J-T model predicts the characteristic length of C-S-H nanostructure in the range from about 1 to 100 nm and aims at interpreting values measured from the gas porosimetry.

Richardson [95] distinguishes two C-S-H morphologies: inner and outer. Inner C-S-H has typically a fine-scale and homogeneous morphology, containing pores under 10 nm in diameter. Outer products appear as a leftover of small particles with higher porosity, in all kinds of cements: Portland, slag or fly ash. When the slag dosage increases, the typical fibrillary morphology is replaced by a foil-like morphology that improves paste durability. The C/S ratio of C-S-H holds 1.2–2.3 with a mean of 1.75 in Portland cement pastes. The C/(S+A) ratio of C-S-H varies as 0.7 – 2.4 in water-activated slag cement pastes (replacement 0–100 %).

Taplin (ref. in [95]) assumes that inner C-S-H lies within original boundaries of a hydrating grain whether outer C-S-H expands into porous space. This assumption is simple and understandable, although not always correct [95].

Observation and analysis of backscattered electron images distinguish two types of the hydration products: phenograin and groundmass [26]. The criterion for their distinction is based on gross porosity and the phenograin size. The main drawback of this division is that phenograin or groundmass do not represent the chemical phases but rather a mixture of the hydrated mate-

rial [95].

It is believed that at the beginning of hydration only C-S-H$_{LD}$ appears due to unrestrained pore space while C-S-H$_{HD}$ originates in later stages of cement hydration when diffusion reactions dominate in the microstructure [113]. This transition happens at the nanometer scale and partially explains why different densities are often measured among similar C-S-H. According to the Kelvin equation, drying to about 85 % RH empties pores greater than 10 nm. Experiments found 40 % RH to be sufficient to cause shrinkage and collapse of LD microstructure. When the pores in the C-S-H are filled, the densities of both C-S-H$_{LD}$ and C-S-H$_{HD}$ were calculated as 1850 and 1980, or 2037 and 2195 kg/m$^3$, depending on the density of basic building unit [55].

Tennis and Jennings [113] assumed that C-S-H$_{HD}$ is not at all accessible by N$_2$ porosimetry while the C-S-H$_{LD}$ is. Based on these assumptions, the separation of both C-S-H types is done by multilinear regression [113]. The mass ratio of C-S-H$_{LD}$ to the total C-S-H was found to be

$$M_r = \frac{S_{N2}M_D}{S_{LD}M_t},$$ (2.16)

where $S_{N2}$ is the specific surface area of the dried paste, $M_D$ is the mass of dried paste, $S_{LD}$ is the surface area per gram of D-dried C-S-H$_{LD}$ and $M_t$ is the total mass of C-S-H. Eq. (2.16) yields strange results especially at the beginning of hydration, where nearly 50 % of C-S-H$_{HD}$ is already formed. This does not correspond to the idea that C-S-H$_{HD}$ emerges at later stages, where probably confinement plays the role for denser structure formation.

The models, which were proposed for the evolution of both C-S-H types, are presented in sections 3.4.6 and 3.4.7.

## 2.6 Degree of hydration concept related to mechanical properties

Degree of hydration is a macroscopic quantity describing mass ratio of reacted cement. Correlation with liberated heat [20], chemically bound water [66], chemical shrinkage [110], compressive strength [32] or electrical conductivity [6] was reported. During this work, only four cement clinker minerals are accounted for the degree of hydration, excluding gypsum and other phases.

In many cases the complete hydration does not occur due to a lack of water and necessary space for forming reaction products as deduced by Powers and his coworkers [92]. The degree of hydration indicates the development of microstructure macroscopically.

It was observed that stiffness in terms of elastic properties evolves more progressively than strength at early ages [102]. It must be noted that the experimental data of such measurements depend on used technique; however, from a micromechanical point of view the origin of strength and stiffness is the same, corresponding to the presence of a first spanning cluster. This is the

initial period where a very low degree of hydration is measured, see Tab. 4.1. On the other hand, Schutter and Taerwe [102] report the critical degree of hydration of 0.25 for $w/c = 0.5$. This points rather to experimental difficulties of young samples than to the real threshold of mechanical properties.

The porosity of material may be expressed via a combination of degree of hydration and Powers and Brownyard's model, section 3.3. In more details, the linear relationship between strength and degree of hydration was formulated by Fagerlund [32]. The concept originates from the idea that strength of a porous material $f$ is proportional to the load carrying area, regardless on material phase, Fig. 2.3. Following equations formulate the strength evolution in terms of porosity that is expressed as a function of the degree of hydration

$$f = f_0 \left( 1 - \frac{P}{P_{CR}} \right) = A f_0 \left( \frac{\alpha}{\alpha_{CR}} - 1 \right) = \left( \frac{A f_0}{\alpha_{CR}} - A f_0 \right) \frac{\alpha - \alpha_{CR}}{1 - \alpha_{CR}} =$$

$$= A f_0 \left( \frac{1 - \alpha_{CR}}{\alpha_{CR}} \right) \frac{\alpha - \alpha_{CR}}{1 - \alpha_{CR}} = f_{max} \frac{\alpha - \alpha_{CR}}{1 - \alpha_{CR}}, \tag{2.17}$$

$$A = \left( \frac{w_0/c + a_0/c}{m \cdot w_n^0/c \cdot \alpha_{CR}} - 1 \right)^{-1}, \tag{2.18}$$

where the meaning is as follows

| | |
|---|---|
| $f$ | the strength of a porous material, |
| $c$ | the cement content, kg/m$^3$, |
| $w_0/c$ | the water cement ratio, |
| $m$ | specific volume of non-evaporable water to evaporable, |
| $w_n$ | the non-evaporable water content, kg/m$^3$, |
| $w_n^0$ | the non-evaporable water content in completely hydrated paste, kg/m$^3$, |
| $a_0$ | the air content, l/m$^3$, |
| $f_0$ | the fictitious strength of pore free material that depends on type, gradation, and amount of aggregates; the intrinsic strength, |
| $f_{max}$ | the fictitious strength of one specific composition, |
| $\alpha_{CR}$ | critical degree of hydration corresponding to zero strength, |
| $P$ | porosity of material, |
| $P_{CR}$ | critical porosity corresponding to zero strength. |

For Portland cement paste $w_n^0/c \sim 0.25$ and $m \sim 0.75$. The coefficient $f_0$ is the fictitious strength of the completely pore-free material; it is a fictitious value and an extrapolation of a strength-porosity curve to zero porosity. A completely pore-free material would have a considerably higher strength [32]. $f_0$ is an inherent property of the solid phase and therefore appears independent of *w/c*.

Powers and Brownyard [92] found compressive strength on mortars within the range of 180 to 342 MPa, for pure compacted cement paste Bajza found 450–500 MPa. The amount of air

present in a mixture is more critical in small amounts, reducing $f_0$ much more than the same amount added to the material with "normal" porosity, e.g. Popovics [89] states that an increase of 5 % in the air content reduces the compressive strength to two-thirds of its original value.

The compressive strength relation between paste, mortar and concrete based on measurements is suggested to depend on the volume fraction of aggregates, $V_a$ [32]

$$f_{mortar,concrete} = f_{paste}(1 - 0.73V_a). \tag{2.19}$$

The critical degree of hydration $\alpha_{CR}$ corresponds to a constant ratio between the volume of the cement gel and capillary pore volume. $\alpha_{CR}$ corresponds to the value of zero strength and increases with increasing *w/c*. Also the results for mortars containing between 50–60 % of sand were similar, according to Powers and Brownyard [92]

$$\alpha_{CR} = 0.44w_0/c \ \sim \ 0.4w_0/c + 0.06. \tag{2.20}$$

Fagerlund [32] states that the critical degree of hydration in paste, mortar, or concrete is the same under the same conditions and may be attributed purely to the cement paste. His model implies the same "negative" extrapolated strength at the degree of hydration of zero for a given mixture with different *w/c*'s .
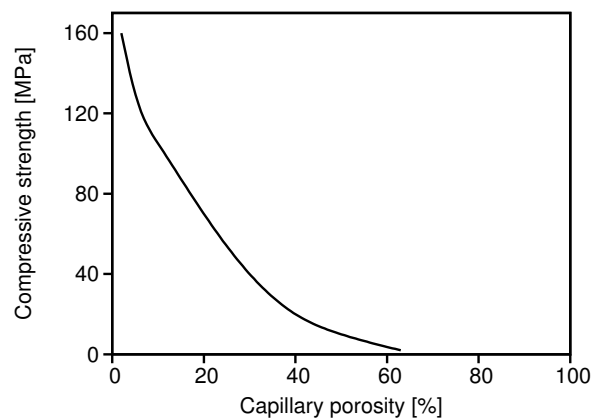


Figure 2.3: Strength vs. capillary porosity for normally cured cement pastes [124]

The relationship $f/\alpha$ reported by several authors does not have to be linear even though this is a widely used assumption. For example, Nielsen [82] reports a power law function.

# Chapter 3

# MODELING OF CEMENT HYDRATION

## *3.1 Affinity model*

An affinity model was found useful for the prediction of cement hydration during all hydration stages, e.g. [17]. The model assumes isotropic random microstructure that means independence on morphology, microstructure size, *w/c*, or fineness. To account for these effects, the input parameters of affinity model are to be modified. It is assumed that the rate of hydration degree is directly related to the affinity during the whole hydration

$$\frac{d\alpha}{dt} = \frac{\tilde{A}(\alpha)}{\tau},$$ (3.1)

where $\alpha$ is the degree of hydration, $\tilde{A}(\alpha)$ is the normalized affinity and $\tau$ is the characteristic time of a reaction. The latter depends on the type of clinker mineral, *w/c*, temperature and possibly on the fineness of clinker mineral [17].

The concept of reaction dependence on temperature is well described by the Arrhenius equation, in this particular case in terms of time scaling

$$\tau(T) = \tau(T_0) \exp\left[\frac{E_a}{R}\left(\frac{1}{T_0} - \frac{1}{T}\right)\right],$$ (3.2)

where $T$ and $T_0$ are arbitrary and some reference temperatures of a reaction, $R$ is the universal gas constant ($8.314 \, \text{Jmol}^{-1}\text{K}^{-1}$) and $E_a$ is the apparent activation energy.

The latter was found to be dependent on $\alpha$, clinker content and moreover on the temperature that somehow denies true meaning of the activation energy [21]. Wirquin *et al.* [127] give the values of activation energy for concrete prepared from CEM I 42.5, Tab. 3.1. They did not find the superplasticizer to change the reaction kinetics. Other authors, e.g. [21], have similar results around 40 kJ/mol for normal room temperature. It is a known fact in concrete engineering that the temperature increase by $10°\text{C}$ approximately doubles the reaction speed. Indeed, going from $20°\text{C}$ to $30°\text{C}$ means speed-up of hydration by 72 % for $E_a = 40$ kJ/mol, for example.

At least three processes are remarkable during cement hydration: dissolution, nucleation accompanied by the formation of hydration products, and diffusion.

Dissolution of particles in the initial period takes place in the first minutes after the contact

| Temperature | 10–20°C | 20–30°C | 30–40°C |
|---|---|---|---|
| Apparent activation energy [kJ/mol] | 32.04 | 38.3 | 45.7 |

Table 3.1: Apparent activation energy for concrete made from the cement CEM I 42.5 [127]

with water. The constant reaction rate is assumed, which implies

$$\tilde{A} = 1 \tag{3.3}$$

$$\tau = \frac{\alpha_0}{t_0}, \tag{3.4}$$

where $t_0$ is the duration of initial plus induction (dormant) period and $\alpha_0$ is the critical degree of hydration at that time. The end of induction period strongly depends on the chemical composition, fineness, *w/c*, flocculation, superplasticizer, and especially on alkalis and retarders. After dormant stage, the hydration degree is typically a few percent. Similar results were found when studying percolation in digitized microstructures, see Tab. 4.1.

The nucleation was studied extensively in metals and there was found a similarity with the acceleration period in hydrating cement [110]. The physical model is termed Kolmogorov-Johnson-Mehl-Avrami (KJMA) but it is a common practice to refer to this model as of Avrami model [2]

$$-\ln\left[1 - (\alpha - \alpha_0)\right] = \left[k(t - t_0)\right]^\kappa. \tag{3.5}$$

After differentiating with respect to time and replacement of $t - t_0$ by $\alpha - \alpha_0$ from Eq. (3.5), the following expressions reads

$$\frac{d\alpha}{dt} = \kappa k \left[1 - (\alpha - \alpha_0)\right] \left[-\ln(1 - (\alpha - \alpha_0))\right]^{1 - \frac{1}{\kappa}}. \tag{3.6}$$

The dimensionless form, according to Eq. (3.1), then reads

$$\tilde{A} = \frac{1 - (\alpha - \alpha_0)}{\left[-\ln(1 - (\alpha - \alpha_0))\right]^{\frac{1}{\kappa} - 1}}, \tag{3.7}$$

$$\tau = \frac{1}{\kappa k}. \tag{3.8}$$

The parameter $k$ defines reaction order while $\kappa$ represents the rate constant. For a variety of cement clinkers and various *w/c*'s, the parameters of Avrami model are summarized in Tab. 3.2 [16, 17, 110]. The table is valid for fineness of 360 m²/kg and an average cement grain radius of 5 $\mu$m.

Remarkable decrease in reaction kinetics is observed after acceleratory period. At that time, the hardly penetrable hydrates cover the cement grains and defend easy water access. Therefore, the hydration is driven by the amount of dissolved ions through the shell of hydrates.

| Clinker | *w/c* | $\tau(T_0)$ [h] | $\kappa$ | $\alpha_0$ | $D$ [mm²/h] | $\alpha_0^{dif}$ | $E_a$ [kJ/mol] |
|---------|-------|-----------------|----------|------------|-------------|------------------|----------------|
| C₃S | 0.3–0.7 | 10.5–13.5 | 1.66–1.86 | 0.02 | 0.42–15.6·10⁻⁸ | 0.6 | 37.41 |
| C₂S | 0.3–0.7 | 58.6–71.2 | 0.84–1.1 | 0.00 | 6.64·10⁻⁸ | 0.6 | 20.78 |
| C₃A | 0.3–0.7 | 39.5–57.7 | 0.86–1.14 | 0.04 | 2.64·10⁻⁸ | 0.6 | 45.73 |
| C₄AF | 0.3–0.7 | 14.3–27.0 | 2.16–2.44 | 0.04 | 0.42–15.6·10⁻⁸ | 0.6 | 34.92 |

Table 3.2: Parameters for affinity model of cement hydration for fineness of 360 m²/kg and average particle radius 5 $\mu$m [16, 17, 110]

Fuji and Kondo [35] described this phenomena by diffusion theory. Since the hydrates are deposited mostly around the cement grain, critical transition thickness may be determined based on the critical hydration degree, $\alpha_0^{dif}$. The normalized affinity during this hydration stage can be expressed as

$$\tilde{A} = \frac{(1 - \alpha)^{\frac{2}{3}}}{(1 - \alpha_0^{dif})^{\frac{1}{3}} - (1 - \alpha)^{\frac{1}{3}}}, \tag{3.9}$$

and the characteristic time in the form of diffusion coefficient $D$ and the initial radius of cement grain $R$ is formulated as

$$\tau(T_0) = \frac{R^2}{3D}. \tag{3.10}$$

The denominator of Eq. (3.9) may easily drop to zero when the degree of hydration is close to the critical one. This problem may be fixed by knowing that the hydration rate must decrease is the diffusion stage, thus it is possible to compare it with the acceleratory period.

The reaction kinetics due to the fineness of cement is taken into account by scaling the characteristic time $\tau$ linearly with the fineness ratio

$$\tau(T_0, \phi) = \frac{\phi_0}{\phi} \cdot \tau(T_0, \phi_0), \tag{3.11}$$

where $\phi_0$ represents the reference fineness and $\phi$ is the real cement fineness. Associated values for $\phi_0 = 360$ m²/kg and average particle radius of 5 $\mu$m are summarized in Tab. 3.2.

The amount of chemical phases during hydration may be easily accessed via the degree of hydration. The amount of hydrated cement is directly proportional to the progressing hydration degree, the rest of phases may be assigned according to Power's model [92], reformulated by, e.g. Hansen [41] or Bernard *et al.* [17].

The approach for the homogeneous phase system may be extended assuming either independent reactions or equal fraction rates. Then, the model is able to predict an evolution from all cement clinkers. Next extension is an introduction of two types of C-S-H, depending on the origin site: the high density product forms inside the grain initial boundary while the outer

products occupy original pore space [17]. Since the morphology of microstructure remains unknown, the model is perfect for the prediction of phase evolution. This approach was applied in analytical homogenization, for example [17].

The affinity model may be validated with experimental data, such as released heat during hydration. Fig. 7.33 is an example of validation with other hydration models. The parameters of affinity model were fit in the following manner: the length of dormant period as 3 hours, $\alpha_0^{dif} = 0.45$, $\tau = 13.5$, $\kappa = 1.72$, $R = 5\ \mu$m, $E_a = 40$ kJ/mol.

Tennis and Jennings [113] argue that Avrami equation is suitable for the degree of hydration up to 20–30 %, approximately up to 1 day of OPC hydration. The advantage of this approach is the possibility to assign different reaction rates associated with different phases of Portland cement paste.

### 3.2  Other models based on KJMA equations

A variety of other hydration models appeared, applying the KJMA equation, which is derived from the similarity between the volume fractions of overlapping particles and independently hydrating uniform particles. This equation was used in the work of Bezjak and Jelenic [19] for the modeling of cement hydration kinetics.

### 3.2.1  HYMOSTRUC model

The HYMOSTRUC model, developed in Delft by van Breugel [21] is a stereological vector model taking into account unhydrated cement, hydration products and porosity. The parameters for the governing KJMA reaction corrected for the diffusion of later hydration stages are given explicitly at the beginning of simulation, Fig. 3.1. This vectorized microstructure was used for studying autogeneous shrinkage [94] or percolation [132]. The model is based on the following assumptions

- reaction products are formed close to the grains,
- in a case of isothermal curing, the density of the reaction product (gel) is constant and independent of the place where it is formed,
- expansion and dissolution of cement particles are concentric,
- particles of the same size hydrate at the same rate,
- cement components hydrate at equal fractional rates.

Particles with diameter smaller than $\sim 3\ \mu$m are considered to dissolve immediately after a contact with water. Since the hydration products occupy more space than the solid cement

clinkers by a factor $\nu(t) \sim 2.2$, the outer radius of hydrated particle increases and the solid part of microstructure grows.

The corresponding penetration depth from the original boundary of the particle inwardly is $\delta_{in}$ and it is calculated directly from the degree of hydration $\alpha$ and the particle radius $r$

$$\delta_{in} = \frac{r}{2}(1 - \sqrt[3]{1 - \alpha}). \tag{3.12}$$

The volume of a newly formed product (gel) is bigger by a factor $\nu$ from the volume $v_{un}$ of the unhydrated particle

$$v_{ou} = (\nu - 1)\alpha v_{un}. \tag{3.13}$$

If no other cement is found around the expanding particle, the outer radius of such particle is

$$r_{ou} = \sqrt[3]{\frac{3v_{ou}}{4\pi} + \frac{r}{2}}, \tag{3.14}$$

and the thickness of the outer shell follows

$$\delta_{ou} = r_{ou} - \frac{r}{2}. \tag{3.15}$$

An increase of $\delta_{in}$ in time is calculated with a *basic rate formula* [21]. This formula is the multiplication of coefficients representing: the basic rate factor, the water withdrawal, the distribution of water, the amount of water, the effect of temperature based on Arrhenius equation, the product densification and the transition thickness when the reaction changes from the boundary to the diffusion type. Based on the assumptions, this formula is the same for particles with the same radii. $\delta_{in}$ reflects the effect of various chemical compositions and can express an effect of added alkali.
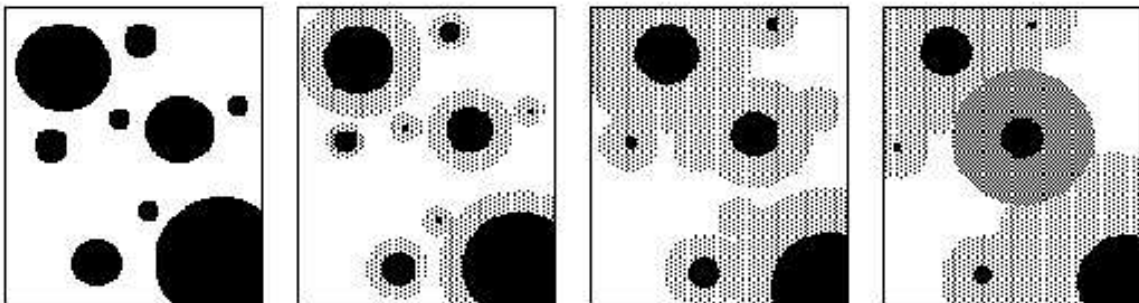


Figure 3.1: Evolution of the microstructure in HYMOSTRUC model, after [21]

### 3.2.2 Pignat and Navi's model

Pignat and Navi used the same approach as in HYMOSTRUC, corrected for later diffusion stages and different in portlandite placement [88]. The hydration of $C_3S$ particle is again concentric and creates the C-S-H shell deposited around the particle. Portlandite is placed as a sphere (with some corrections of neighbouring particles) in the pore space on nucleation sites. Therefore, the model recognizes $C_3S$, water, CH and C-S-H. Pignat and Navi [88] implemented the reaction of pure $C_3S$ according to the following stoichiometry

$$C_3S + 5.3H \quad \rightarrow \quad C_{1.7}SH_4 + 1.3CH, \tag{3.16}$$

where they assumed the density of 2 g/cm³ for C-S-H, 3.15 for $C_3S$ and 2.24 for CH. These densities are based mostly on experiments conducted by Jennings [55]. The molar volumes are then 72.381 cm³/mol for $C_3S$, 113.5 cm³/mol for C-S-H, and 33.036 cm³/mol for CH. They used the microstructure for the simulation of MIP technique, passing a liquid through the porosity necks [88]. The microstructures from this model will be compared to microstructures from the NIST model in sections 7.1.7 and 7.1.8.

### 3.3 Powers and Brownyard's model

Powers and Brownyard were the first who investigated quantitatively the reactions of cement with water and the formation of cement paste [92]. They presented a model where the unreacted cement, hydration product, gel and capillary porosity were distinguished. The innovation was an ability to quantitatively predict evolving phases. The non-evaporable water, another name for chemically bound or combined water, was found to be dependent mainly on the clinker composition and on the amount of reacted cement

$$m_{w,n}/m_c = 0.187 \cdot m_{C_3S} + 0.158 \cdot m_{C_2S} + 0.665 \cdot m_{C_3A} + 0.213 \cdot m_{C_4AF}, \tag{3.17}$$

where the letter $m$ denotes the mass of a phase, e.g. $m_{w,n}$ is the weight of non-evaporable water, $m_c$ means the weight of reacted cement and $m_{C_3S}$ represents the amount of consumed $C_3S$.

The amount of gel water was found to be dependent on the relative humidity (RH). Bellow 45 %, the gel water content was found to be proportional to the amount of reacted cement, or in other words to the amount of gel. Above RH 45 %, the water also condensed in the larger capillary pores. The amount of monolayered gel water $m_{w,m}$ was determined using the BET theory for adsorption isotherm. The first layer that was able to cover hydrated cement appeared at RH 20 %. The maximum amount of gel water was found, corresponding to $4m_{w,m}$. All water above this quantity is then the capillary water.

Powers and Brownyard [92] observed that $m_{w,m}$ exhibits a linear relationship with the amount of non-evaporable water, therefore the ratio remains constant. They found an empirical fit, where $\chi$ is the weight fraction of a component in the unhydrated cement

$$m_{w,m}/m_{w,n} = 0.230 \cdot \chi_{\mathrm{C_3S}} + 0.32 \cdot \chi_{\mathrm{C_2S}} + 0.317 \cdot \chi_{\mathrm{C_3A}} + 0.368 \cdot \chi_{\mathrm{C_4AF}}. \tag{3.18}$$

The constant ratio $m_{w,m}/m_{w,n} \sim 0.25$ implies that all clinker minerals react at the same fractional rates of hydration. In addition, the hydration products are independent of the origin of their birth.

The total volume of cement and mixing water at the beginning equal to the sum of volumes during hydration

$$V_{tot} = \frac{m_c^0}{\rho_c} + \frac{m_w^0}{\rho_w} = \frac{m_c}{\rho_c} + \frac{m_{w,n}}{\rho_{w,n}} + \frac{m_{w,g}}{\rho_{w,g}} + \frac{m_{w,cap}}{\rho_{cap}}, \tag{3.19}$$

| | | |
|---|---|---|
| $m_c^0$ | = | initial mass of cement, |
| $m_c$ | = | mass of cement during hydration, |
| $m_w^0$ | = | initial mass of mixing water, |
| $m_{w,g}$ | = | mass of gel water, |
| $m_{w,n}$ | = | mass of non-evaporable water, |
| $m_{w,cap}$ | = | mass of capillary water, |
| $\rho_w$ | = | mixing water density $\sim 1.0$ g/cm³, |
| $\rho_{w,n}$ | = | density of non-evaporable water $\sim 0.9$ g/cm³, |
| $\rho_{w,g}$ | = | density of gel water $\sim 1.0$ g/cm³, |
| $\rho_c$ | = | cement density. |

The total volume of cement gel, $V_B$, consists of the volume of the original cement that has hydrated, plus the volume of non-evaporable and gel water

$$V_B = \frac{\alpha m_c^0}{\rho_c} + \frac{m_{w,n}}{\rho_{w,n}} + \frac{m_{w,g}}{\rho_{w,g}}, \tag{3.20}$$

where $V_B$ is in units of cm³ per gram of cement. Although there is no information about the microstructure, the phase fractions are given for a specific hydration stage, expressed in terms of the hydration degree.

### 3.4 CEMHYD3D model

Analysis of the cement microstructure requires an universal robust model that would capture microstructural evolution within considered types of cements. A model should reflect at

least four effects: cement composition, particle size distribution (PSD), curing regime and temperature. For the purpose of mesh generation, discrete rather than vector type of the model is preferred. Cement hydration model CEMHYD3D, developed at NIST, is based on observing the development of 2D microstructure images under an electron microscope [8]. The idea is to split up a microstructure into voxels (volume elements), typically with an edge of 1 $\mu$m. A voxel should be considered as an accumulation of specific phase from the neighborhood, maintaining stoichiometry of chemical reactions and neglecting tiny details of the microstructure. The size of voxel determines the model resolution that should be small enough to capture the important undergoing processes, e.g. dissolution, transport and diffusion. This coincides with the resolution of experimental devices where an accurate identification of chemical phases is expected to be as fine as possible.

The 3D microstructure, forming a RVE, consists of chemical phases that are implemented as an ID assignment to each voxel. The rules how to handle individual voxels are called cellular automata and they define how voxels dissolve, move and what happens on their collision. Cellular automata are combined with probabilistic functions that were found effective in the description within considered model [37]. Hydration products are, with certain probabilities, formed on the grains exposed to water contact and they nucleate in the available pore space.

Initial and random 3D microstructure is reconstructed with the help of autocorrelation functions and typically contains four cement clinker mineral phases and forms of calcium sulfate, all as the digital spherical particles. The size of microstructure may be arbitrary, limiting the maximal cement grain that may be placed in. The microstructure remains periodic during all calculations which allows imposing the periodic boundary conditions in a homogenization process. A flowchart of the model with associated homogenization is showed in Fig. 3.2. Model cycles can be mapped on time axis using parabolic relationship [8]. Since this brings fitting parameter to the whole procedure, the calculations are related rather to the degree of hydration [71]. An example of cement microstructures is in Fig. 3.3.

Several problems occur when discretizing vector microstructures such that one of a cement paste. Since the resolution is limited, very fine cement particles cannot be captured at all. On the other way, they cannot be disregarded. Certain remedy is to map their dissolution to the fine cement grains that are represented by one voxel by means of changing the dissolution bias [10].

The model resolution cannot be arbitrary scaled for the reason of dissolution length. The neighborhood of eligible voxels, which are possibly ready for dissolution, is defined from the resolution. Higher voxel resolution causes that the large grains are not able to hydrate completely due to a layer of hydration products. When scaling, the maximum penetration depth would be scaled as well which is not true.
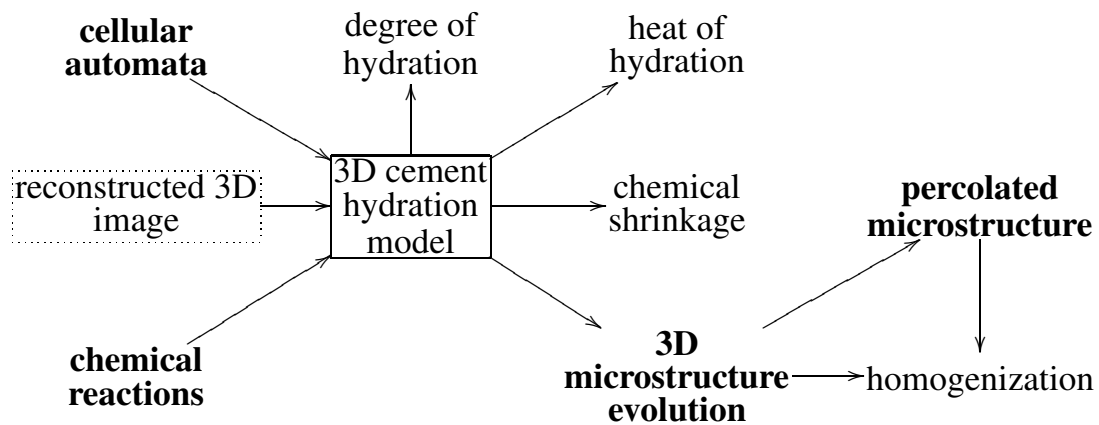
Figure 3.2: A flowchart of CEMHYD3D model and the homogenization process, adapted from [8]

Dissolution probabilities play further fundamental role in the cement kinetics. The rate is changed by temperature, alkalis (alkality of the water-filled porosity) and saturation. The dormant period as well as later stages may be modeled using this dissolution approach. Assumed "universal" dissolution values may be found in the program documentation [8, 10].

The kinetics of cement hydration in early stages is modeled by adjusting initial dissolution probabilities of four clinker minerals. Quadratic dependence on the normalized amount of formed C-S-H is adopted, i.e. the volume of formed C-S-H divided by the volume of initial cement amount. In the case of fine fillers, the dissolution probability is corrected by the fraction of surface area of initial cement and filler to the initial cement raised again to the second power [10].

Any model of a random system brings two sources of error: statistical fluctuation and finite size effect [37]. Statistical error emerges in any random system due to its representation, e.g. small dimensions of a cement paste. Finite size of RVE captures only a limited piece of material which means that the sample is not statistically homogeneous. This problem may be eliminated, when RVE is compared to the one that is considered sufficiently big. It was showed that for *w/c* 0.2 and 0.5, for fine and coarse cement, and for expected error in the degree of hydration of max. 10 % at the same cycle after approximately three hours of hydration, the reasonable microstructure size lies in the range of 20 – 50 $\mu$m [108]. This corresponds roughly to a suggested size of 100 $\mu$m by the authors of the model. Microstructure edge size above 100 $\mu$m was found to bring no significant accuracy in the hydration model prediction [37].

This model of cement hydration brings also digital resolution problems. The smallest information unit is the voxel of size of 1 $\mu$m, therefore any smaller size is considered only if the concentration around the neighborhood reaches that volume. This means that volumetric
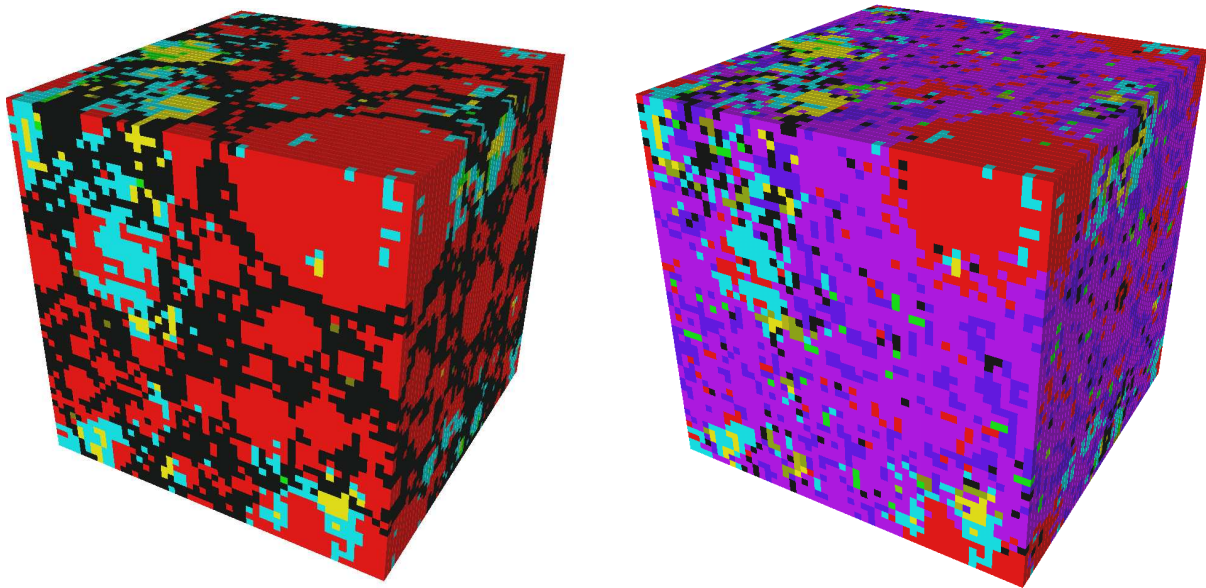
Figure 3.3: Microstructure $50 \times 50 \times 50$ $\mu$m, $w/c = 0.25$, initial (left) and at the degree of hydration of 0.63 (right). Red = $C_3S$, cyan = $C_2S$, green = $C_3A$, yellow = $C_4AF$, black = porosity, violet = C-S-H, blue = CH

fractions of chemical phases are maintained within the model but spatial distribution remains uncaptured below the resolution and small variations are expected in the neighborhood. In such a case, a suitability of the model depends on the properties of interest. Simulation revealed that digital resolution plays a significant role in percolation characteristics and in transport issues such as diffusivity or permeability [37]. The proper size for the voxel lies probably in the range of 0.125 to 1 $\mu$m/voxel that was determined using an assumption of continuous C-S-H phase and a dissolution rate of larger cement grains [37]. The progress of the reaction front towards a grain is also influenced by a dissolution length, specified as an amount of 6 or 26 of adjacent voxels. The latter value corresponds to a $3 \times 3 \times 3$ voxel box around the central voxel and specifies candidates to be dissolved. Although the dissolution length changes significantly hydration kinetics, the elastic results remain less touched. The effect of resolution and dissolution length on elastic properties will be explored in the section 7.1.5.

The discrete microstructure output contains at every voxel either the solid or the liquid phase. Special care has to be devoted to diffusing species that are placed in the water-filled porosity. They should be treated as the solid phase for image output because of maintaining the stoichiometry of chemical reactions. Therefore, the input homogenization routine changes CH and C-S-H dissolved species to the solid counterparts. Typically, the error in volumetric content disregarding this change is up to a few per cent and does not influence significantly the

results. At the end of hydration, the dissolution of solids is strongly reduced thus the caution is not necessary.

The extension of cement paste hydration to concrete is considered straightforwardly as an independent problem. Although the region around the aggregates contains the flow channels of water, the hydration is rather uninfluenced [79]. Therefore it is assumed that the aggregates in concrete do not influence hydration at all. The early stages of hydration do not strongly depend on the *w/c* and there is always enough available space to accomodate the hydration products. On the other hand, late hydration stages suffer from a lack of water and space. As the result, some ITZ zone develops. The only effect of adding aggregates for the model lies so far in the prediction of concrete temperature during the non-isothermal curing conditions and in different formation around aggregates in the microstructure.

In June 2005 the CEMHYD3D version 3.0 was released [10]. The major enhancement is the incorporation of alkali influence on early hydration properties. Following modeling issues were implemented as well: the influence of fine fillers such as limestone on hydration, precipitation of C-S-H in the plate or random morphology, probability of CH formation on an aggregate surface. The refined X-ray diffraction analysis of cement paste changed the initial dissolution probabilities in the following manner: $C_3S$ down by 14 %, $C_2S$ down by 50 %, $C_3A$ remained the same, $C_4AF$ down by 49 %. Also, some small changes were done on the densities of clinker minerals. The density dependence of the C-S-H remained the same. The kinetics of later hydration stages is changed as the power function of saturation, i.e. the relative amount of water-filled capillary porosity divided with all porosity. This mechanism reduces the dissolution probability from the total capillary porosity fraction of 0.22 thus accounting for later hydration stages.

Some of the researchers noted that the addition of finely grounded lime stone or other filler enhanced precipitation of hydration products [74]. These observations were incorporated in the model in such a way that C-S-H and CH could be formed also on the surface of the filler. Based on the simulation, the lime reaction within 180 days was only by 5 %, when 20 % of cement replacement was used [14].

Three hydration models were used to show the difference in performance: CEMHYD3D version 2.0, 3.0, and the results from Pignat and Navi's model. The $C_3S$ microstructure according to Pignat and Navi [87] with $w/c = 0.42$ was reconstructed. The CEMHYD3D parameters have to be slightly modified in order to obtain the same volumetric amount of hydration products as in Eq. (3.16). The hydration runs under sealed curing conditions and with disabled alkali effect on hydration. Fig. 3.4 shows the difference in the degree of hydration in dependence of the selected hydration model.
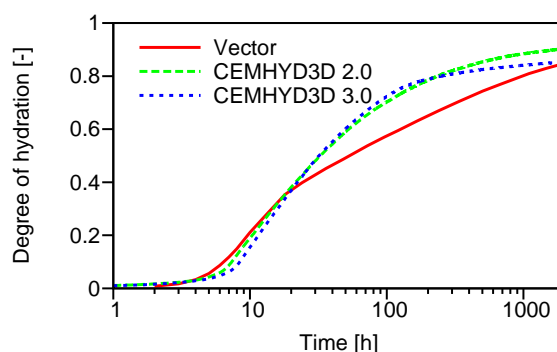
Figure 3.4: Results of three models on pure $C_3S$ hydration, $w/c = 0.42$

### 3.4.1 Implemented reactions

Cellular automata form the rules used during the simulation of hydration. Reaction means dissolution and collision with other voxels where the amount is prescribed by stoichiometric chemical reactions. The implemented reactions reflect the current knowledge of cement systems, see e.g. [110]. The silicate reactions were extended with pozzolanic reactions including materials such as silica fume. The stoichiometry of C-S-H phase is temperature dependent [8, 38], Eq. (3.30). Numbers in parenthesis quantify the volumetric amount of the phase

$$C_3S(1) + 5.3H(1.34) \rightarrow C_{1.7}SH_4(1.52) + 1.3CH(0.61) \quad 20°C, \quad (3.21)$$

$$C_2S(1) + 4.3H(1.49) \rightarrow C_{1.7}SH_4(2.07) + 0.3CH(0.191) \quad 20°C, \quad (3.22)$$

$$1.1CH(1.34) + S(1) + 2.1H(0.63) \rightarrow C_{1.1}SH_{2.1}(3.0). \quad (3.23)$$
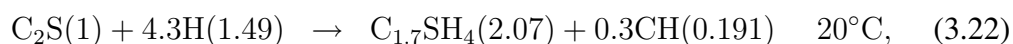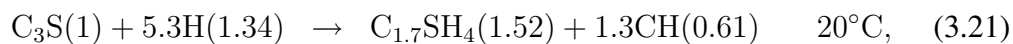
The aluminate reactions are based on the hydration of $C_3A$. The reactions of $C_3A$ are the fastest and strongly depend on the amount of gypsum. Eq. (3.24) represents the hydration without gypsum causing a flash set and the following reactions are with gypsum content forming ettringite later converted to the monosulphate phase. Slow ferrite reactions do not significantly

contribute to long-term properties of cement.

$$C_3A(1) + 6H(1.21) \rightarrow C_3AH_6(1.69), \qquad (3.24)$$

$$C_3A(0.4) + 3C\overline{S}H_2(1) + 26H(2.1) \rightarrow C_6A\overline{S}_3H_{32}(3.3), \qquad (3.25)$$

$$2C_3A(0.2424) + C_6A\overline{S}_3H_{32}(1) + 4H(0.098) \rightarrow 3C_4A\overline{S}H_{12}(1.278), \qquad (3.26)$$

$$C_4AF + 3C\overline{S}H_2 + 30H \rightarrow C_6A\overline{S}_3H_{32} + CH + FH_3, \qquad (3.27)$$
$$0.575 \qquad 1 \qquad 2.426 \qquad 3.3 \qquad 0.15 \quad 0.31$$

$$2C_4AF + C_6A\overline{S}_3H_{32} + 12H \rightarrow 3C_4A\overline{S}H_{12} + 2CH + 2FH_3, \qquad (3.28)$$
$$0.348 \qquad 1 \qquad 0.294 \qquad 1.278 \qquad 0.09 \quad 0.19$$

$$C_4AF + 10H \rightarrow C_3AH_6 + CH + FH_3. \qquad (3.29)$$
$$1 \qquad 1.41 \qquad 1.17 \qquad 0.26 \quad 0.545$$
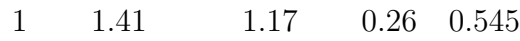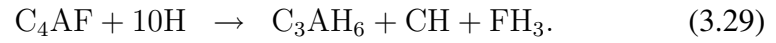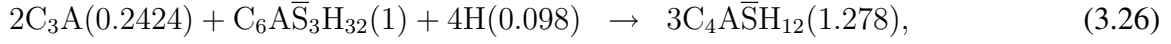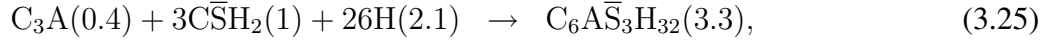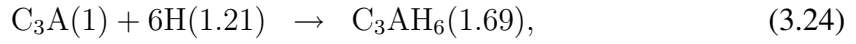
The temperature dependent C-S-H density is based on data of chemical shrinkage from Geiker [38]. The molar volume, S/H ratio and density are expressed as follows

$$\text{molar volume } [C_{1.7}SH_y] = 108 - 8\frac{T - 20}{80 - 20} \text{ cm}^3/\text{mol}, \qquad (3.30)$$

$$S : H = y = 1/\left(4 - 1.3\frac{T - 20}{80 - 20}\right), \qquad (3.31)$$

$$\text{density } \textbf{C-S-H}\,(T) = \frac{227.2}{110.67 - 0.133\,T} \text{ g/cm}^3. \qquad (3.32)$$

C-S-H density for $0°C$ is predicted as 2.05 g/cm³, at $20°C$ as 2.1 g/cm³ and at outmost high-temperature valid point of $80°C$ as 2.27 g/cm³. Tennis and Jennings [55] calculated densities at saturated conditions for C-S-H$_{LD}$ 1.85–2.037 g/cm³ and for C-S-H$_{HD}$ 1.98–2.195 g/cm³. Water appearing in nearly all reactions originates in the water-filled pore space or is provided externally, e.g. in a case of saturated conditions. An empty porosity may develop in the case when the pore network is depercolated, even in the case of saturated curing conditions.

### *3.4.2 Reconstruction of initial microstructure*

The microstructure reconstruction in CEMHYD3D consists of two steps: generation of discrete particles based on PSD and separation of chemical phases within the particles into clinker minerals.

The PSD is a continuous function that generally differs from cement to cement. For the simulation purpose, this function may be approximated by the Rosin-Rammler distribution (RR)

$$G(x) \;=\; 1 - e^{-bx^n}, \qquad \lim_{x\to\infty} G(x) = 1, \tag{3.33}$$

$$G'(x) \;=\; \frac{nbe^{(n\ln(x)-bx^n)}}{x}, \qquad \lim_{x\to\infty} G'(x) = 0,$$

where x [$\mu$m] is the particle diameter and $b, n$ are constants determined via the function fitting. Further in the reconstruction, the surface area is considered to be the smallest compared to the volume, i.e. the case of spherical particles. The number of spherical particles $n$ of specified diameter $x$ (between $x^-$ and $x^+$) is then calculated as

$$n = \frac{V_{ref} \int_{x^-}^{x^+} G'(x,b,n)\mathrm{d}x}{\text{volume of one particle}}, \tag{3.34}$$

where $V_{ref}$ is the reference volume of the particles unity, determined from *w/c*.

A reference database of cements is available at NIST [83] for different cement types or finenesses. Fig. 3.5 displays the PSD for German cements of type I from that database. The PSD curves are in an ascending order, depending on the fineness of cement. The parameters $b, n$ from Eq. (3.33) may be expressed as a function of cement fineness [m$^2$/kg] via the linear regression, Fig. 3.6

$$n \;=\; -0.00083333 \,\text{fineness} + 1.1175, \tag{3.35}$$

$$b \;=\; 0.000754 \,\text{fineness} - 0.143. \tag{3.36}$$
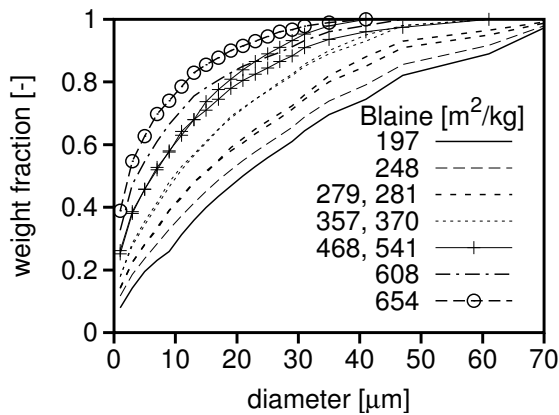


Figure 3.5: PSD for German cements, all cements are type I
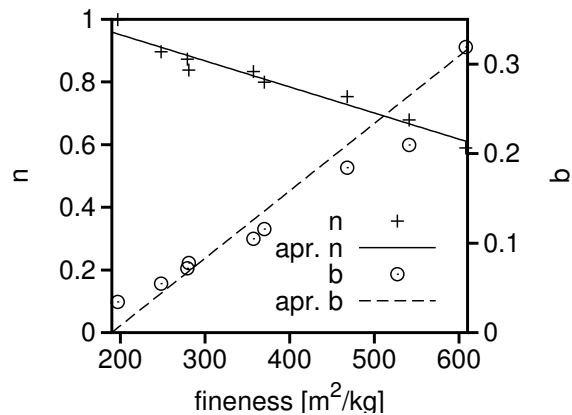
Figure 3.6: PSD for German cements from the NIST database

The PSD is usually truncated in order to accommodate all necessary particles. The maximal diameter of a sphere that can be placed into the CEMHYD3D microstructure is typically a half of its side length.

A two-point autocorrelation function $S(x, y)$ on an image $M$ x $N$ is introduced for the purpose of segmentation the cement grains to the groups of clinker minerals [9]

$$S(x, y) = \sum_{i=1}^{M-x} \sum_{j=1}^{N-y} \frac{I(i, j) \cdot I(i + x, j + y)}{(M - x) \cdot (N - y)}, \tag{3.37}$$

where I(x,y) and I(i+x, j+y) are boolean functions with the value of 1, if the voxel at that location is of interest, otherwise 0. Another efficient method for the calculation of $S(x, y)$ is based on fast Fourier transformation [134]. In order to extend the autocorrelation function into 3D, conversion from the Cartesian to polar coordinates is used

$$S(r) = \frac{1}{2r + 1} \sum_{l=0}^{2r} S(r, \frac{\pi l}{4r}), \tag{3.38}$$

$$S(r, \varphi) = S(r \cos \varphi, r \sin \varphi). \tag{3.39}$$

Bilinear interpolation is typically used to find the integer radius $r$. Autocorrelation function yields a phase area fraction at $S(0)$ and the second power of phase area fraction at $S(r \to \infty)$. Imposing a Gaussian noise image to a monophase microstructure image yields, after smoothing, the input microstructure for the subsequent hydration in the CEMHYD3D model [9].

### 3.4.3 Mapping hydration cycles to time

The rules of dissolution, collision and nucleation, handled with the help of the cellular automata, represent unfortunately no meaningful scale of time. Original linear mapping of cycles to time shows considerable disagreement with experiments [8]. Parabolic mapping, based on the Knudsen's parabolic dispersion model, was found appropriate under different curing conditions and cement types [9]. Knudsen's model assumes that the diffusion of ions takes the control over the hydration rate with the dormant period lasting $t_0$

$$\text{time} = t_0 + \beta \, \text{cycle}^2. \tag{3.40}$$

$$\Delta\text{time} = 2\beta\text{cycle}. \tag{3.41}$$

The parameter $\beta$ is usually found in the interval $1 \cdot 10^{-4} \le \beta \le 1.1 \cdot 10^{-3}$ [9, 11]. The time step during the hydration cycles is obtained by differentiating Eq. (3.40). The introduction of time step has the purpose in the heat transfer problems.

Since the time mapping is not based on any governing equation of physical processes, the choice may be somehow arbitrary. In some cases, the exponential relationship with one unknown parameter was found more adequate

$$\text{time} = \exp(\beta \, \text{cycles}^2). \tag{3.42}$$

### 3.4.4   Effect of initial microstructure size

In this section, the statistical descriptors of the unhydrated microstructure are studied. Generally, the size of RVE should be at least comparable with studied phenomenon, e.g. the ITZ of approximately 20 $\mu$m in thickness [81]. Bentz *et al.* [37] found the satisfactory size of RVE $100 \times 100 \times 100$ $\mu$m for the scatter of percolation and the degree of hydration.

Increasing the fineness of cement means a shift to smaller particles. However, when the mean grain size approaches small diameters, PSD tends to be narrower. Thus the appropriate RVE size is related to PSD and there are several descriptors available of the distribution

- *median diameter* $d_{50}$, when 50 % of the mass fraction is reached,
- *modal diameter* $d_{mod}$, when the density distribution function reaches its maximum,
- *balanced mean diameter* $d_{bal}$, is the abscissa of the center of density distribution area,
- *average particle diameter* $d_{a,V}$, $d_{a,S}$ represents the mono-sized spherical microstructure with an identical volume or surface area,

$$
\begin{aligned}
d_{a,V} &= \sqrt[3]{\int_0^\infty G'(x)x^3\mathrm{d}x}, \\
d_{a,S} &= \sqrt{\int_0^\infty G'(x)x^2\mathrm{d}x},
\end{aligned}
\tag{3.43}
$$

- *average diameter* $d_{disc}$ of discrete particles,

$$
d_{disc} = \frac{6V}{S}.
\tag{3.44}
$$

Tab. 3.3 summarizes the results for three different finenesses of a $C_3S$ cement powder according to RR distribution, truncated to the diameter of 47 $\mu$m. The volume above truncation is 3.3 and 23 % for 500 and 250 m²/kg. Average particle diameters $d_{a,V}$ and $d_{a,S}$ are close to each other but overestimate an average discrete diameter $d_{disc}$ due to the truncation.

The effect of RVE size was explored on two extremities widely used in practice: the most dilute ($w/c = 0.5$, Blaine fineness 250 m²/g) and the densest microstructure ($w/c = 0.2$, Blaine fineness 500 m²/g), Tab. 3.3. Particles were randomly placed without flocculation into RVE $300 \times 300 \times 300$ $\mu$m that was considered as an error-free reference.

At $w/c = 0.2$ and the fine cement of 500 m²/kg, the RVE $300 \times 300 \times 300$ $\mu$m contains $52.777 \cdot 10^{-6}$ g of cement. The calculated area of digital spheres is 473.1 m²/kg and that of ideal spheres approximately 2/3 smaller. Both values roughly correspond to input Blaine fineness.

| Fineness [m²/kg] | $b$ | $n$ | $d_{50}$ [$\mu$m ] | $d_{mod}$ [$\mu$m ] | $d_{bal}$ [$\mu$m ] | $d_{a,V}$ [$\mu$m ] | $d_{a,S}$ [$\mu$m ] | $d_{disc}$ [$\mu$m ] |
|---|---|---|---|---|---|---|---|---|
| 250 | 0.0455 | 0.9093 | 20.0 | 0.062 | 31.3 | 61.8 | 56.5 | 5.14 |
| 350 | 0.1209 | 0.8260 | 8.3 | 0.222 | 14.3 | 31.1 | 22.5 | 3.42 |
| 500 | 0.2340 | 0.7010 | 4.71 | 0.644 | 10.1 | 26.4 | 18.8 | 2.51 |

Table 3.3: Particle diameter statistics in a $C_3S$ cement powder

Some RVE's with smaller sides were cut out, not maintaining periodical boundaries for the simplicity of calculation. The volume and surface standard deviations, $\sigma$, for both cements are summarized in Tab. 3.4. The standard deviation of surface does not almost depend on the fineness, only the volume standard deviation depends on *w/c*.

| RVE size [$\mu$m] | | 300 | 200 | 100 | 50 | 30 | 20 | 10 |
|---|---|---|---|---|---|---|---|---|
| Number of samples | | 1 | 64 | 64 | 216 | 216 | 216 | 216 |
| $\sigma$ volume [%] | $w/c = 0.2$ | 0 | 0.24 | 1.26 | 3.53 | 5.95 | 8.74 | 17.33 |
| $\sigma$ surface [%] | 500 m²/kg | 0 | 0.36 | 1.86 | 5.29 | 8.5 | 11.97 | 23.6 |
| $\sigma$ volume [%] | $w/c = 0.5$ | 0 | 0.66 | 3.97 | 11.58 | 22.13 | 33.22 | 59.24 |
| $\sigma$ surface [%] | 250 m²/kg | 0 | 0.34 | 1.92 | 5.28 | 9.27 | 12.26 | 26.91 |

Table 3.4: Effect of RVE size in a $C_3S$ cement powder with two finenesses and two $w/c$'s

### 3.4.5  *Effect of microstructure size on hydration and percolation*

As evident from the previous section, the loose microstructure would be more susceptible to the representation size because of higher deviation for volume. The RVE considered as error-free was in this case $100 \times 100 \times 100$ $\mu$m. During the simulation of hydration, the following typical parameters of the model were set as

- hydration under saturated conditions,
- isothermal temperature of $25°C$,
- conversion factor $\beta$ from cycles to time 0.0003.

The relative error of the overall degree of hydration within different RVE sizes is in Fig. 3.7. In acceleratory period, the hydration proceeds quickly and the difference in the hydration degree

in two adjacent cycles is high. After approximately 3 hours, the relative error in the degree of hydration drops below 10 %.
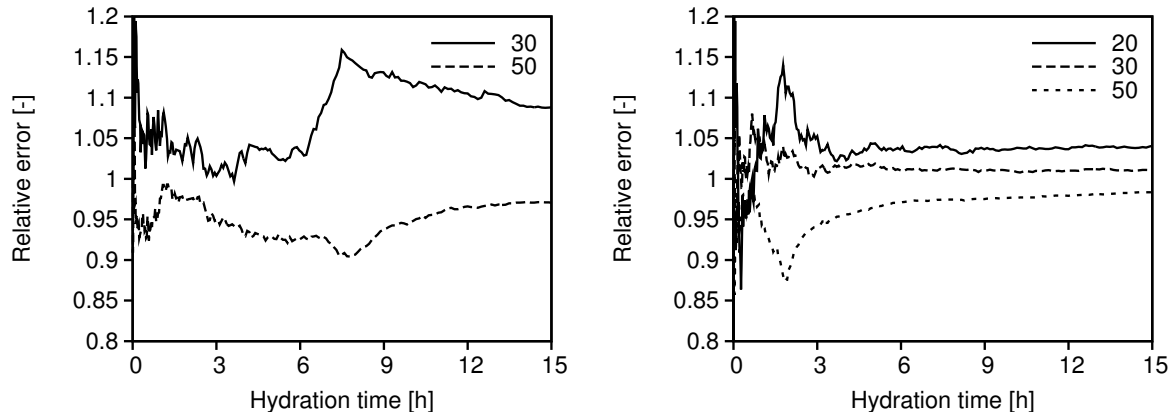


Figure 3.7: Relative error in the degree of hydration in different RVE sizes: coarse cement at $w/c = 0.5$ (left) and fine cement at $w/c = 0.2$ (right)

The worst situation from the statistical point of view emerges at $w/c = 0.5$. Particles have the highest average distance and the degree of hydration would reach one at an infinite time [41]. Unhydrated part of particles with different diameters is in Fig. 3.8, for $w/c = 0.2$ and $0.5$. After 200 hours, the hydration slows down considerably in the microstructure on the right side for the reason of limited capillary place.
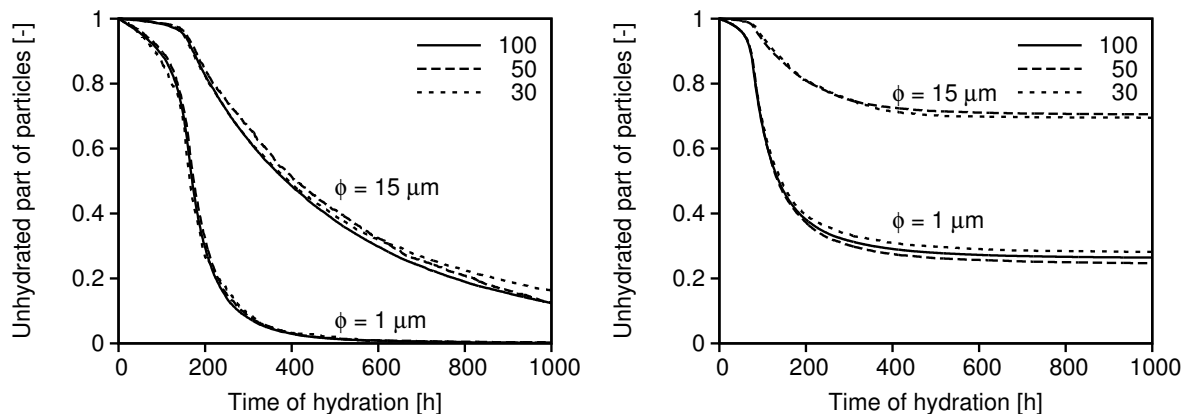


Figure 3.8: Unhydrated part of particles with specified diameter in two microstructures with different RVE sizes: coarse cement at $w/c = 0.5$ (left) and fine cement at $w/c = 0.2$ (right)

The RVE size also influences the connectivity of solid phases, from one RVE size to the opposite, for further details see section 4.2. The volume ratio of connected solid phases to

the total volume of solids is in Fig. 3.9. The smaller RVE has generally higher percolation threshold because large connecting particles of cement grains are missing. Even in $w/c = 0.2$, the difference in percolation threshold is within 20 minutes of hydration.
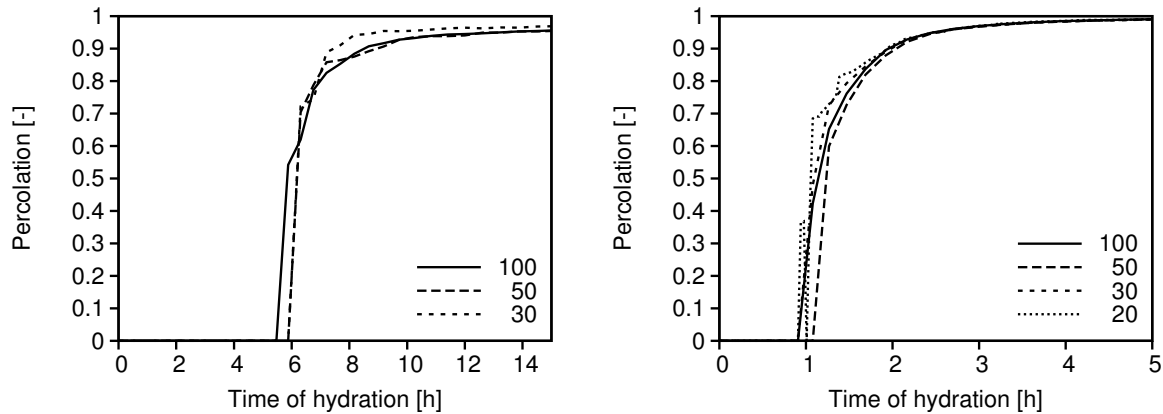


Figure 3.9: Percolation of two microstructures with different RVE sizes: coarse cement at $w/c = 0.5$ (left) and fine cement at $w/c = 0.2$ (right)

The percolation is influenced by the content of alkalis in the cement system and it was showed that the alkali have a dramatic effect on a depercolation of capillary porosity [13]. At the same degree of hydration, the alkali-rich mixtures depercolated sooner than that with lower alkali content. It is believed that the sooner depercolation is responsible for the lath-like morphology of C-S-H which is often observed in alkali-rich systems [13].

Since each microstructural image of the representation is in principle random, statistical evaluation of the degree of hydration should be examined. Again, two microstructures with low and high *w/c* were selected, based on data of Kamali [57]. Fig. 3.10 summarizes the evolution of hydration degree on five realizations of the sizes $10 \times 10 \times 10$ and $50 \times 50 \times 50$ $\mu$m. Fig. 3.11 supports the finding that the statistical fluctuation is more critical in lower *w/c*.

### 3.4.6 Microscale C-S-H model based on a transition thickness

It was recognized that the C-S-H appear in two morphological forms [55], see section 2.5.2. The water proceeds inwards to the cement grain, where more dense hydration matter was observed [113]. On the other hand, the outer hydration products, formed behind the original cement grain, are less dense [104].

One of the way to implement this phenomenon into any stereological hydration model is to reduce the interface of a grain with *transition thickness*, $\delta$. The C-S-H$_{HD}$ is assumed to form inside the original cement grain boundary increased with the transition thickness inwards. This
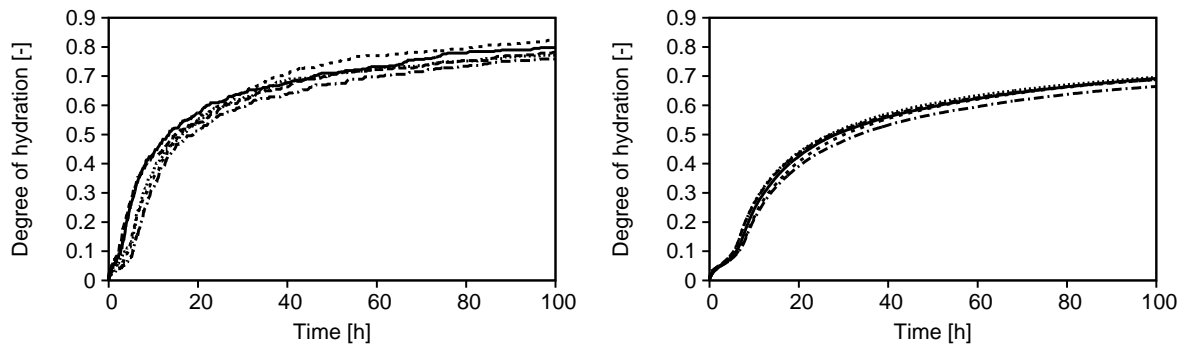
Figure 3.10: Hydration evolution in five realizations for two RVE sizes: $10 \times 10 \times 10$ (left) and $50 \times 50 \times 50$ $\mu$m (right), $w/c = 0.5$, coarse cement 250 m$^2$/kg
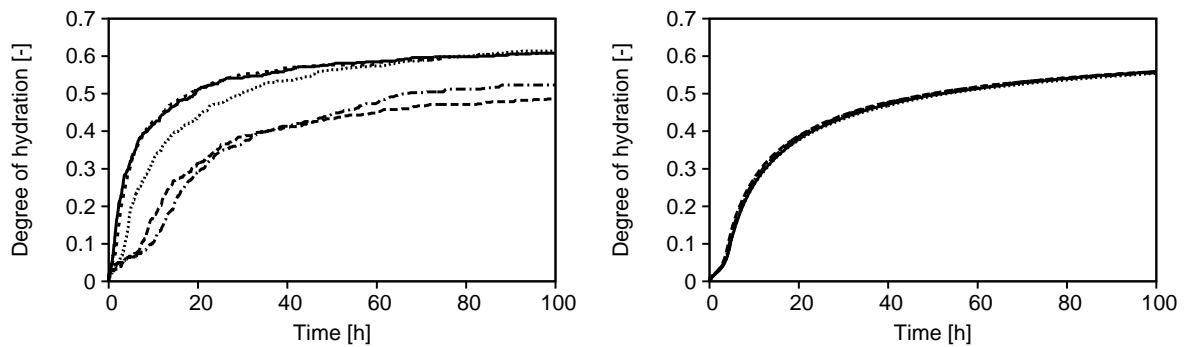


Figure 3.11: Hydration evolution in five realizations for two RVE sizes: $10 \times 10 \times 10$ (left) and $50 \times 50 \times 50$ $\mu$m (right), $w/c = 0.25$, fine cement 500 m$^2$/kg

idea corresponds to a confinement of C-S-H because of dense packing under another shell of hydrates.

The *transition thickness* as a non-integer number must be introduced explicitly and defines the shell thickness above which the only C-S-H$_{LD}$ can form. For example, the $\delta = 0.5$ $\mu$m will cause that C-S-H$_{LD}$ will be always present where a 1 voxel cement particle was originally located. In this particular case, the volume of cement grains appropriate for C-S-H$_{HD}$ origin is reduced by nearly one third, Fig. 3.12.

Van Breugel implements the *transition thickness* in the HYMOSTRUC hydration program, where the reaction changes from a boundary to a diffusion type [21]. For a wide range of cements, $\delta_{tr}$ lies between 2–6 $\mu$m. The penetration front goes in the ratio approximately 1/1.2 on larger cement grains (inner/outer volume). This gives the thickness of change from C-S-H$_{LD}$ to C-S-H$_{HD}$ at the depth of 0.9–2.7 $\mu$m, which roughly corresponds to the observation by Richardson [95] ($5/2 = 2.5$ $\mu$m). On the other hand Richardson [96] argues that inner and

outer products do not correspond to the original cement grain boundaries.

Generally, the beginning of hydration is marked as the domination of C-S-H$_{LD}$. At the later stages of hydration, Tennis and Jennings [113] predicts the ratio of 30/70 (C-S-H$_{HD}$/C-S-H$_{LD}$) in $w/c = 0.5$. Fig. 3.12 demonstrates quantitative behavior of C-S-H$_{LD}$ evolution using CEMHYD3D code. Reactions as well as their stoichiometries are left to the chemical equations implemented in CEMHYD3D that describe an average behavior of various C-S-H phases. The amount of hydrates corresponds in our case only to an average, with no difference between both morphologies.

Three C$_3$S microstructures were examined in a combination of $w/c = 0.3$ and 0.5 with fine (500 m$^2$/kg) and coarse cement (250 m$^2$/kg). The RVE size was chosen as $100 \times 100 \times 100$ $\mu$m, accommodating comfortably larger particles. If $\delta = 0.0$ $\mu$m, about a half is converted to C-S-H$_{HD}$ at later stages, compared to a third of C-S-H$_{HD}$ when $\delta = 1.0$ $\mu$m, Fig. 3.12.
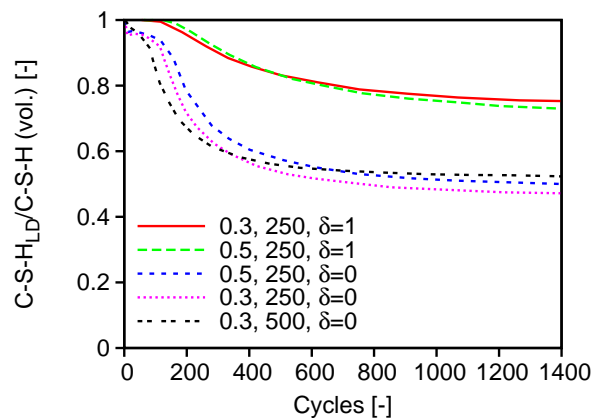


Figure 3.12: Predicted relative volumetric ratio of C-S-H$_{LD}$ in cement pastes based on transition thickness $\delta$ [$\mu$m ], $w/c = 0.3$ and 0.5, fineness 250 and 500 m$^2$/kg

Fig. 3.12 testifies that neither cement fineness nor *w/c* play a significant role in C-S-H$_{LD}$ or C-S-H$_{HD}$ evolution. Higher *w/c* means only higher average distance of the same cement grains so transition thickness acts in the same manner. This model, based on transition thickness, does not conform to the Jennings observation, where the C-S-H$_{HD}$ dominates through the microstructure at low *w/c* in later stages. The proposed model is in contradiction in terms of *w/c* dependence, where much higher portion of C-S-H$_{HD}$ is expected to form when *w/c* decreases.

### 3.4.7 Microscale C-S-H model based on confinement

The previous section showed that the average distance among cement particles must be taken into account when a realistic prediction of C-S-H type should be carried out. It is assumed that

the C-S-H become more compacted when external pressures act due to insufficient capillary pore space. The box size is introduced in CEMHYD3D model that is checked for an amount of solid phases inside. If enough solid phases is found, then all C-S-H voxels inside that box are converted to the C-S-H$_{HD}$. Typically, the box size $3 \times 3 \times 3$ $\mu$m, which is the neighborhood of one voxel, contains the amount of 27 voxels. This view represents physically the confinement condition due to an expansion of hydration products during hydration.

For the verification, the experimental data from cement pastes were used [107]. Tab. 3.5 gives the volumetric cement characteristics used during the simulation. The simulation runs under saturated conditions at a constant temperature of 20°C. The size of the reference RVE is $50 \times 50 \times 50$ $\mu$m.

| Item | Value |
|------|-------|
| $C_3S$ | 53.0 vol. % |
| $C_2S$ | 22.1 vol. % |
| $C_3A$ | 10.9 vol. % |
| $C_4AF$ | 9.0 vol. % |
| Gypsum | 5 vol. % |
| *w/c* | 0.2, 0.3, 0.5 |
| Blaine fineness | 370 m$^2$/kg |
| Activation energy | 37 kJ/mol |

Table 3.5: Portland cement input parameters used in C-S-H model verification [107]

The confinement algorithm rises the following questions: an effect of digital representation on the C-S-H$_{HD}$ formation, box size with the amount of solid voxels inside and the threshold when C-S-H$_{HD}$ begin to form. Fig. 3.13 shows the results of a preliminary study. Three microstructures with *w/c*'s as 0.2, 0.3 and 0.5 were generated using the same cement. One of the clues for the determination of the amount of solids in the box was, that C-S-H$_{HD}$ starts to form at the degree of hydration $\alpha = 0.6$ at $w/c = 0.6$ [17]. When the degree of hydration reaches 0.9, the C-S-H$_{HD}$ fraction is around 25 % in the $w/c = 0.5$. It is obvious that 25 solid voxels in the box of $3 \times 3 \times 3$ is not enough, so the true value must lie above this value, Fig. 3.13. The most probable seems the value close to 27, i.e. complete filling with solid phases.

The effect of box size was explored as the next stage. Two neighborhoods, i.e. $3 \times 3 \times 3$ and $5 \times 5 \times 5$ $\mu$m were checked for the C-S-H$_{HD}$ eligibility. The numerical study on the paste with $w/c = 0.2$ shows that the C-S-H$_{HD}$ evolution rises quicker than within the smaller box. No significant qualitative difference is observed, Fig. 3.13. The same conclusion is valid for

$w/c = 0.3$ and 0.5 (not displayed).

Fig. 3.14 uses a different approach in the box of $3 \times 3 \times 3$. Pure $C_3S$ paste has hydrated at $w/c = 0.25$, with PSD from [57] and in the microstructure size of $25 \times 25 \times 25$ $\mu$m. If only the central C-S-H voxel is transformed, the final volume of the C-S-H$_{HD}$ is insufficient. There is no other way to increase this ratio unless all C-S-H voxels in the box are changed to the C-S-H$_{HD}$. Therefore, changing only central voxel in the box does not seem to be realistic.
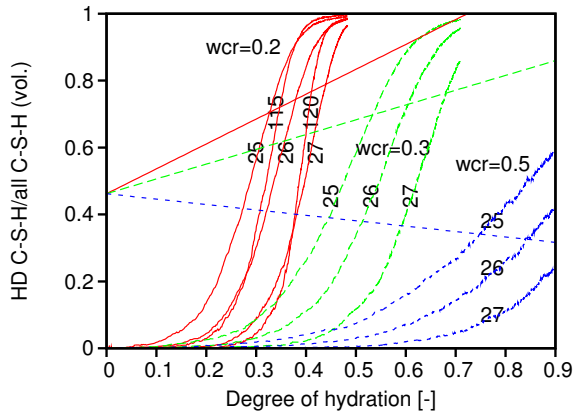


Figure 3.13: C-S-H$_{HD}$ evolution in three *w/c*'s in dependence on surrounding solid volume
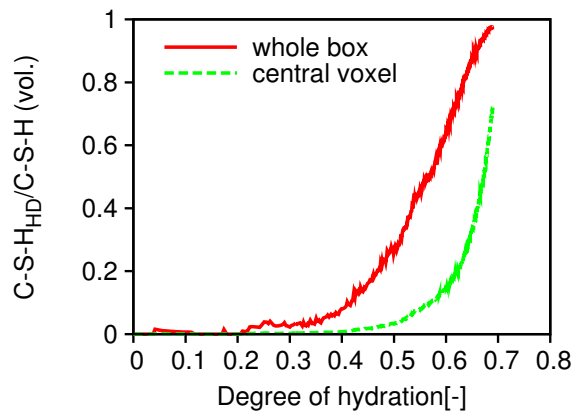
Figure 3.14: C-S-H$_{HD}$ evolution depending on the neighborhood selection

Calibration of the confinement model is based also on Tennis and Jennings' sample data [113]. By nitrogen adsorption technique, they found the mass ratio $M_r$ of C-S-H$_{LD}$/C-S-H as

$$M_r = 3.017\alpha w/c - 1.347\alpha + 0.538. \tag{3.45}$$

This equation is displayed by straight lines in Fig. 3.13. As discussed in section 2.5.2, data from young pastes from [113] are not consistent with the theory of confinement where the beginning of hydration produces no C-S-H$_{HD}$. On the other hand, lines intersect at the value of 0.462 at the beginning of hydration. It is believed that the value of 27 voxels is the most appropriate one for the description of C-S-H$_{HD}$ formation. The box $5 \times 5 \times 5$ provides no quantitatively different result either, see Fig. 3.13 for 115 and 120 solid voxels in the enlarged box.

Chapter 4

# HOMOGENIZATION OF CEMENT-BASED MATERIALS

The theory of homogenization generally transfers information from the lower heterogeneous material level to the higher one [117]. Heterogeneous material is either composed of different phases or of material in different states, such as polycrystals. The homogenization will focus on multiscale analysis of cementitious materials due to the fact that typical levels may be found at separable and remarkable length scales

**C-S-H level** typically spans the characteristic length between 10 nm – 1 $\mu$m [17]. Two morphologies of C-S-H$_{LD}$ and C-S-H$_{HD}$ were found,

**cement paste level** is found on the scale of 1 $\mu$m – 100 $\mu$m. Clinker minerals, gypsum, CH, homogenized C-S-H and some capillary porosity are present [17],

**mortar level** is considered on the scale between 1 mm and 1 cm. It contains homogenized cement paste, fine aggregates such as sand and associated ITZ. Air voids may be found too,

**concrete level** spans in typical concrete the characteristic length of 1 cm – 1 dm. Mortar, coarse aggregates such as gravel and associated ITZ are typically found.

The above mentioned level separation may be expressed in the theory of homogenization as

$$d_o \ll d \ll l \ll L, \quad l \ll \lambda, \tag{4.1}$$

where $d_0$ is the smallest size under which continuum mechanics is not valid, $d$ is the characteristic length of inhomogeneities or deformation mechanisms, $l$ is the RVE size, $L$ is the dimension of the whole body of material and $\lambda$ is the fluctuation length of material properties. The homogenization methodology presented here assumes that the heterogeneous material obeys three principles [134]

**ergodic hypotheses** requires that an ensemble average of any function corresponds to a member average in an ensemble. This hypothesis reduces the ensemble to the member in ensemble under the condition that the member is sufficiently large. The member corresponds than to RVE. In the case of periodic medium, this assumption is automatically satisfied when selecting periodic unit cell as the member,
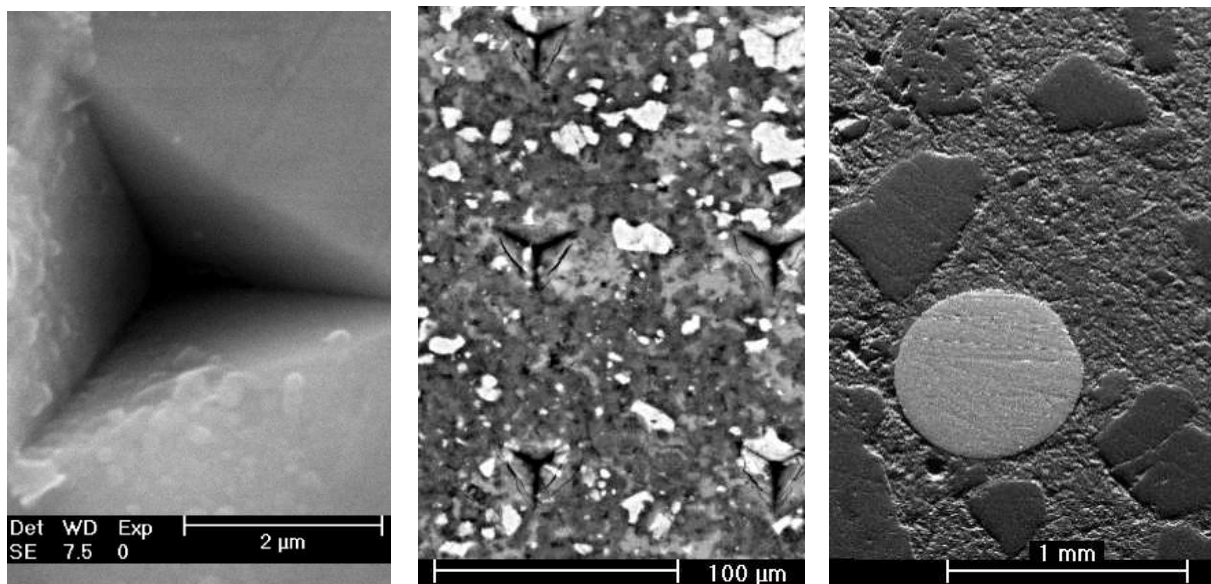
Figure 4.1: Images of C-S-H, cement paste and mortar level with indents and a steel fiber (images by L. Kopecký)

**statistical homogeneity** which requires that some function average related to the RVE is invariant with respect to translation,

**statistical isotropy** is a narrower restriction to the condition of statistical homogeneity; the function average in the RVE is invariant in addition with respect to rotation. Probably only highly anisotropic elastic properties of portlandite may violate this assumption at the cement paste level.

Cement paste starts as a disconnected, heterogeneous material that hardens after its setting. This situation is complicated for homogenization since the material changes its porosity, connectedness and chemical phases during hydration. A random evolving microstructure could be described in terms of $n$-point probability functions or lineal path function, e.g. [134]. For our purposes, there is no need to do so since the simulated evolving 3D microstructure with finite resolution will be used directly in the most cases.

The details of cement microstructure remain hidden in virtually all situations hence the correlation functions of $n^{th}$ order are usually unknown. Generally, higher than the second order correlation functions significantly improve RVE description since they include information about phase connectivity. The bounds calculated from homogenization would be useful in decision whether the system is above or below the percolation threshold [117]. The shortcoming of high-order functions exists in the case of high contrast properties among phases, typically for porous materials, where the upper bound diverges [117].

Traditional view of homogenization was based on limited microstructural information such as volume fractions of components. This was a typical situation of cementitious materials where the microstructure was captured only by simple models, often with unavailable microstructural details. Using the Powers model coupled with KJMA equation for the cement hydration, the volumetric phases may be easily determined as an input in some homogenization procedures [17]. However, the assumptions of homogenization schemes reflect some ideal configuration of microstructures leading to discrepancies with the real shape. Typical representatives of such analytical homogenization methods are the rule of mixtures [71], Hashin-Shtrikman bounds [44], Mori-Tanaka [75] or self-consistent [51] method, discussed in chapter 5 and validated in chapter 7.

A replacement of assumptions used in analytical homogenization methods with the real microstructure leads to a significant refinement of results. The validity of results may be checked and compared with the bounds predicted for some special configurations. The key term is the representative volume element (RVE) that captures and analyzes a limited piece of a heterogeneous material. Then, the numerical methods can be used to calculate the fluctuations of stress or strain field to bridge the characteristic length of material. This approach will be referred to as a numerical homogenization, chapter 6.

### 4.1 Representative volume element of cement paste

The key task in material analysis is an appropriate selection complying to ergodic and statistical homogeneity assumptions. In fact, the representative volume element, coined by Hill [50], is usually smaller than by its definition, which was noted and explored by Huet [52]. Huet introduced the term *apparent properties* and the effect of various boundary conditions on the overall response was carried out for elastic materials [46]. Kanit *et al.* [58] studied the effect of boundary conditions in significantly smaller RVE's and concluded that the overall response may be approximated by a certain amount of random realizations. Generally, the size of the RVE is a function of five parameters: the analyzed physical quantity, the contrast of material properties, the volume fraction of components, the relative error and the amount of realizations of random microstructure [58]. The determination of an appropriate RVE size in cement-based materials is therefore error-based, specific to each microstructure of cement paste.

Since nearly all hydration models work on a periodic microstructure, the RVE size is introduced unambiguously. Such representative volume typically undergoes a homogenization process, i.e. simulated size of $100 \times 100 \times 100$ voxels corresponds to the same RVE. The periodic RVE makes possible to impose periodic boundary conditions without any difficulties. In the numerical homogenization, chapter 6, the hexahedral finite element in the form of a

voxel will be used inside the RVE. The study of RVE appropriate size in terms of hydration is demonstrated in section 3.4.5, in terms of homogenization in chapter 7.

The largest RVE size is limited by computer capacities, i.e. current single 32-bit computers with 3.2 GB of memory. The RVE may be as large as approximately $75 \times 75 \times 75$ of hexahedral finite elements with tri-linear interpolation function when using a single computer. The FFT-based homogenization allows approximately up to $230 \times 230 \times 230$ material points. Parallel computation solves partially these problems, consuming even more computation time. For the elastic homogenization of matured cement paste, a reasonable size is about $50 \times 50 \times 50\ \mu$m, chapter 6.

### 4.2   Percolation of solids

Percolation theory describes topological connection in a random material of at least two phases [117]. There exists a strong link between the behavior of a random material and perco-lation, e.g. elasticity, conductivity, permeability [117]. When applied to cement paste [20, 94], percolation of solids $p$, further referred to as the percolation, is quantified as

$$p = \frac{\text{connected volume of solids}}{\text{total volume of solids}}. \tag{4.2}$$

At the onset of hydration, the cement grains are mutually separated hence connected volume fraction and percolation of solids is equal to zero. As hydration proceeds, the hydration products glue the grains. At the point called the percolation threshold of solids $p_c$, the microstructure contains sufficient amount of solids to bridge one RVE side to the opposite one.

The experimental data of early aged cement systems describing the microstructure connect-edness are not available in general. The lattice percolation theory predicts theoretical Young's modulus evolution in an asymptotic vicinity of the percolation threshold in 3D as [117]

$$E \sim (p - p_c)^{3.75}. \tag{4.3}$$

Note that Eq. (4.3) is rigorously valid within the same medium. For the cement paste, the validity is restricted to early ages only since hydration changes volume fractions with different elastic properties.

Torrenti and Benboudjema [118] argue that the approach based on Eq. (4.3) is not correct since low *w/c* may exhibit solid percolation already before the onset of hydration but there is not necessary the cohesion between cement grains. Therefore, an additional parameter capturing the cohesion should be introduced. Their conclusion is valid for a finite resolution, where tiny details about microstructure are lost. This situation is circumvented in CEMHYD3D by an

introduction of ID numbers to cements grains so any unflocculated cement paste always starts from a liquid form.

The percolation threshold may be computed with the help of real connected volume fraction in the RVE. Hence the mechanical properties originate after the percolation threshold, i.e. as soon as the first cluster of connected phase bridges the microstructure. Garboczi and Bentz [37] formulated burning algorithm to assess the solid percolation in CEMHYD3D. The algorithm starts at one side of the RVE and marks the passed voxels as burnt. The burning front proceeds to connected voxels as long as there is something to burn. If the opposite side is reached, the RVE is percolated. In this particular case, the percolation is generally different in three principal directions.

The percolation may be related to Vicat needle penetration test [37]. As soon as the first spanning cluster appears, the cement paste starts to stiffen. The reconstructed microstructure $50 \times 50 \times 50$ $\mu$m of Princigallo [94] at $w/c = 0.375$ is an example, where Vicat needle test took place. Fig. 4.2 displays the results from calorimetry with associated simulation and the results from Vicat needle test. The percolation has typically very steep evolution in its beginning and the first cluster appears when about 40 % of solid phases is percolated. The differences in three principal directions are not significant for such microstructure size.
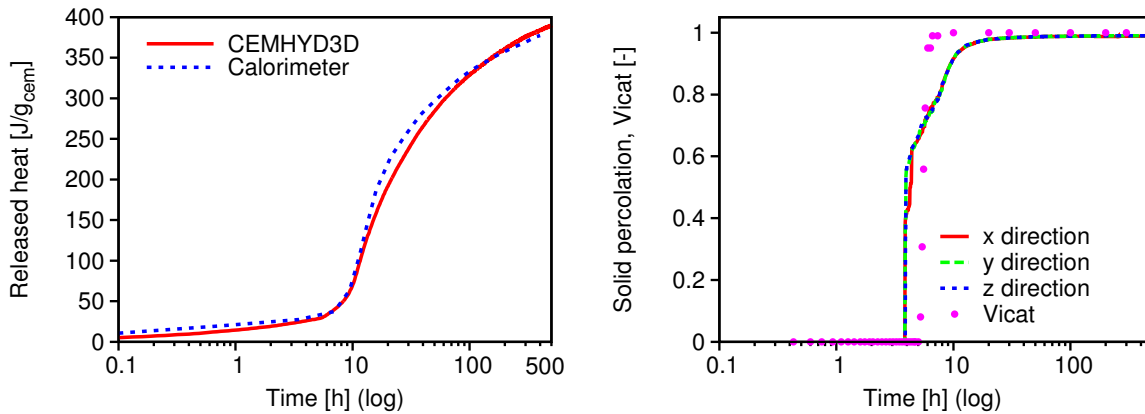


Figure 4.2: Released heat, simulation and typical percolation curve with corresponding Vicat needle penetration test [94]

The percolation threshold, i.e. the point where the first spanning cluster appears, may be related to the degree of hydration. Since that time, the mechanical properties evolve. Boumiz *et al.* [20] measured vacuum pumped cement paste specimens by an acoustic wave technique and released heat by means of calorimetry. He found $\alpha$ for white cement paste that corresponds to the percolation threshold: $\alpha = 0.015$ for $w/c = 0.35$ and $\alpha = 0.021$ for $w/c = 0.4$. Similar values were found via CEMHYD3D simulation of cement pastes. The results are summarized

in Tab. 4.1 for percolation in three principal directions. The ranges of values have their origin in the anisotropy.

| w/c | Degree of hydration | Percolated fraction of solids | Source |
|-----|---------------------|-------------------------------|--------|
| 0.2 | 0.009230 – 0.013387 | 0.3033 – 0.618 | [107], CEMHYD3D |
| 0.3 | 0.009230 – 0.013914 | 0.3033 – 0.617 | [107], CEMHYD3D |
| 0.35 | 0.015 | – | [20] |
| 0.40 | 0.021 | – | [20] |
| 0.5 | 0.021400 – 0.029597 | 0.2561 – 0.600 | [107], CEMHYD3D |

Table 4.1: Determination of degree of hydration at the solid percolation threshold

Upper range of percolated solid fraction corresponds roughly to value 0.5, as proposed by Garboczi [8]. Bentz *et al.* studied the effect of PSD in *w/c* in the range from 0.246 to 0.5 [11]. They found the degree of hydration corresponding to the percolation threshold to be in the range from 0.011 to 0.089. The latter value is for the particle diameter of 5 $\mu$m. When the average grain size of PSD is lower, the higher degree of hydration is required to connect the microstructure. These results are in accordance with Tab. 4.1 for a broad PSD of Portland cements. The linear fit of Tab. 4.1 leads to

$$\text{Degree of hydration at the solid percolation threshold} = 0.0485 \, w/c, \qquad (4.4)$$

with the correlation coefficient of 0.937.

### 4.3 Intrinsic properties of constituents

The intrinsic properties of individual components are a prerequisite for a homogenization problem. One of the way to access the intrinsic mechanical values is the ultrasonic pulse velocity measurement method (UPV), which is a non-destructive method based on the recalculation from known velocity and density of material $\rho$. Since the relation is derived from a continuum, the sample should be homogeneous on the scale of measurement. For an isotropic material the relation between longitudinal, shear UPV velocities and Lamé's constants $\lambda, \mu$ are

$$v_l \;=\; \sqrt{\frac{\lambda + 2\mu}{\rho}}, \qquad (4.5)$$

$$v_s \;=\; \sqrt{\frac{\mu}{\rho}}. \qquad (4.6)$$

$$(4.7)$$

The elastic properties obtained from UPV experiments are often called dynamic moduli and according to [62], the dynamic $E$ modulus is higher than the static one for concrete probably due to short-term creep [4]. The ratio $E_{dyn}/E_{stat}$ varies from 1.5 to 1.7 for equivalent concrete ages greater than 50 h. It is often found that the dependence of both moduli is almost linear with the degree of hydration [62]. Above the hydration degree of 0.4, the rate of grow might be lower. The extrapolation of elastic properties to early ages might be misleading, e.g. linear extrapolation of the origin of static modulus points to the degree of hydration of 0.05, but yields degree of hydration of 0.20 by a quadratic extrapolation for the same concrete [62]. Mindness [73] and Nagy [78] also found that UPV provides usually a higher modulus of elasticity up to 30 % than that determined by high strain static testing, e.g. ASTM C597. Therefore, these non-destructive techniques are not generally recommended in practice but are very valuable in modeling. The difference is partially attributed to a short-term creep phenomenon, especially to C-S-H phases [4].

### 4.3.1   C-S-H mechanical properties

The C-S-H phases are intimately mixed with porosity and small CH crystals hence the results are sensitive to a selection of the cement paste region. Constantinides and Ulm [24] performed a set of nanoindentation tests on OPC, $w/c = 0.5$, and they obtained data in Fig. 4.3. They concluded that there are two types of C-S-H, assigning them properties in terms of Young's modulus: C-S-H$_{LD}$ $\sim 21.7 \pm 2$ GPa and C-S-H$_{HD}$ $\sim 29.4 \pm 2.4$ GPa. Poisson ratio was determined as 0.24 for both types. Acker [1] measured intrinsic properties of both types of C-S-H with the results of $20 \pm 2$ GPa and $31 \pm 4$ GPa.
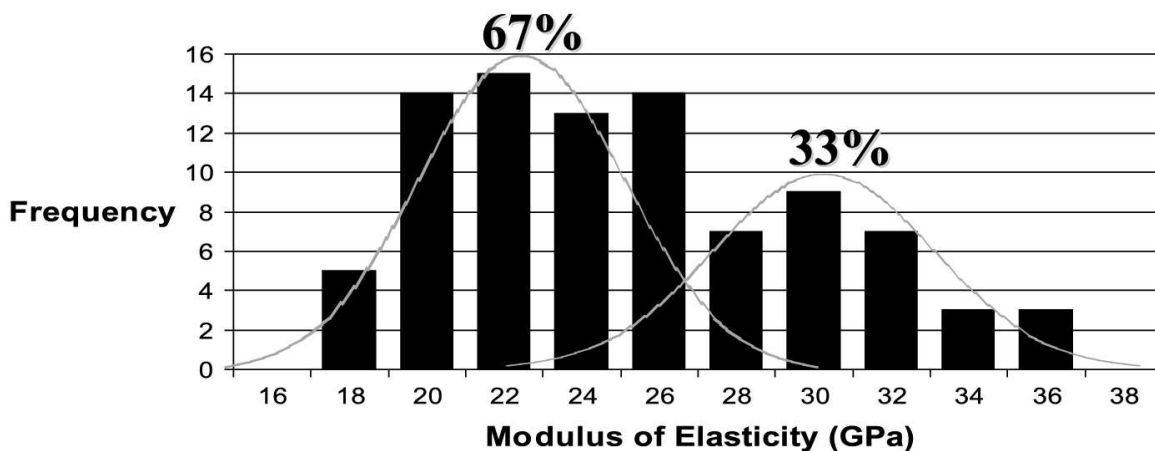


Figure 4.3: C-S-H nanoindentation data, $w/c = 0.5$, after [24]

The C-S-H experimental results may be explained using the J-T model, where both C-S-H forms are constructed from the same building unit [113]. According to the J-T model, two gel porosities for C-S-H$_{LD}$ and C-S-H$_{HD}$ are 0.42 and 0.3, respectively. When the nanoindentation results are correct, the homogenization at the C-S-H level from the building units would predict similar results. Unknown elastic properties of building units may be found with an inverse homogenization problem. Indeed, the C-S-H morphology resembles a matrix-inclusion assemblage. Therefore the analytical Mori-Tanaka [75] homogenization theory may be applied with the reference medium of C-S-H$_{LD}$ (C-S-H$_{LD}$ as a matrix with spherical porous inclusions). In addition, the self-consistent scheme is checked without any reference phase. Tab. 4.2 summarizes intrinsic values and downscaled intrinsic values using both schemes for the building units. The independent nanoindentation results of both morphologies yielded nearly the same stiffness of solid building units via the Mori-Tanaka scheme. This coincidence suggests that nanoindentation, J-T model and the Mori-Tanaka scheme captures a true behavior. If so, the data from porosimetry may be used to reconstruct the C-S-H structure and to predict its mechanical behavior.

|  | C-S-H nanoindentation | Porosity (J-T) | Building units |
|---|---|---|---|
| Fraction in C-S-H$_{LD}$ | - | 0.42 | 0.58 |
| Young's modulus, E | 21.7 GPa | 0.001 | **53.22 - MT** (137.4-SCS) |
| Poisson's ratio, $\nu$ | 0.24 | 0.001 (0.499) | **0.265 - MT** (0.37-SCS) |
| Fraction in C-S-H$_{HD}$ | - | 0.30 | 0.70 |
| Young's modulus, E | 29.4 GPa | 0.001 | **54.69 - MT** (73.77 - SCS) |
| Poisson's ratio, $\nu$ | 0.24 | 0.001 (0.499) | **0.257 - MT** (0.277 - SCS) |

Table 4.2: Downscaling of C-S-H$_{LD}$ and C-S-H$_{HD}$ to the building units using Mori-Tanaka and self-consistent scheme

### 4.3.2 Cement paste level

The intrinsic elastic properties of cement paste level are important especially for unhydrated clinker minerals and portlandite. Characteristic porosity of a phase is included in intrinsic properties. However, little data is available on the intrinsic porosity of raw cement clinker. Theisen and Smidth [111] report porosity from 5 up to 25 vol. % for alite and belite, but including void pores in epoxy resin.

Velez *et al.* [123] measured the elastic values of clinker minerals as they appear in Portland cement by nanoindentation and by means of the resonance frequency. They verified that

there is no creep at constant force and low scatter of nanoindentation values. Poisson's ratio is assumed to be of 0.3 for all clinker minerals. Intrinsic data of CH were measured by several researchers [1, 5, 128], see [17] for comprehensive results.

| Phase | $E$ (nanoind.) (mechanical) | $\nu$ | $E$ (resonance) | Porosity [%] | Ref. |
|---|---|---|---|---|---|
| $C_3S$ | **135**±7 | **0.3** | 147±5 | - | [123] |
| $C_2S$ | **130**±20 | **0.3** | 140±10 | - | [123] |
| $C_3A$ | **145**±10 | **0.3** | 160±10 | - | [123] |
| $C_4AF$ | **125**±25 | **0.3** | - | - | [123] |
| $C\overline{S}H_2$ | 16-**30**-35 | 0.18-**0.3**-0.34 | - | 3.5–7.5 | [7] |
| Porosity$^a$ | **$10^{-3}$** | **0.499924** | - | - | - |
|  | **$10^{-3}$** | **$10^{-3}$** | - | - | - |
| CH | **38**±5 | **0.305**-0.325 | - | - | [24] |
| $C\text{-}S\text{-}H_{LD}$ | **21.7**±2.2 | **0.24** | - | - | [24] |
| $C\text{-}S\text{-}H_{HD}$ | **29.4**±2.4 | **0.24** | - | - | [24] |
| $C_6A\overline{S}_3H_{32}$ | **22.4** | **0.25** | - | - | [57] |
| $C_4A\overline{S}H_{12}$ | **42.3** | **0.324** | - | - | [57] |
| $C_3AH_6$ | **22.4** | **0.25** | - | - | * |
| $FH_3$ | **22.4** | **0.25** | - | - | * |

Table 4.3: Intrinsic elastic moduli of chemical phases as measured by nanoindentation, resonance frequency or mechanical tests. The Young moduli $E$ with the standard deviation or range are in GPa. **Bold** values are used in homogenization, * values are estimated, based on [57], $^a$ is the water-filled porosity or the void, see further discussion

The study of portlandite crystal revealed that its structure is in the form of a trigonal lattice. For such topographical configuration, linear elastic analysis based on density functional theory was performed [65]. Six independent constants may be used for the reconstruction of stiffness tensor. The global minimum value of Young's modulus is 22.56 GPa when the angle between $c$-axis of crystal and the direction of deformation is 39.82°. The global maximum has the modulus of 99.39 GPa in the perpendicular direction to $c$-axis. The stiffness tensor of portlandite has the

following structure and numerically equals to [65]

$$
\mathbf{C}_{ij} = \begin{pmatrix}
c_{11} & c_{12} & c_{13} & c_{14} & 0 & 0 \\
c_{12} & c_{11} & c_{13} & -c_{14} & 0 & 0 \\
c_{13} & c_{13} & c_{33} & 0 & 0 & 0 \\
c_{14} & -c_{14} & 0 & c_{44} & 0 & 0 \\
0 & 0 & 0 & 0 & c_{44} & |c_{14}| \\
0 & 0 & 0 & 0 & |c_{14}| & \frac{1}{2}(c_{11} - c_{12})
\end{pmatrix} =
\begin{pmatrix}
99.39 & 30.78 & 7.36 & 0 & 0 & 0 \\
30.78 & 99.39 & 7.36 & 0 & 0 & 0 \\
7.36 & 7.36 & 36.29 & 0 & 0 & 0 \\
0 & 0 & 0 & 7.88 & 0 & 0 \\
0 & 0 & 0 & 0 & 7.88 & 0 \\
0 & 0 & 0 & 0 & 0 & 34.31
\end{pmatrix}.
\tag{4.8}
$$

The porosity presents a serious problem in the homogenization since it is in fact not a solid phase. There are two types of porosities in the CEMHYD3D model; a water-filled porosity and an empty porosity. While the water-filled porosity originates from mix water, the empty porosity appears due to the depletion of water for hydration.

The elastic properties of water strongly influence the results for an early hydration period, especially of Poisson's ratio [17]. The water in the RVE cannot move freely out which is in contradiction with the real cement paste at the beginning of hydration, especially during the mechanical testing and resembles the problem of a saturated soil consolidation. If the water movement is not restricted, the water should act in the micromechanical model as a void to enable the compression.

Since presented analytical homogenization methods do not consider implicitly the depercolation of pore space, the water might be considered as a void so the percolation threshold remains at 50 % of porosity of the self-consistent scheme. The Poisson ratio will then increase during the whole hydration as the consequence of chosen water properties. Giving the water its real elastic properties results in the decrease of Poisson's ratio from the value of 0.5, on the other hand, the percolation threshold of the self-consistence scheme is higher than 50 % of the water-filled porosity.

In the numerical homogenization, the water-filled pores can have the bulk modulus of water ($k = 2.18$ GPa) since the microstructure contains information about the connectivity of pores and the strain may localize in empty pores. The next consequence of chosen porosity properties is the speed convergence of FEM and FFT-based numerical homogenization methods since the selection determines the contrast of phases.

Chapter 5

# ANALYTICAL HOMOGENIZATION METHODS

The methods of continuum mechanics relate the linear and nonlinear behavior at the fundamental level (phase or single crystal) with the macroscopic scale. Finding the effective physical properties of composites is a classical engineering problem, where the domains of a heterogeneous material have different properties. The domain size is much larger than the molecular dimensions and smaller than the macroscopic sample so these length scales can be viewed as a continuum, Eq. (4.1). Empirical relations were found good for data correlation rather than for prediction [116]. The microstructure configuration determines the effective properties in addition to the volumetric fractions of the material domains. The most important, but not the only one, is the volume fraction, or the result of one point autocorrelation function.

The continuum mechanics rely on the concept of concentration which is able to derive the local stress or strain fields $\boldsymbol{\sigma}(\boldsymbol{x})$, $\boldsymbol{\varepsilon}(\boldsymbol{x})$ from the macroscopic ones $\boldsymbol{\Sigma}$ and $\boldsymbol{E}$. This problem cannot be solved in general, so additional assumption is made which leads to an *estimate* or to a *bound*. In the case of estimates, the boundary conditions of inclusion are generally unknown, so the problem is firstly transformed to the problem with homogeneous boundary conditions [43, 51]. In the case of stress homogeneous boundary condition

$$\boldsymbol{p}(\boldsymbol{x}) = \boldsymbol{\Sigma}\boldsymbol{n}, \tag{5.1}$$

where $\boldsymbol{n}$ is the unit outward at the boundary and $\boldsymbol{p}$ are surface tractions. For any equilibrated stress filed $\boldsymbol{\sigma}(\boldsymbol{x})$, the volume average yields back the homogeneous stress

$$\langle \boldsymbol{\sigma} \rangle = \frac{1}{V} \int_V \boldsymbol{\sigma}(\boldsymbol{x}) \mathrm{d}V = \boldsymbol{\Sigma}. \tag{5.2}$$

Similarly a macroscopic strain can be imposed through surface displacements, which is referred to as Hashin-type boundary condition

$$\boldsymbol{u}(\boldsymbol{x}) = \boldsymbol{E}\boldsymbol{x}, \tag{5.3}$$

where $\boldsymbol{u}(\boldsymbol{x})$ is microscopic displacement vector and $\boldsymbol{x}$ determines its position. For any strain field $\boldsymbol{\varepsilon}(\boldsymbol{x})$ derived from any compatible displacement field according to Eq. (5.3), the macroscopic strain then reads

$$\langle \boldsymbol{\varepsilon} \rangle = \frac{1}{V} \int_V \boldsymbol{\varepsilon}(\boldsymbol{x}) \mathrm{d}V = \boldsymbol{E}. \tag{5.4}$$

The homogeneous boundary conditions according to Eqs. (5.1), (5.3) enable to use the Hill lemma for the strain energy density, where at least strain or stress field satisfies homogeneous boundary conditions

$$\langle \boldsymbol{\sigma}(\boldsymbol{x}) : \boldsymbol{\varepsilon}(\boldsymbol{x}) \rangle = \langle \boldsymbol{\sigma}(\boldsymbol{x}) \rangle : \langle \boldsymbol{\varepsilon}(\boldsymbol{x}) \rangle = \boldsymbol{\Sigma} : \boldsymbol{E}. \tag{5.5}$$

The conditions of validity of Eq. (5.5) may be extended to periodic boundary conditions as well [133]. In continuum micromechanics, the approximate microscopic stress or strain field may be linked to the macroscopic one by means of strain $\mathbf{A}(\boldsymbol{x})$ or stress $\mathbf{B}(\boldsymbol{x})$ localization (concentration) tensors in the case of linear elasticity

$$\boldsymbol{\varepsilon}(\boldsymbol{x}) = \mathbf{A}(\boldsymbol{x}) : \boldsymbol{E}, \tag{5.6}$$

$$\boldsymbol{\sigma}(\boldsymbol{x}) = \mathbf{B}(\boldsymbol{x}) : \boldsymbol{\Sigma}. \tag{5.7}$$

Eqs. (5.2), (5.4) imply that

$$\langle \mathbf{A}(\boldsymbol{x}) \rangle = \langle \mathbf{B}(\boldsymbol{x}) \rangle = \mathbf{I}. \tag{5.8}$$

Combining Eq. (5.5) with Eqs. (5.4), (5.6) and subsequently with Eqs. (5.2), (5.7) yields

$$\boldsymbol{E} : \boldsymbol{\Sigma} = \langle \boldsymbol{\varepsilon}(\boldsymbol{x}) : \boldsymbol{\sigma}(\boldsymbol{x}) \rangle = \langle \boldsymbol{\varepsilon}(\boldsymbol{x}) : \mathbf{B}(\boldsymbol{x}) : \boldsymbol{\Sigma} \rangle, \tag{5.9}$$

$$\boldsymbol{\Sigma} : \boldsymbol{E} = \langle \boldsymbol{\sigma}(\boldsymbol{x}) : \boldsymbol{\varepsilon}(\boldsymbol{x}) \rangle = \langle \boldsymbol{\sigma}(\boldsymbol{x}) : \mathbf{A}(\boldsymbol{x}) : \boldsymbol{E} \rangle. \tag{5.10}$$

Eqs. (5.9), (5.10) lead to the same results in heterogeneous materials only in sufficiently large samples. If not so, which is usually the case of representation in numerical analysis, the results may be far apart and depend on boundary conditions [58]. This is discussed in section 6.3. Let us define local constitutive equations (relating average microscopic strain with stress at microscopic level)

$$\boldsymbol{\sigma}(\boldsymbol{x}) = \mathbf{c}(\boldsymbol{x}) : \boldsymbol{\varepsilon}(\boldsymbol{x}), \tag{5.11}$$

$$\boldsymbol{\varepsilon}(\boldsymbol{x}) = \mathbf{s}(\boldsymbol{x}) : \boldsymbol{\sigma}(\boldsymbol{x}), \tag{5.12}$$

where $\mathbf{c}(\boldsymbol{x})$ and $\mathbf{s}(\boldsymbol{x})$ are the local stiffness and compliance tensors, respectively.

Inserting Eq. (5.6) into Eqs. (5.11), (5.2) and Eq. (5.7) into Eqs. (5.12), (5.4) leads to the effective stiffness and compliance tensors. Since a heterogeneous sample is often formed from $r$ phases with $f_r$ volume fractions, it is possible to replace integral with a summation

$$\boldsymbol{\Sigma} = \langle \boldsymbol{\sigma} \rangle = \frac{1}{V} \int_V \mathbf{c}_r : \mathbf{A}_r : \boldsymbol{E} \, \mathrm{d}V = \sum_r f_r \mathbf{c}_r : \mathbf{A}_r : \boldsymbol{E} = \mathbf{C}^{eff} : \boldsymbol{E}, \tag{5.13}$$

$$\boldsymbol{E} = \langle \boldsymbol{\varepsilon} \rangle = \frac{1}{V} \int_V \mathbf{s}_r : \mathbf{B}_r : \boldsymbol{\Sigma} \, \mathrm{d}V = \sum_r f_r \mathbf{s}_r : \mathbf{B}_r : \boldsymbol{\Sigma} = \mathbf{S}^{eff} : \boldsymbol{\Sigma}. \tag{5.14}$$

Following Eshelby's idea [31], an estimate for the concentration tensor $\mathbf{A}_r^{est}$ is obtained from the solution of matrix-inclusion problem. If an inclusion has a spherical or ellipsoidal shape and is embedded in a reference medium with the stiffness tensor $\mathbf{C}_0$, the strain field $\varepsilon_r$ in the inclusion is uniform from far imposed homogeneous strain. Such approach leads to an estimate of elastic properties. The most common choice for localization tensor is the Eshelbian type ellipsoidal inclusion placed in a reference medium [133]

$$\mathbf{A}_r^{est} = \left[\mathbf{I} + \mathbf{S}_r^{Esh} : \left(\mathbf{C}_0^{-1} : \mathbf{c}_r - \mathbf{I}\right)\right]^{-1} : \left\langle \left[\mathbf{I} + \mathbf{S}_r^{Esh} : \left(\mathbf{C}_0^{-1} : \mathbf{c}_r - \mathbf{I}\right)\right]^{-1} \right\rangle^{-1}. \qquad (5.15)$$

The Eshelby tensor $\mathbf{S}_r^{Esh}$ depends on the geometry and phase orientation. During the next analysis, this tensor is considered to be of spherical inclusion type in isotropic media since the cement paste resembles this type of morphology [17]. The Eshelby tensor is then composed of volumetric and deviatoric parts

$$\mathbf{S}_r^{Esh} = \alpha_0 \mathbf{J} + \beta_0 \mathbf{K}, \qquad (5.16)$$

$$\alpha_0 = \frac{3k_0}{3k_0 + 4\mu_0}, \qquad (5.17)$$

$$\beta_0 = \frac{6k_0 + 12\mu_0}{15k_0 + 20\mu_0}, \qquad (5.18)$$

where $k_0, \mu_0$ are the bulk and shear moduli of a reference medium and $\mathbf{J}, \mathbf{K}$ are the volumetric and deviatoric parts of a unity tensor $\mathbf{I}$: $\mathbf{J}_{ijkl} = (1/3)\, \delta_{ij}\delta_{kl}$ and $\mathbf{K} = \mathbf{I}$ - $\mathbf{J}$, where $\delta_{ij}$ represents the Kronecker delta. Similarly, the stiffness tensor of the reference phase may be decomposed

$$\mathbf{C_r} = 3k_r\mathbf{J} + 2\mu_r\mathbf{K}. \qquad (5.19)$$

The following relations between the elastic constants of the isotropic material are useful when constructing the stiffness tensor from the Young modulus and the Poisson ratio

$$E = \frac{9k\mu}{3k + \mu}, \qquad (5.20)$$

$$\nu = \frac{3k - 2\mu}{6k + 2\mu}, \qquad (5.21)$$

$$k = \frac{E}{3(1 - 2\nu)}, \qquad (5.22)$$

$$\mu = \frac{E}{2(1 + \nu)}. \qquad (5.23)$$

### 5.1 Rule of mixtures

The rule of mixtures is the first known micromechanical model, stated by Voigt in 1887. It corresponds to a parallel alignment of phases where the localization tensor is estimated as $\mathbf{A} = \mathbf{I}$

$$k = \sum_i k_i f_i, \tag{5.24}$$

$$\mu = \sum_i \mu_i f_i, \tag{5.25}$$

where $k$ is the bulk modulus, $\mu$ the shear modulus and $f$ the volume fraction of individual phases. In the case of serial alignment and perfect bonding, the Reuss estimation with $\mathbf{B} = \mathbf{I}$ is recovered

$$\frac{1}{k} = \sum_i \frac{f_i}{k_i}, \tag{5.26}$$

$$\frac{1}{\mu} = \sum_i \frac{f_i}{\mu_i}. \tag{5.27}$$

Although seeming as an oversimplification, the rules of mixture yield the bounds that cannot be exceeded in the case of elastic isotropic material by any other homogenization method. Fig. 7.4 gives an example of upper bound in a real hydrating cement paste.

### 5.2 Hashin-Shtrikman and Walpole bounds

Hashin and Shtrikman bounds (HS), elaborated in 1962, provide the estimate of bounds for elastic constants in the heterogeneous material [44]. The necessary condition, under these bound were derived, is a random isotropic distribution of phases and the same order of elastic moduli $k$ and $\mu$, i.e. both have to increase or decrease for all phases simultaneously.

HS bounds are very useful for a rapid checking of heterogeneous materials if they satisfy conditions of phase random distribution and moduli order. On the other hand, if the experimental effective properties lie bellow the lower HS bound, a discontinuous behavior is to be expected, in the forms of defects or cracks. Hashin-Shtrikman bounds are much narrower than Voigt-Reuss bounds since additional information about random isotropic distribution is taken into account.

Hashin and Shtrikman [44] found that the lower bound of bulk modulus coincides with the effective bulk modulus of coated sphere assemblage as discussed in section 5.5. When the phases of coated spheres are interchanged, the effective bulk modulus corresponds to the upper Hashin-Shtrikman bound. The reason of bounds coincidence is in spherical symmetry, which substitutes isotropic material, and exhibits the constant strain field within one phase.

HS bounds coincide with the scheme of Mori and Tanaka in the case that composite matrix is made from the softer phase and inclusions are in the form of spheres, or randomly distributed ellipsoids. However, the results are not equal in case of elongated particles with different shapes or orientations.

Consider a two phase medium with bulk moduli $k_1$, $k_2$, shear moduli $\mu_1$, $\mu_2$, and phase fractions $f_1$, $f_2$. Suppose the following inequalities for both phases

$$k_1 \leq k_2, \quad \mu_1 \leq \mu_2. \tag{5.28}$$

The resulting elastic bounds of Hashin-Shtrikman are calculated from a variational formulation

$$k_1 + \frac{f_2}{\frac{1}{k_2-k_1} + \frac{3f_1}{3k_1+4\mu_1}} \leq \quad k_{eff} \quad \leq k_2 + \frac{f_1}{\frac{1}{k_1-k_2} + \frac{3f_2}{3k_2+4\mu_2}}, \tag{5.29}$$

$$\mu_1 + \frac{f_2}{\frac{1}{\mu_2-\mu_1} + \frac{6f_1(k_1+2\mu_1)}{5\mu_1(3k_1+4\mu_1)}} \leq \quad \mu_{eff} \quad \leq \mu_2 + \frac{f_1}{\frac{1}{\mu_1-\mu_2} + \frac{6f_2(k_2+2\mu_2)}{5\mu_2(3k_2+4\mu_2)}}. \tag{5.30}$$

If more phases are present in a composite, the necessary order of bulk and shear moduli are of importance. The phases must have increasing or decreasing bulk and shear moduli together. If not so, Walpole or Hashin-Shtrikman-Walpole broader bounds should be used [18]. The resulting formula for bulk and shear modulus bounds of the latter reads

$$k_{low}^{high} \quad = \quad \left\langle \frac{1}{k_r + \frac{4}{3}\mu_{min}^{max}} \right\rangle^{-1} - \frac{4}{3}\mu_{min}^{max} = \left( \sum_r \frac{f_r}{k_r + \frac{4}{3}\mu_{min}^{max}} \right)^{-1} - \frac{4}{3}\mu_{min}^{max}, \tag{5.31}$$

$$\mu_{low}^{high} \quad = \quad \left\langle \frac{1}{\mu_r + k_{min}^{max}} \right\rangle^{-1} - k_{min}^{max} = \left( \sum_r \frac{f_r}{\mu_r + k_{min}^{max}} \right)^{-1} - k_{min}^{max}, \tag{5.32}$$

where $k_{min}^{max}$ and $\mu_{min}^{max}$ are maximal and minimal absolute values of the bulk and shear moduli in a composite and $f_r$ are the volume fractions of phases. An example of applied bounds is in Fig. 7.4. The bounds are usually wide for porous materials and for practical evaluation are of little importance.

### 5.3 Mori-Tanaka method

The Mori-Tanaka homogenization method [75] assumes a matrix-inclusion morphology of considered phases, as derived in terms of localization in Eq. (5.15) and extended to elliptical pores, e.g. [98].

The Mori Tanaka scheme for estimating the effective moduli is applicable to regions of the graded microstructure that have a well-defined continuous matrix and a discontinuous particulate phase as showed in Fig. 5.1. It takes into account the weak interaction of the elastic fields
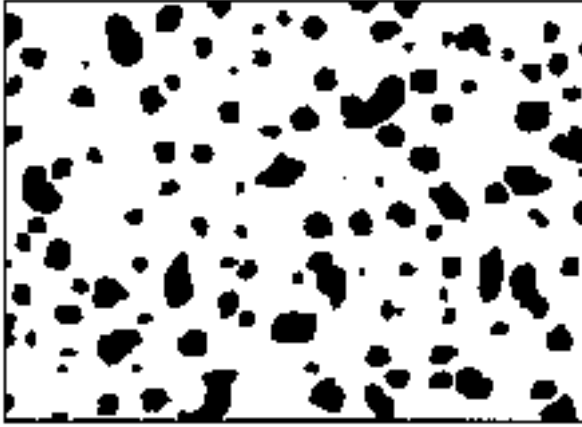
Figure 5.1: Material with particulate structure



Figure 5.2: Material with skeletal structure

between neighboring inclusions. The matrix phase, denoted as the reference phase and by subscript $0$, is reinforced by spherical particles of a particulate phases, denoted by subscript $r$. In this notation, $k_0$, $\mu_0$ are the bulk and shear matrix moduli and $k_r$, $\mu_r$ refer to phases that represent inclusions. The following explicit estimates are derived from Eq. (5.15) when inserting Eq. (5.16) - (5.19). $\alpha_0$ and $\beta_0$ are according to Eqs. (5.17), (5.18). The explicit results for the effective bulk modulus $k$ and the shear modulus $\mu$ then read

$$
k_{hom} = \frac{\sum_r f_r k_r \left(1 + \alpha_0 \left(\frac{k_r}{k_0} - 1\right)\right)^{-1}}{\sum_r f_r \left(1 + \alpha_0 \left(\frac{k_r}{k_0} - 1\right)\right)^{-1}},
\tag{5.33}
$$

$$
\mu_{hom} = \frac{\sum_r f_r \mu_r \left(1 + \beta_0 \left(\frac{\mu_r}{\mu_0} - 1\right)\right)^{-1}}{\sum_r f_r \left(1 + \beta_0 \left(\frac{\mu_r}{\mu_0} - 1\right)\right)^{-1}}.
\tag{5.34}
$$

## 5.4 Self-consistent scheme

The self-consistent scheme (SCS) of Budiansky, elaborated by Hill [51] is an implicit scheme for composites with the skeletal structure in Fig. 5.2, incorporating the Eshelby tensor and based on Eq. (5.15). Reference medium points to the homogenized medium itself hence the solution is in implicit form. The iterative procedure may be rewritten from Eqs. (5.33), (5.34), substituting $k_0$ for $k_{hom}$ and $\mu_0$ for $\mu_{hom}$, respectively. In porous materials, the implicit formulation yields elastic properties of porous phase when the porosity fraction is above approximately 50 %. Good results of the self-consistent scheme were reported on Voronoï cells with Young's moduli ratios of 1:100 and with the amount of up to 50 % of solid phase representation [58].

The threshold of SCS may be used to account for solid percolation threshold in cement pastes [17]. Selection of elastic properties of capillary porosity determines the volume fraction at which SCS yields the threshold. When porosity is considered with the elastic parameters of water, Tab. 4.3, the SCS threshold needs more than 50 % of capillary water-filled porosity. When the water-filled porosity is considered with a very low Poisson's ratio, i.e. corresponding to a true void, the SCS yields the threshold at exactly 50 % of porosity.

To demonstrate the performance of SCS in various *w/c*'s, the homogenization level of cement paste is carried out, Fig. 5.3. The intrinsic mechanical values from Tab. 4.3 are used, with the water-filled porosity. The data of OPC are taken from Slamečka [107] and the relationship between capillary porosity and Young's modulus $E$ from empirical formula according to Eq. (7.1), [57].
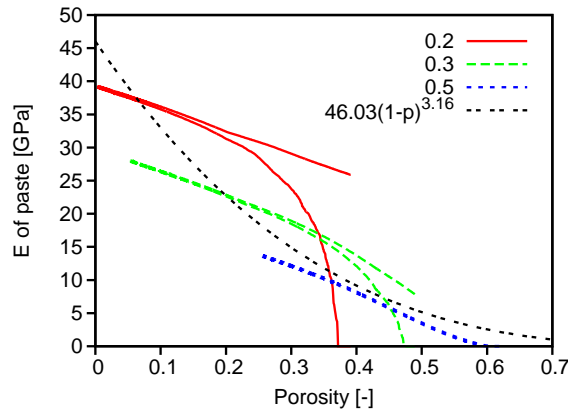


Figure 5.3: Performance of self consistent scheme with and without solid percolation

When a Portland cement paste has $w/c = 0.318$, the set point coincides with 50 % of void porosity which is the threshold of self-consistent scheme [17]. If the *w/c* is lower, the paste exhibits non-negligible Young's modulus right from the beginning of hydration, which is the problem of particle contact and assumption of perfect bonding in homogenization problem.

The solid percolation threshold $p_c$ from where the cement paste should exhibit mechanical response, was determined by CEMHYD3D model as the first non-zero value in any of three principal directions accounted for solid percolation. The results of $p_c$ are similar to Tab. 4.1. Eq. (1.2) was modified to account for percolation in the simplest way. It was assumed that the same amount of phases exist in the percolated path and in the rest of the phases, arriving to a proportional relation with percolated fraction

$$E_{perc} = E_{SCS} \frac{p - p_c}{1 - p_c}, \tag{5.35}$$

where $E_{perc}$ is the corrected $E_{SCS}$ modulus for the percolation of solids. Indeed, the reduced Young modulus is then closer to experimental fit in Fig. 5.3. For high *w/c*, the percolation is much less significant than in the case of low *w/c*, Fig. 5.3. Another way to account for percolation is to filter directly the RVE which will result in modified volume fractions while satisfying the assumption of perfect bonding among phases.

Another example is an uncoupling of length scales via the SCS, Tab. 5.1. Three phases are considered, $A$ as a solid phase and $B$, $C$ as the water-filled porosity. The homogenization order will be altered to show how these levels are associated. Homogenization "all at one" generally gives the lowest values, line 10 in Tab. 5.1, since the nominator in Eqs. (5.33), (5.34) is the lowest due to the fact that $k_B$ and $k_C$ are nearly zero. The line 7 reflects the arrangement, where the phase $A$ has an intrinsic porosity $B$ and this mixture as one phase is inserted in the porous phase $C$. Therefore, the porosity distributed over different length scales does not reduce effective properties so considerably as the porosity at one scale in the same volume.

| Line | Phase | Vol. fraction | $E$ | $\nu$ | $k$ | $\mu$ |
|------|-------|---------------|-----|-------|-----|-------|
| 1 | A | 0.63 | 10 | 0.3 | 8.333 | 3.846 |
| 2 | B | 0.07 | $10^{-6}$ | 0.49 | 0.000 | 0.000 |
| 3 | C | 0.30 | $10^{-6}$ | 0.49 | 0.000 | 0.000 |
| 4 | A+C | 0.677 : 0.323 | 3.531 | 0.247 | 2.329 | 1.416 |
| 5 | B+C | 0.189 : 0.811 | $10^{-6}$ | 0.49 | 0.000 | 0.000 |
| 6 | A+B | 0.9 : 0.1 | 7.995 | 0.287 | 6.244 | 3.107 |
| 7 | (A+B)+C | (0.7) : 0.3 | **3.185** | **0.245** | 2.083 | 1.279 |
| 8 | A+(B+C) | 0.63 : (0.37) | **2.583** | **0.236** | 1.634 | 1.045 |
| 9 | (A+C)+B | (0.93) : 0.07 | **3.036** | **0.243** | 1.969 | 1.221 |
| 10 | A+B+C | 0.63 : 0.07 : 0.3 | **2.583** | **0.236** | 1.634 | 1.045 |

Table 5.1: Homogenization with different phase order on a three phase system

### 5.5 N-layered spheres

Hervé and Zaoui [47] derived elastic strains and stresses of $n$-layered isotropic spherical inclusions embedded in an unbounded matrix. The uniform stress or strain load is applied in infinity. Continuity of displacements and stresses is assumed between adjacent spheres. Similar models of spherical assemblages and isotropic elasticity were derived by Hashin [43] or Christensen and Lo [23] for two material phases in the form of two isotropic spheres. The $n$-layered

model may be extended to arbitrary number of phases embedded in an infinite homogenized medium. The geometrical representation of the Hervé-Zaoui scheme is in Fig. 5.4.
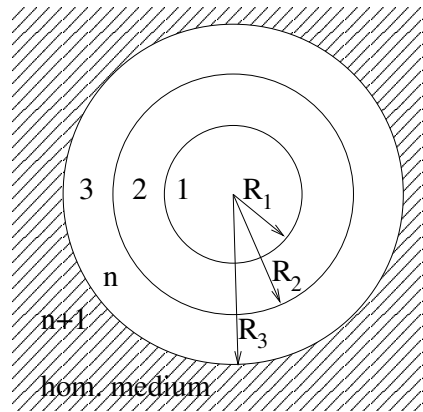


Figure 5.4: The geometrical representation of the 3-layered Hervé-Zaoui scheme

There are two possible applications of the Hervé and Zaoui scheme: the first one taking $n + 1$ phases, i.e. also the elastic properties of the homogenized medium. The resulting displacements and stresses may be calculated. The second application of the scheme is the determination of homogeneous elastic medium around the spherical inclusions, taking only elastic properties of $n$ isotropic phases. The derivation of Hervé and Zaoui scheme is in Appendix A.

It must be emphasized that in the case of two spherical inclusions, i.e. $n = 2$, the scheme provides the same estimates as the Hashin-Shtrikman bounds. If the bulk and shear moduli are in an ascending order from the center, i.e. the core is more compliant than the shell, then the result coincide with the upper Hashin-Shtrikman bound. In the reversed configuration, i.e. the cherry-pit model, the lower Hashin-Shtrikman bound is found [47].

Heutkamp and Ulm [48] used this scheme for the study of ITZ in leached cement pastes. The order of phases according to Fig. 5.4 was the following; $1 =$ sand, $2 =$ ITZ, $3 =$ cement paste, hom. medium $=$ mortar. They found a reduction of Young's modulus of degraded cement paste by 40 or 45 % in ITZ. In their case, the ITZ thickness was assumed as 20 $\mu$m. The Hervé and Zaoui scheme will be validated for the effect of ITZ in section 7.3.

## 5.6 Other elastic homogenization models

Beyond presented homogenization models, other models applied directly to concrete were derived as well [71]. Hirsch combined Voigt and Reuss models, disregarding lateral deforma-

tions, by introducing empirical constant $\chi$ [71]

$$\frac{1}{E_c} = (1 - \chi) \left[ \frac{c}{E_a} + \frac{1-c}{E_p} \right] + \chi \left[ \frac{1}{cE_a + (1-c)E_p} \right], \tag{5.36}$$

$$c = \frac{V_a}{V}, \tag{5.37}$$

where $V_a$, $E_a$ refer to aggregates, and $E_p$ to the cement paste and $E_c$ to concrete. When the empirical constant $\chi = 0$, the serial Reuss model emerges while $\chi = 1$ represents a parallel configuration of the paste and aggregates. Value $\chi = 0.5$ is often recommended for practical applications [71].

Hansen (reference in [71]) simplified the Hashin-Shtrikman bounds [44] coinciding with Hervé-Zaoui scheme [47] for two phases with equal Poisson's ratios of 0.2

$$E_c = \left[ \frac{f_p E_p + (1 + f_a) E_a}{(1 + f_a) E_p + f_p E_a} \right]. \tag{5.38}$$

Counto proposed a model where a prism of aggregate is embedded in a self-similar concrete prism, see [71], resulting in

$$\frac{1}{E_c} = \frac{1 - \sqrt{f_a}}{E_p} + \frac{1}{\left( \frac{1 - \sqrt{f_a}}{\sqrt{f_a}} \right) E_p + E_a}. \tag{5.39}$$

To illustrate the performance of the above-mentioned methods, a system aggregate-soft phase is used. The parameters for aggregate were $E_a = 60$ GPa and $\nu_a = 0.3$ and the soft phase has $E_p = 0.6$ GPa and $\nu_p = 0.3$ which is the property contrast $\frac{100}{1}$. Fig. 5.5 shows the results when varying the soft phase content in a mixture. The Hirsch parameter was considered to be $\chi = 0.5$. The Mori-Tanaka estimate and HS upper bound coincide. Hirsch, Counto, Hansen and the HS lower bound give the very similar results with the maximum difference of 1.4 GPa. The SCS estimate drops to zero shortly after exceeding 50 % of "void". Roberts and Garboczi [98] established a relation for a porous material by means of FEM. They found a good fit for the case of spherical pores with $n = 1.65$, $\phi_0 = 0.818$

$$E_{composite} = E_{solid} \left( 1 - \frac{\phi}{\phi_0} \right)^n. \tag{5.40}$$

Another example considers aggregates with the volume of 0.75, which is typical for concrete, $E_a = 60$ GPa and $\nu_a = 0.3$ combined with a hardening cement paste having $E_p$ varying from 0 to 40 GPa and $\nu_p = 0.3$. Eight homogenization methods in Fig. 5.6 show the results from elastic homogenization. Hirsch (for $\chi = 0.5$), Counto, Hansen and HS lower bound fall to a similar curve.
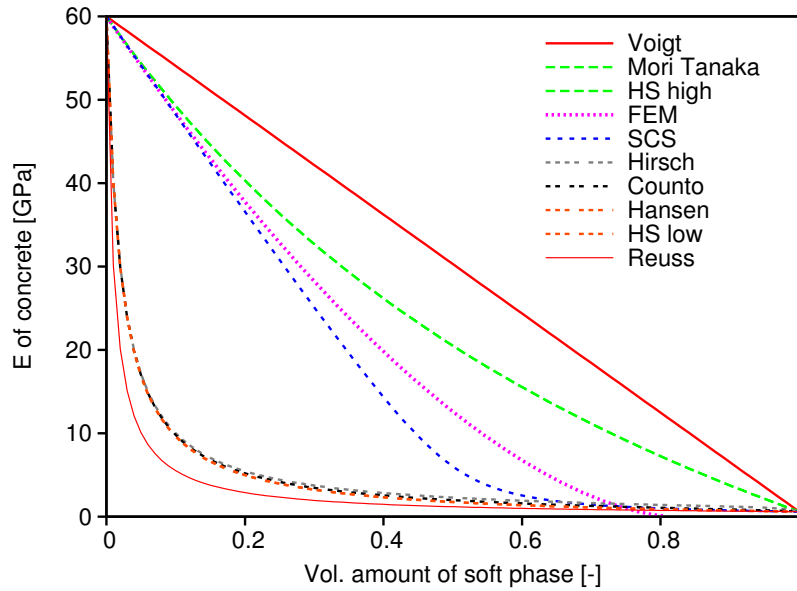
Figure 5.5: Homogenization of an aggregate with a soft phase
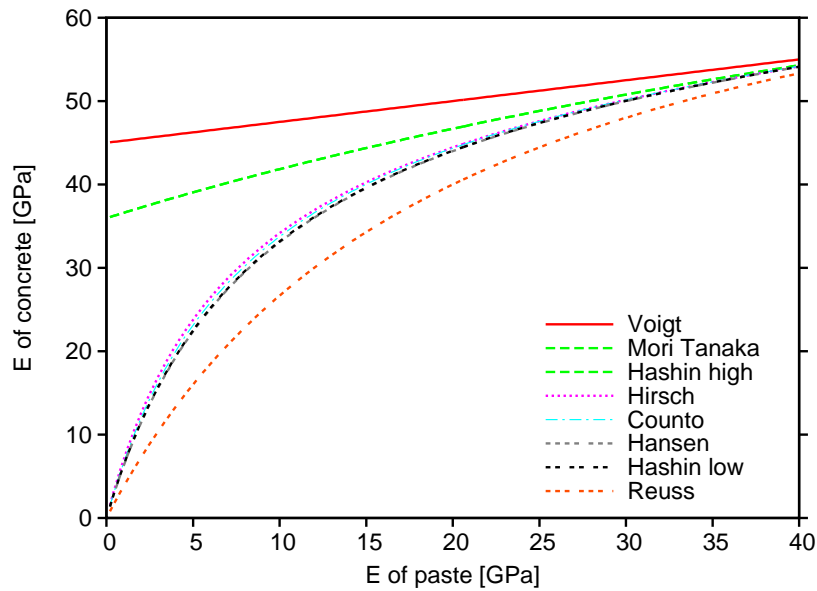


Figure 5.6: Homogenization of an aggregate with hydrating cement paste

Chapter 6

# NUMERICAL HOMOGENIZATION METHODS

## *6.1  General principles and material isotropy*

The aim of numerical homogenization methods is to find again an effective stiffness tensor of the homogenized medium that would behave in the same way as a heterogeneous composite on finite dimensions. The finite dimensions are represented with the RVE which is a sufficiently large material sample to be statistically representative. The boundary conditions must be imposed on the RVE to define uniquely the homogenization problem. The numerical methods are used to find a static equilibrium within the RVE associated with the boundary conditions. Eqs. (5.2), (5.4) formulate stress and strain averages over the RVE and Eqs. (5.13), (5.14) the effective homogenized stiffness and compliance tensors.

The homogenization method will be further restrained to isotropic intrinsic properties and it is natural to expect a homogenized isotropic response due to the definition of the RVE. The 3D constitutive equation in a tensorial form of isotropic homogeneous material may be rewritten in the engineering matrix and vector notation

$$
\left\{
\begin{array}{c}
\sigma_{xx} \\
\sigma_{yy} \\
\sigma_{zz} \\
\tau_{xy} \\
\tau_{yz} \\
\tau_{zx}
\end{array}
\right\}
=
\left[
\begin{array}{cc}
\frac{E}{(1+\nu)(1-2\nu)}
\left[
\begin{array}{ccc}
1-\nu & \nu & \nu \\
\nu & 1-\nu & \nu \\
\nu & \nu & 1-\nu
\end{array}
\right] & 0 \\
0 &
\left[
\begin{array}{ccc}
\mu & 0 & 0 \\
0 & \mu & 0 \\
0 & 0 & \mu
\end{array}
\right]
\end{array}
\right]
\left\{
\begin{array}{c}
\varepsilon_{xx} \\
\varepsilon_{yy} \\
\varepsilon_{zz} \\
\gamma_{xy}(2\varepsilon_{12}) \\
\gamma_{yz}(2\varepsilon_{23}) \\
\gamma_{xz}(2\varepsilon_{13})
\end{array}
\right\}, \quad (6.1)
$$

where the shear modulus $\mu$ is defined in Eq. (5.23) and the Cauchy stress vector $\boldsymbol{\sigma}$ has the components

$$
\boldsymbol{\sigma} = \{\sigma_{11}, \sigma_{22}, \sigma_{33}, \sigma_{12}, \sigma_{23}, \sigma_{13}\}^T, \quad (6.2)
$$

and consequently the small strains vector $\boldsymbol{\varepsilon}$

$$
\boldsymbol{\varepsilon} = \{\varepsilon_{11}, \varepsilon_{22}, \varepsilon_{33}, 2\varepsilon_{12}, 2\varepsilon_{23}, 2\varepsilon_{13}\}^T. \quad (6.3)
$$

Anisotropy may appear in the RVE due to an insufficient size of the RVE, e.g. the percolation at early ages. The principle of energy conservation was used for the transition from a

generally anisotropic to an isotropic homogenized material. Isotropic material is characterized by two independent constants, e.g. Young's modulus and Poisson's ratio. The stiffness matrix of an isotropic material, Eq. (6.1), may be seen as two independent submatrices: the upper submatrix $3 \times 3$ relates the normal stresses and strains, while the lower submatrix $3 \times 3$ relates the shear stresses and strains. From these two submatrices and with the help of stored energy in an anisotropic material, two independent elastic constants of isotropic medium may be calculated in one step. The work in a unity of linear isotropic material reads

$$W = \frac{1}{2}\, \boldsymbol{\varepsilon}^T \boldsymbol{\sigma} = \frac{1}{2}\, \boldsymbol{\varepsilon}^T \boldsymbol{C}^{eff} \boldsymbol{\varepsilon}. \tag{6.4}$$

Eq. (6.4) leads to the following set of equations that finally yields the homogeneous Young's modulus and Poisson's ratio $\nu$, all in engineering terms

$$\mu = \frac{\gamma_{xy}\tau_{xy} + \gamma_{yz}\tau_{yz} + \gamma_{xz}\tau_{xz}}{\gamma_{xy}^2 + \gamma_{yz}^2 + \gamma_{xz}^2}, \tag{6.5}$$

$$a = \varepsilon_{xx}^2 + \varepsilon_{yy}^2 + \varepsilon_{zz}^2, \tag{6.6}$$

$$b = 2(\varepsilon_{xx}\varepsilon_{yy} + \varepsilon_{xx}\varepsilon_{zz} + \varepsilon_{yy}\varepsilon_{zz}), \tag{6.7}$$

$$W_n = \varepsilon_{xx}\sigma_{xx} + \varepsilon_{yy}\sigma_{yy} + \varepsilon_{zz}\sigma_{zz}, \tag{6.8}$$

$$\nu = \frac{W_u - \mu a}{\mu(b - a) + 2W_u}, \tag{6.9}$$

$$E = 2\mu(1 + \nu), \tag{6.10}$$

where $W_n$ stores twice the amount of internal energy.

## 6.2  Eigenstrain method

Eigenstrain is a generic name of a stress-free strain that exists in a material due to former history as welding, phase transformation, initial strains, plastic strains etc. One of good representatives and the most common application of eigenstrains is temperature. Temperature is a special kind of eigenstrain where the shear components equal to zero so only axial effects are involved. The other names for eigenstrain as a stress-free strain or a polarization strain may appear in the literature.

Similarly, an eigenstress is a self-equilibrated internal stress that was caused by eigenstrain in bodies that are not loaded by any external force. The advantage of using eigenstrain is the way of imposing of residual stresses in a linear model of elasticity. This method will be used further as a loading condition that corresponds to a homogeneous strain state.

In the theory of small deformations, the total strain $\varepsilon_{ij}$ is considered as the sum of elastic strain $\varepsilon_{ij}^{elas}$ and eigenstrain $\varepsilon_{ij}^{eigs}$

$$\varepsilon_{ij} = \varepsilon_{ij}^{elas} + \varepsilon_{ij}^{eigs}. \tag{6.11}$$

The total strain, which includes eigenstrain, is compatible with deformation

$$\varepsilon_{ij} = \frac{1}{2}\left(\boldsymbol{u}_{i,j} + \boldsymbol{u}_{j,i}\right). \tag{6.12}$$

The stiffness tensor of material is symmetric thanks to Cauchy's second law of motion, which means that $\boldsymbol{u}_{i,j} = \boldsymbol{u}_{j,i}$. The constitutive equation for linear elastic material is corrected for the effect of eigenstrain, by substituting Eqs. (6.11), (6.12)

$$
\begin{aligned}
\boldsymbol{\sigma}_{ij} &= \mathbf{C}_{ijkl}\varepsilon_{kl} = \mathbf{C}_{ijkl}\left(\varepsilon_{kl} - \varepsilon_{kl}^{eigs}\right), & (6.13)\\
\boldsymbol{\sigma}_{ij} &= \mathbf{C}_{ijkl}\left(\boldsymbol{u}_{k,l} - \varepsilon_{kl}^{eigs}\right). & (6.14)
\end{aligned}
$$

Let us compare two loading conditions: the first case will deal with an arbitrary and equilibrated stress state on the domain. In the second case, only eigenstrain will be assumed while the material domain will be free from any external forces and boundary constraints

$$
\begin{aligned}
\boldsymbol{\sigma}_{ij,j} &= 0, & \forall \boldsymbol{x} \in \Omega, & (6.15)\\
\boldsymbol{\sigma}_{ij}\boldsymbol{n}_j &= 0, & \forall \boldsymbol{x} \in \Gamma, & (6.16)
\end{aligned}
$$

where $\boldsymbol{n}_j$ is the outer vector of the boundary. After substituting Eq. (6.14) into Eq. (6.15) and Eq. (6.16), the following equations relating displacements and eigenstrains are obtained

$$
\begin{aligned}
\mathbf{C}_{ijkl}\boldsymbol{u}_{k,lj} &= \mathbf{C}_{ijkl}\varepsilon_{kl,j}^{eigs}, & \forall \boldsymbol{x} \in \Omega, & (6.17)\\
\mathbf{C}_{ijkl}\boldsymbol{u}_{k,l}\boldsymbol{n}_j &= \mathbf{C}_{ijkl}\varepsilon_{kj}^{eigs}\boldsymbol{n}_j, & \forall \boldsymbol{x} \in \Gamma. & (6.18)
\end{aligned}
$$

Eq. (6.17) proves that the contribution of eigenstrains can be replaced with a body forces while Eq. (6.18) sets up the relationship between surface tractions and eigenstrains. The body forces $-\mathbf{C}_{ijkl}\varepsilon_{kj}^{eigs}$ and the surface tractions $\mathbf{C}_{ijkl}\varepsilon_{kj}^{eigs}\boldsymbol{n}_j$ create the same displacement field across the domain.

In the case that only some part of the domain (such as any kind of inclusion) is loaded by the eigenstrain, the equilibrium conditions on the surface $\Gamma_i$ between inclusion and matrix follows as in Eq. (6.17)

$$
\begin{aligned}
\mathbf{C}_{ijkl}\boldsymbol{u}_{k,lj} + \mathbf{C}_{ijkl}\varepsilon_{kl,j}^{eigs}\chi(\boldsymbol{x}) &= \mathbf{0}, & (6.19)\\
\chi(\boldsymbol{x}) &= 1 \ \forall \boldsymbol{x} \in \Gamma_i, \text{ otherwise } 0, & (6.20)\\
\varepsilon_{kl,j}^{eigs} &= \varepsilon_{kl}^{eigs}\boldsymbol{n}_j. & (6.21)
\end{aligned}
$$

The solution of Eq. (6.19) for the given eigenstrain $\varepsilon_{kl}^{eigs}$ is obtainable through the methods of periodicity, such as Fourier series or Green's function.

When imposing eigenstrains to the domain, the strains are introduced to all material phases regardless of their intrinsic mechanical properties and the homogenized stiffness tensor does

not depend on imposed eigenstrain. Since the relation between strains, or eigenstrains, and displacement exists, the body is then subjected to homogeneous displacement conditions over the domain. For example, the periodic material yields the macroscopic stiffness tensor

$$\mathbf{C}^{hom} : \boldsymbol{E} = \boldsymbol{\Sigma} = \langle \mathbf{C}(\boldsymbol{x}) : (\boldsymbol{\varepsilon}(\boldsymbol{u}^*) + \boldsymbol{E}) \rangle, \tag{6.22}$$

where $\boldsymbol{u}^*$ is a fluctuation part of the periodic displacement field. Input eigenstrains $\boldsymbol{E}$ may be chosen arbitrarily resulting to the same $\mathbf{C}^{hom}$.

The above-mentioned strain approach may be substituted with a stress approach, prescribing overall homogeneous stress for the domain. This topic is discussed in detail, e.g. [72, 134].

### 6.3 Smaller volume then the representative volume element

In every practical simulation, the RVE is smaller then the studied material sample. Huet [52] coined the term *apparent properties* which results from an insufficient size of RVE. Two limiting types of boundary conditions may be imposed on the RVE. The static uniform boundary conditions (SUBC) are defined in such a way, that the tractions are prescribed on the boundary $\Gamma$

$$\boldsymbol{\sigma}\boldsymbol{n} = \boldsymbol{\Sigma}\boldsymbol{n}, \quad \forall \boldsymbol{x} \in \Gamma. \tag{6.23}$$

On the other hand, kinematic uniform boundary conditions (KUBC) follow the prescribed displacements on the boundary from the given strain $\boldsymbol{E}$

$$\boldsymbol{u} = \boldsymbol{E}\boldsymbol{x}, \quad \forall \boldsymbol{x} \in \Gamma. \tag{6.24}$$

The response of loading conditions according to Eqs. (6.23), (6.24) yields the same result only when the size of RVE is large enough (compare with Eqs. (5.13), (5.14)). In such a particular case, the material macroscopic response is independent of the applied boundary conditions. The special case of boundary conditions is the periodic one, which is always a combination of the KUBC and SUBC. Huet [52] proved that SUBC and KUBC are the bounds of effective properties on insufficiently sized RVE, following the inequalities of apparent and effective stiffness tensors

$$\mathbf{C}^{app}_{SUBC} \leq \mathbf{C}^{app}_{PERIODIC} \leq \mathbf{C}^{app}_{KUBC}, \tag{6.25}$$

$$\mathbf{C}^{app}_{SUBC} \leq \mathbf{C}^{eff} \leq \mathbf{C}^{app}_{KUBC}, \tag{6.26}$$

where $\mathbf{C}^{app}$ is the apparent stiffness fourth-order tensor. The inequality can be understood in the sense of quadratic form, i.e., $\boldsymbol{\varepsilon} : \mathbf{C} : \boldsymbol{\varepsilon}$ for any tensor $\boldsymbol{\varepsilon} \neq \boldsymbol{0}$. The same inequality works for bulk and shear moduli but not for Young's modulus or Poisson's ratio. For the effect of boundary condition type in real cement pastes, see Fig. 7.7.

### 6.4 FEM eigenstrain procedure for periodic boundary conditions

According to Eq. (6.22), the strain can be decomposed to the constant and fluctuating part for the case of periodic boundary conditions

$$\varepsilon(\boldsymbol{x}) = \boldsymbol{E} + \varepsilon^*(\boldsymbol{x}), \tag{6.27}$$

where the fluctuating strain $\varepsilon^*(\boldsymbol{x})$ is searched with the FEM and equals to zero on average over the body. The principle of virtual work yields in fact the Hill lemma, Eq. (5.5)

$$\langle \delta\varepsilon^*(\boldsymbol{x}) : \boldsymbol{\sigma}(\boldsymbol{x}) \rangle = \langle \delta\varepsilon^*(\boldsymbol{x}) \rangle : \langle \boldsymbol{\sigma}(\boldsymbol{x}) \rangle = 0. \tag{6.28}$$

The discretization via the Galerkin method leads to the formulation of FEM, subsituting for the fluctuating displacement field $\boldsymbol{u}^*(\boldsymbol{x}) = \boldsymbol{N}(\boldsymbol{x})\boldsymbol{r}$, where $\boldsymbol{N}(\boldsymbol{x})$ is the matrix of interpolation functions and $\boldsymbol{r}$ is the nodal displacement vector. Regardless of boundary conditions, the assembly of finite elements provides the linear algebraic equations

$$\boldsymbol{K}\boldsymbol{r} = \boldsymbol{F}, \tag{6.29}$$

where $\boldsymbol{K}$ is a reduced global stiffness matrix including the effect of supports and $\boldsymbol{F}$ is a vector of nodal forces. Plugging the variation of Eq. (6.27) into Eq. (6.28) yields a loading case with the eigenstrains so that Eq. (6.29) becomes

$$\boldsymbol{K}\boldsymbol{r} = -\sum_{elements} \int_V \boldsymbol{B}^T \boldsymbol{D}\boldsymbol{E} \mathrm{d}V, \tag{6.30}$$

where $\boldsymbol{B}$ is the strain interpolation matrix, $\boldsymbol{D}$ represents a rigidity matrix and the matrix $\boldsymbol{E}$ contains prescribed components of the eigenstrain.

Approximate solution using the conjugate gradient method (CGM) [105] is typically used for the solution of Eqs. (6.29), (6.30) due to the fact that the solution time is significantly smaller than that of exact solution in a majority of cases. The CGM will always converge to exact solution in a case of positive definite matrices, which is the case of linear elasticity. Storage of $\boldsymbol{K}$ is advantageous in the form of symmetric compressed rows [105] found as the most effective memory usage.

Garboczi [36] used the FEM method directly for the computation of elastic properties of cement paste on RVE's obtained from CEMHYD3D model. A similar approach will be used here, extended for solid percolation. The finite element is chosen to be representative of the voxel, which results in the hexahedral element. The limited computer memory calls for a minimal set of algebraic equations, which are also determined by the displacement approximations over the element. The tri-linear interpolation functions are used in our case so each of eight vertices in
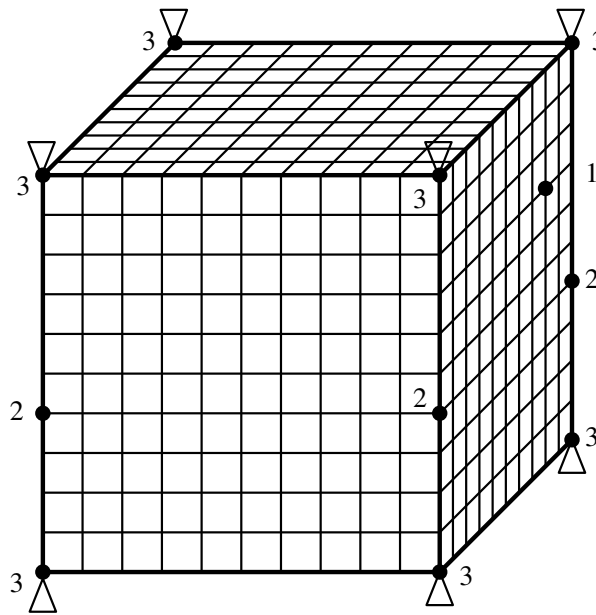
Figure 6.1: FEM implementation of voxelized microstructure with periodic boundary conditions

the hexahedral (brick) element has three DOF's. The microstructure yields a structured regular mesh that may be easily generated without the need of external mesh generator, Fig. 6.1.

Suppose that the heterogeneous domain with the periodic boundary conditions is subjected to an uniform eigenstrain. The force contributions from the adjacent finite elements are introduced to the nodes. In the case of linear elasticity, solving the linear equations provides the unknown nodal displacements. Since the stresses are in principle discontinuous due to heterogeneous materials, volume averaging of strains and stresses is performed via integration points on elements according to Eq. (5.5). When a homogeneous strain is applied to the heterogeneous RVE, the average strain equals back to the input strain.

Periodic boundary conditions on RVE may be effectively implemented by a code number technique [59]. The advantage of this method is no increase of degrees of freedom or additional parameters like in the case of penalty method, e.g. [134]. On the other hand, the bandwidth of stiffness matrix increases which slows down the consecutive elimination.

Fig. 6.1 shows a typical situation for the RVE with the periodic boundary conditions. Each node on the RVE side experiences the same periodic displacement as the opposite node (number 1) so they are denoted as virtual pairs. Particular node on the edge of the RVE has three virtual twins (number 2) and each vertex node has seven virtual twins (number 3). These relations are simply expressed in terms of identical nodal code numbers. Support of microstructure is chosen as fixed displacements in one vertex (number 3) so all eight vertices are fixed.

### *6.4.1 Numerical verification*

The first set of verifications is carried out on a simple microstructure consisting of two phases. A checkerboard symmetrical configuration allows to use directly the hexahedral elements, Fig. 6.2. The periodic boundary conditions with eigenstrain load are assumed. When the RVE size is $2 \times 2 \times 2$ then there is no nodal displacement at vertices at all. This allows checking directly the performance of element due to imposed eigenstrain. The regular mesh refinement improves the results, which converge to the correct solution. The results for hexahedral element with tri-linear shape function are summarized in Tab. 6.1. Eq. (6.30) was solved with the LDL decomposition [105]. The phase mechanical parameters are chosen in such a way that the shear moduli are equal [36]. In such a particular case, equal shear moduli must be obtained, regardless of morphology in 2D or 3D, leading to the homogenized bulk moduli in 2D or 3D

$$
k_{2D} = \frac{\mu(c_1 k_1 + c_2 k_2) + k_1 k_2}{\mu + c_1 k_2 + c_2 k_1}, \tag{6.31}
$$

$$
k_{3D} = \frac{\frac{4}{3}\mu(c_1 k_1 + c_2 k_2) + k_1 k_2}{\frac{4}{3}\mu + c_1 k_2 + c_2 k_1}, \tag{6.32}
$$

where $\mu$ is the equal shear modulus, $k_1$, $k_2$ are bulk moduli of two phases, $k_{2D}$, $k_{3D}$ are the resulting bulk moduli and $c_1$, $c_2$ are volumetric fractions. Fig. 6.2 displays the mesh and nodal displacement on three mesh refinements. Note that the edges on the periodic unit cell remain straight since coupling of opposite twin nodes creates the periodic RVE.

| - | Phase 1 | Phase 2 | 8 elmts | 64 elmts | 1000 elmts | Exact |
|---|---|---|---|---|---|---|
| E | 2.25 | 2.95082 | 2.907 | 2.826 | 2.732 | **2.688** |
| $\nu$ | 0.125 | 0.47541 | 0.454 | 0.413 | 0.366 | **0.344** |
| $k_{3D}$ | 1.0 | 20 | 10.50 | 5.438 | 3.399 | 2.873 |
| $\mu$ | 1.0 | 1.0 | 1.0 | 1.0 | 1.0 | 1.0 |
| $c_1$ | - | - | 0.5 | 0.5 | 0.5 | 0.5 |
| $c_2$ | - | - | 0.5 | 0.5 | 0.5 | 0.5 |
| DOF's | - | - | 21 | 189 | 2997 | - |
| Time [s] | - | - | 0.23 | 1.11 | 51.00 | - |

Table 6.1: FEM results from checkerboard configuration on hexahedral elements with **linear** approximations and consumed CPU time (400 MHz, LDL solver)

In order to get better results, quadratic approximation functions are used for the approximation of displacements. Hence, quadratic hexahedral element with 20 nodes and 60 DOF's is

a) $2 \times 2 \times 2$        b) $4 \times 4 \times 4$        c) $10 \times 10 \times 10$
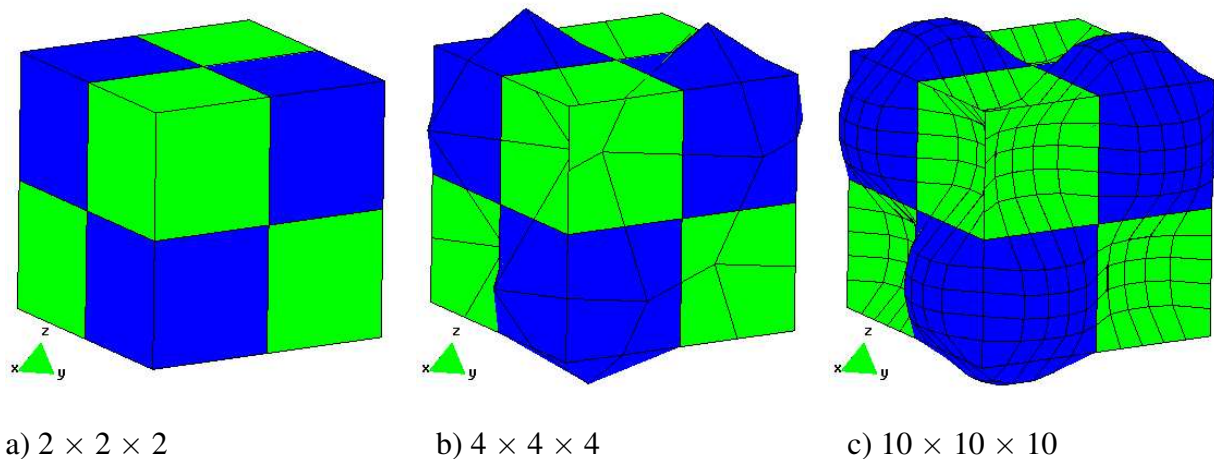
Figure 6.2: Displacements on checkerboard structure using **linear** hexahedral element

used in the 3D analysis. The same microstructure with identical input values was checked for performance, Fig. 6.3 and Tab. 6.2.

| - | Phase 1 | Phase 2 | 8 elmts | 64 elmts | 216 elmts | 1000 elmts | Exact |
|---|---------|---------|---------|----------|-----------|------------|-------|
| E | 2.25 | 2.95082 | 2.908 | 2.745 | 2.722 | 2.703 | **2.688** |
| $\nu$ | 0.125 | 0.47541 | 0.454 | 0.373 | 0.361 | 0.351 | **0.344** |
| $k_{3D}$ | 1.0 | 20 | 10.50 | 3.596 | 3.266 | 3.032 | 2.873 |
| $\mu$ | 1.0 | 1.0 | 1.0 | 1.0 | 1.0 | 1.0 | 1.0 |
| $c_1$ | - | - | 0.5 | 0.5 | 0.5 | 0.5 | 0.5 |
| $c_2$ | - | - | 0.5 | 0.5 | 0.5 | 0.5 | 0.5 |
| DOF's | - | - | 93 | 765 | 2589 | 11997 | - |
| Time [s] | - | - | 3.4 | 18.50 | 105 | 32 min. | - |

Table 6.2: FEM results from checkerboard configuration on hexahedral elements with **quadratic** approximations and consumed CPU time (400 MHz, LDL solver)

The second set of examples will deal with unpercolated cement paste microstructures and will briefly discuss the results. The microstructure of original $25 \times 25 \times 25$ $\mu$m size for the Kamali *et al.* 's experiments is used [57], see section 7.1.2 and 7.1.3, and increased two and three times which corresponds to a finer resolution. Two microstructures are used: the dense one with $w/c = 0.25$ and the looser one with $w/c = 0.5$. The evolution of modulus of elasticity is depicted in Figs. 6.4, 6.5. Capillary porosity is considered as a water-filled one.

Generally, FEM overestimates modulus of elasticity due to coarse approximations of displacements. The FEM results, in terms of Young's modulus, are very close to the linear re-

a) $2 \times 2 \times 2$            b) $4 \times 4 \times 4$            c) $10 \times 10 \times 10$
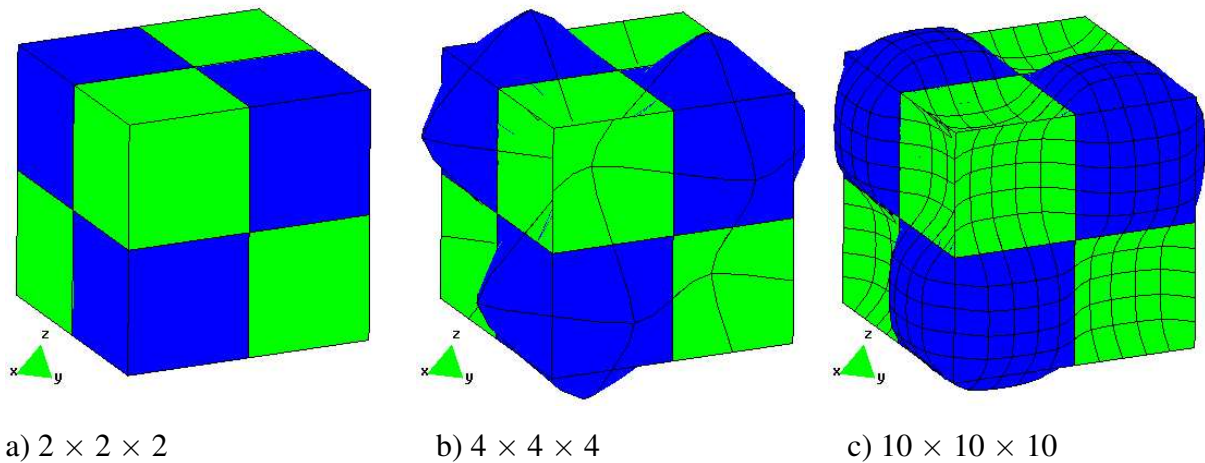
Figure 6.3: Displacements on checkerboard structure using **quadratic** hexahedral element
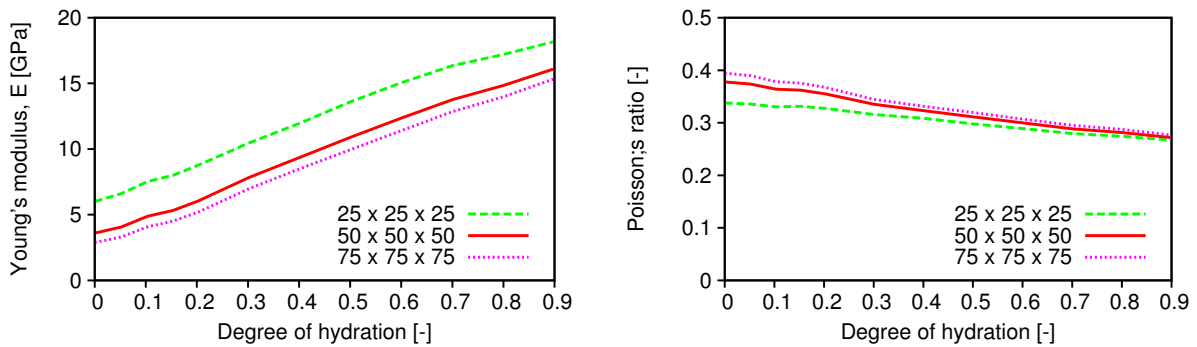


Figure 6.4: FEM evolution of E, $\nu$ at **w/c = 0.5**, unpercolated input images
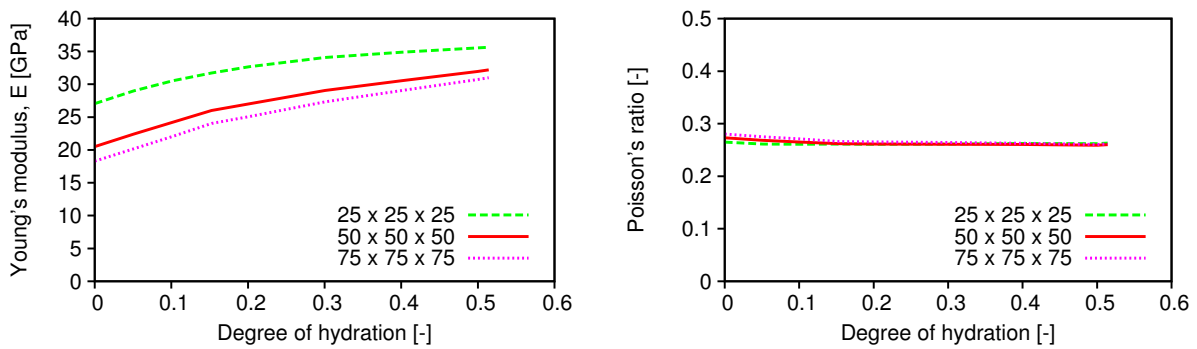


Figure 6.5: FEM evolution of E, $\nu$ at **w/c = 0.25**, unpercolated input images

lationship with the degree of hydration. Poisson's number is not strongly dependent on the resolution. In both cases, the Young modulus does not start from zero and Poisson's number does not start from 0.5. Since unpercolated microstructures are used, the dense microstructure contains many contact points of cement grains that cause non-zero origin of the Young modulus. No convergence problems were observed on unpercolated images.

### *6.4.2 Implementing phase disconnectedness*

Figs. 6.4, 6.5 of hydrating cement paste testify that at the beginning of hydration, unpercolated microstructures are much stiffer than in reality. The same conclusion is valid for analytical results, Fig. 5.3. The reason is hidden in a phase connectedness that must be accounted for as already demonstrated macroscopically by Eq. (5.35).

The implemented algorithm of solid percolation routine in CEMHYD3D is called the burning algorithm [37]. This algorithm separates connected and unconnected phases where the percolated way is determined from solid connected voxels with shared adjacent sides. In original version, only clinker phases, ettringite and C-S-H were involved in the percolation assessment. This assumption was extended to all solids, including CH, hydrogarnet etc.

The adjacent finite elements share the same displacement at nodes. This leads necessarily to stiffer structure due to rough displacement approximations at sharp edges when elements do not share the same face. The next disagreement is visible at the beginning of hydration, Fig. 6.5. When the dense microstructure is analyzed, cement particles touch each other due to insufficient resolution and meshing. This problem is solved with a particle labeling with its own ID. Therefore, the information which particles are connected and which not is available even if the resolution does not capture these details.

An arbitrary vertex, where the eight adjacent vertices meet, will be called the central node. Unconnected node of adjacent finite element to the central node means that there is no physical connection. Two adjacent voxels are considered to be connected at the central node when

- they are connected directly face-to-face or,
- they are not connected directly face-to-face but are connected at least by one adjacent voxel in any configuration, i.e. they share the same edge connected through another adjacent voxel or they share a vertex and remain connected through three adjacent voxels.

There are three possible configurations of disconnected adjacent elements, Fig. 6.6. Disconnection by a side ( Fig. 6.6-a) needs additional 4 nodes, by an edge 2 nodes ( Fig. 6.6-b), and by a vertex 1 node ( Fig. 6.6-c). If any additional node is present at the central node location, such node is called a *split node*. Note that each node has three degrees of freedom.

Fig. 6.7 shows a typical 2D slice of periodic RVE. The split nodes are marked at all locations that create sharp corners and would cause the stress concentration problems due to coarse mesh. The split node approach is similar to contact element approach, presented by Torrenti and Benboudjema [118]. In the proposed split-node algorithm, a minimal increase of additional nodes is maintained and consequently the size of Eq. (6.29). When the split nodes are introduced, the displacement, stress, or strain fields are discontinuous, violating the assumption of
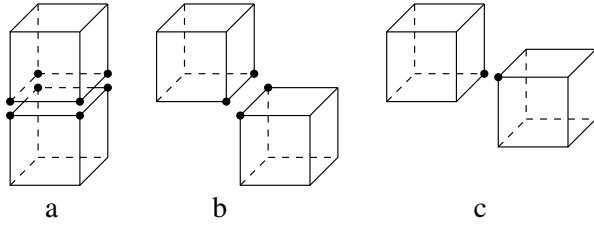
Figure 6.6: Possible configuration of split nodes in adjacent voxels
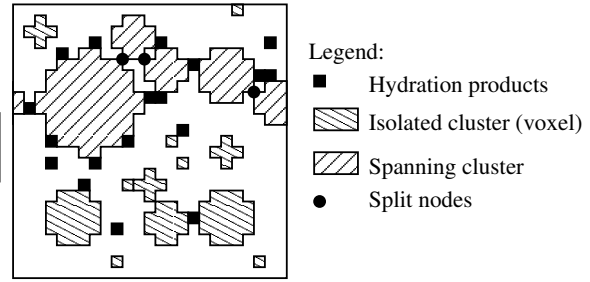


Figure 6.7: Example of percolation in 2D microstructure at early ages

perfect bonding.

### 6.5  Static and kinematic uniform boundary conditions

The static (SUBC) and kinematic uniform boundary conditions (KUBC) are introduced according to Eqs. (6.23), (6.24). There is no requirement of RVE periodicity but the RVE remains periodic as an output of CEMHYD3D. The kinematic uniform boundary conditions are quick for iteration since displacements are prescribed on the boundary nodes. On the other hand, RVE with the static uniform boundary conditions was found as the worst situation for the CGM solver. If not enough iterations, highly non-isotropic response is obtained. For an illustration, normalized residuum for Eq. (6.29) is defined as

$$\text{normalized residuum} = \frac{(\boldsymbol{K}\widetilde{\boldsymbol{r}_i} - \boldsymbol{F})^T(\boldsymbol{K}\widetilde{\boldsymbol{r}_i} - \boldsymbol{F})}{\boldsymbol{F}^T\boldsymbol{F}}, \tag{6.33}$$

where $\widetilde{\boldsymbol{r}_i}$ is the $i^{th}$ approximation of the solution. When the equilibrium is reached, the nominator is zero.

Fluctuation of normalized residuum is often observed during homogenization since the stiffness matrix is not well preconditioned. The potential energy in FEM is minimized in each CGM step

$$\Pi = \frac{1}{2}\widetilde{\boldsymbol{r}_i}^T\boldsymbol{K}\widetilde{\boldsymbol{r}_i} - \widetilde{\boldsymbol{r}_i}^T\boldsymbol{F}. \tag{6.34}$$

During the SUBC run, the normalized residuum of $10^{-6}$ is of sufficient accuracy. Fig. 6.8 displays the normalized residuum of a typical run performed on $w/c = 0.25$ with already percolated microstructure at the degree of hydration 0.018, DOF $= 3573$. Numbers in Fig. 6.8 are homogenized Young's moduli, the correct value is 0.105 GPa as was found after many iterations, when the normalized residuum dropped bellow $10^{-6}$. The LDL decomposition (28.6 s) is slower than 5000 iterations by CGM (22.4 s) at 400 MHz CPU on $10 \times 10 \times 10$ finite elements. The difference of computational time is much higher in larger RVE.
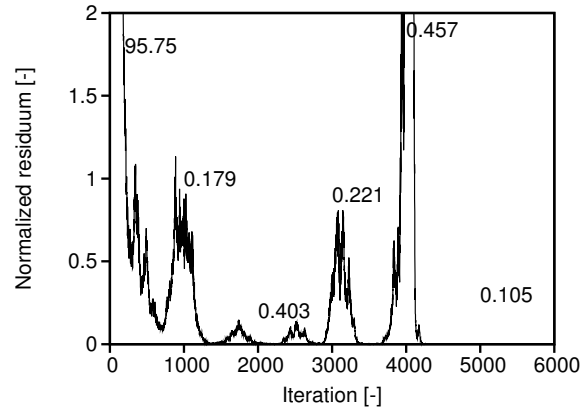
Figure 6.8: Normalized norm of residuum in the CGM, SUBC, $10 \times 10 \times 10$ voxels, percolated RVE on $w/c = 0.25$. The values above are homogenized Young's moduli at corresponding peaks

## 6.6  FFT-based homogenization

The next successive homogenization method is based on the fast Fourier transformation (FFT), as introduced by Moulinec and Suquet for mechanical problems [76]. Any periodic function such as displacement field may be approximated by a series of complex exponential functions; in the FFT form corresponding to a search for the complex coefficients $\xi$. Mathematical properties of FFT are summarized in, e.g. [126, 134]. Following the idea of Hashin-Shtrikman [44], arbitrary stress field in a composite may be decomposed into the contribution of reference homogeneous material and to the polarization stress. Similarly, the strain field may be decomposed into a homogeneous and the fluctuating part

$$\boldsymbol{\sigma}(\boldsymbol{x}) = \mathbf{C}(\boldsymbol{x})\boldsymbol{\varepsilon}(\boldsymbol{x}) = \mathbf{C}^0\boldsymbol{\varepsilon}(\boldsymbol{x}) + \boldsymbol{\tau}(\boldsymbol{x}), \tag{6.35}$$

$$\boldsymbol{u}(\boldsymbol{x}) = \boldsymbol{E}\boldsymbol{x} + \boldsymbol{u}^*(\boldsymbol{x}), \tag{6.36}$$

$$\boldsymbol{\varepsilon}(\boldsymbol{x}) = \boldsymbol{E} + \boldsymbol{\varepsilon}(\boldsymbol{u}^*(\boldsymbol{x})), \tag{6.37}$$

where $\mathbf{C}(\boldsymbol{x})$ and $\mathbf{C}^0$ are the stiffness tensors of the homogenized and of any homogeneous reference medium. The polarization stress $\boldsymbol{\tau}(\boldsymbol{x})$ equals on volume average to zero when the reference medium is chosen in such a way that it corresponds to the homogenized one

$$\int_V \boldsymbol{\tau}(\boldsymbol{x})\mathrm{d}\boldsymbol{x} = \mathbf{0}. \tag{6.38}$$

The fluctuating strain part may be expressed with the help of stress polarization tensor $\boldsymbol{\tau}(\boldsymbol{x})$ and Green's operator $\boldsymbol{\Gamma}^0$ associated with the elasticity tensor $\mathbf{C}^0$ by means of convolution

$$\boldsymbol{\varepsilon}(\boldsymbol{u}^*(\boldsymbol{x})) = -\boldsymbol{\Gamma}^0 * \boldsymbol{\tau}(\boldsymbol{x}). \tag{6.39}$$

Inserting Eq. (6.39) into Eq. (6.37) yields

$$\boldsymbol{\varepsilon}(\boldsymbol{x}) \;=\; \boldsymbol{E} - \int_V \boldsymbol{\Gamma}^0(\boldsymbol{x} - \boldsymbol{x}')\boldsymbol{\tau}(\boldsymbol{x}')\mathrm{d}\boldsymbol{x}', \tag{6.40}$$

where Green's operator $\boldsymbol{\Gamma}^0$ may be obtained as a fundamental solution of Lamé's system of elastic equations. The bulk and shear modulus together with the coefficients of Fourier transformation are involved. For derivation and explicit formulae see, e.g. [72, 126].

Plugging Eq. (6.35) into Eq. (6.40) yields the periodic Lippmann-Schwinger integral equation

$$\boldsymbol{\varepsilon}(\boldsymbol{x}) + \int_V \boldsymbol{\Gamma}^0(\boldsymbol{x} - \boldsymbol{x}')(\mathbf{C}(\boldsymbol{x}') - \mathbf{C}^0)\boldsymbol{\varepsilon}(\boldsymbol{x}')\mathrm{d}\boldsymbol{x}' = \boldsymbol{E}, \tag{6.41}$$

which may be rewritten as an iterative procedure

$$\boldsymbol{\varepsilon}^{k+1}(\boldsymbol{x}) = \boldsymbol{E} - \int_V \boldsymbol{\Gamma}^0(\boldsymbol{x} - \boldsymbol{x}')(\mathbf{C}(\boldsymbol{x}') - \mathbf{C}^0)\boldsymbol{\varepsilon}^k(\boldsymbol{x}')\mathrm{d}\boldsymbol{x}'. \tag{6.42}$$

The integral term containing convolution may be efficiently treated with the help of FFT. The term $\mathbf{C}(\boldsymbol{x}') - \mathbf{C}^0$ in Eq. (6.42) may be simplified to $-\mathbf{C}^0$ due to the requirements of periodicity and reference medium. The term $\mathbf{C}^0\boldsymbol{\varepsilon}^k(\boldsymbol{x}')$ represents the stress, resulting into

$$\boldsymbol{\varepsilon}^{k+1}(\boldsymbol{x}) = \boldsymbol{\varepsilon}^k(\boldsymbol{x}) - \int_V \boldsymbol{\Gamma}^0(\boldsymbol{x} - \boldsymbol{x}')\boldsymbol{\sigma}^k(\boldsymbol{x}')\mathrm{d}\boldsymbol{x}'. \tag{6.43}$$

The solution is straightforward and the iterations are stopped when the stress equilibrium is maintained with a given precision

$$\mathrm{error}^k = \frac{\sqrt{\langle||\mathrm{div}(\boldsymbol{\sigma}^k)||^2\rangle}}{||\langle\boldsymbol{\sigma}^k\rangle||} < \mathrm{error}_{\mathrm{required}}. \tag{6.44}$$

The selection of the reference medium affects the convergence rate. It is possible to transform the stiffness tensor $\mathbf{C}^0$ into a degenerate identity tensor $\mathbf{I}$ without any numerical or iteration difficulties. It is best to choose the transformed reference stiffness tensor of the homogenized medium such that [126]

$$\mathbf{C}^0_{optim} = \frac{\alpha + \beta}{2}\mathbf{I}, \tag{6.45}$$

where $\alpha$ and $\beta$ are the maximal and minimal eigenvalues of the stiffness tensors of the phases.

When all phases from Tab. 4.3 are present in a hydrating cement paste, the optimum reference medium is $\mathbf{C}^0 = 168\,\mathbf{I}$ GPa. The regular periodic cement paste microstructure allows an analysis on a single 32-bit PC in the size of $230 \times 230 \times 230$ points with the memory consumption of 3.1 GB. On a 64-bit PC with 5.9 GB of memory, the RVE of $300 \times 300 \times 300$ voxels may be easily analyzed.

The test of convergence was carried out on the OPC with the $w/c = 0.25$. Two percolated images $50 \times 50 \times 50$ with the resolution of 1 $\mu$m from the NIST model entered the FFT homogenization with the water-filled porosity of $k = 2.2$ GPa. The maximum number of FFT iterations was set to 2000 and 1000 cycles, at the degrees of hydration of cement paste of 0.13 and 0.45, respectively, Fig. 6.9. For the relative error of 1 % in the Young's modulus, the sufficient number of iterations is 1200 for the lower and 150 for the higher degree of hydration. The reference medium was set in both cases according to Eq. (6.45).
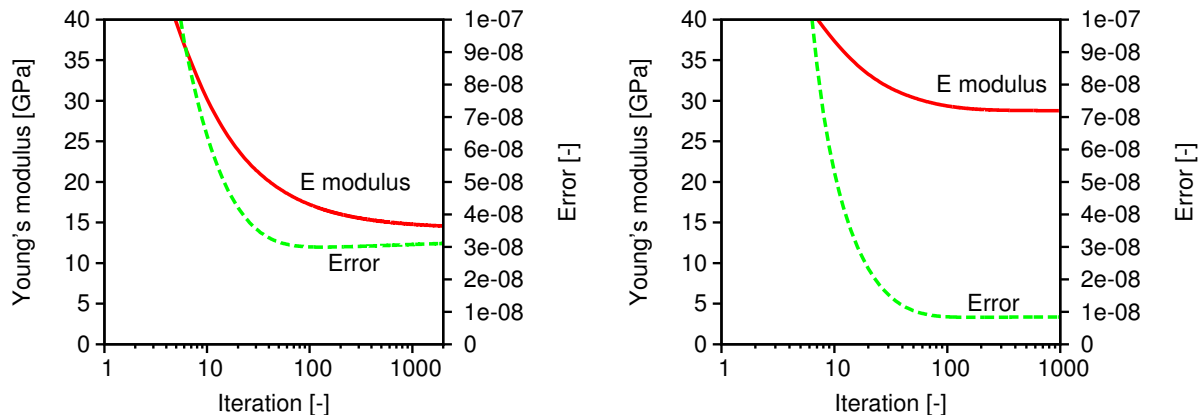
Figure 6.9: Homogenized isotropic Young's modulus and error during FFT homogenization. OPC, $w/c = 0.25$, degree of hydration 0.13 (left) and 0.45 (right)

The effect of refinement of digital microstructures should have only a minor effect on computed homogenized values since the fluctuation of polarization stress remains the same with increased discretization. The performance of FFT homogenization is showed in Fig. 7.16 and indeed, only a minor difference is obvious among the same refined RVE's.

The percolation is not accounted directly in the FFT based homogenization method. However, it is possible to use percolated cement images as the input file. It would be also possible to adjust Green's operator in Eq. (6.42) which relates the polarization stress with the fluctuating strain at two points on the homogeneous reference material but this approach is not used.

Chapter 7

# VALIDATION

This chapter presents the results from various homogenization methods for hydrating cement paste. A short discussion follows each application to give a closer insight. Dehomogenization at the C-S-H level was presented in the section 4.3.1.

## *7.1 Cement paste level*

### *7.1.1 Homogenization of RVE with random distribution of solids*

The simplest microstructure for homogenization is a two-phase system. In the case of cement paste, the hydration products are formed close to the cement grains but their distribution remain often unknown and is left to assumptions. One of such examples is the HYMOSTRUC model [21], where all hydration products evolve concentrically around the cement grains. The question remains, how to check the validity of these assumptions. One of the methods, which is very straightforward, is the elastic homogenization. The placement of hydration products in the pore space has obviously impact on effective elastic properties of the cement paste.

The first attempt to show, how the hydration products affect overall behavior, is based on a probabilistic placement of voxels in the RVE. The placement can be either totally random or influenced by some driving force or mechanism, e.g. ion concentration. Nevertheless, the placement of solid voxels is then distributed unequally. One of the approaches to show such effect is to define some density function, which has the value of 1 in the middle of the RVE and decreases in the directions when approaching the sides of the RVE. The higher the gradient of this distribution function, the more concentrical placement around the center of the RVE is expected. The conditions of periodicity will be satisfied in this case.

The computation is carried out on the RVE $50 \times 50 \times 50$ voxels, where the total porosity is defined as the volume fraction of pores. Homogenization runs with the help of FFT, and at least 500 iterations were performed for each RVE. The error according to Eq. (6.44) was in all cases lower than $10^{-7}$ and generally the convergence was faster at lower porosity values. Both phases have the following parameters; water-filled porosity with the elastic properties of water as $E = 0.001$ GPa, $\nu = 0.499924$, the solid phase similar to the intrinsic properties of hydrates as $E = 30.0$ GPa, $\nu = 0.3$. Either the uniform distribution function of the solid phase or the
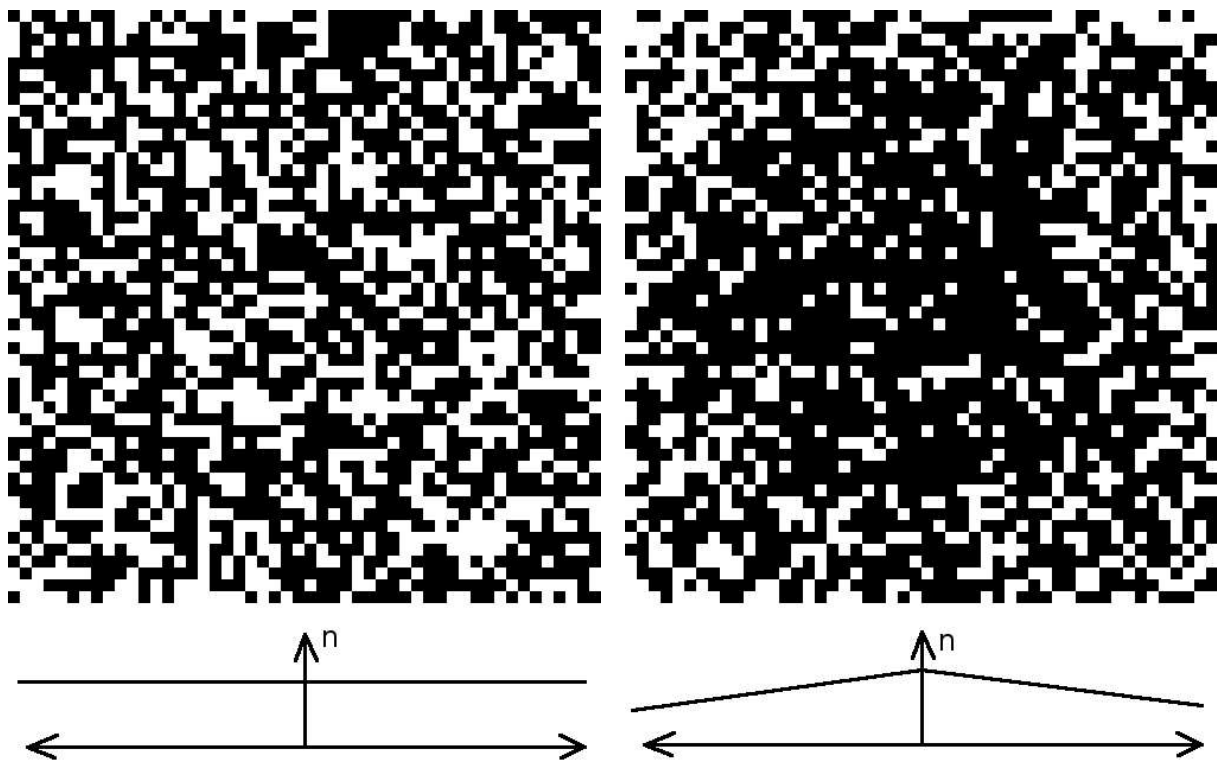
Figure 7.1: Middle slice of analyzed two-phase digital images $50 \times 50 \times 50$ voxels with uniform and linear distribution function at the porosity of 0.4

linear alternative were used to generate random solid phases within RVE. The linear function corresponds to the zero probability of hydrates placement at the most distant corners of the RVE, Fig. 7.1.

The results from homogenization are summarized in Tab. 7.1. At the beginning, the microstructure contains only porosity hence the result corresponds to the parameters of the water-filled porosity. Up to the porosity of about 0.7, the results are nearly the same. When the porosity fraction decreases, the RVE with randomly distributed voxels yields a higher stiffness since solid phases become connected. The difference is obvious from the solid percolation fractions of connected solid voxels. The microstructure with linear distribution functions percolates sooner since more voxels are concentrated around the principal RVE axes. The highest relative difference between the uniform and the linear distribution of hydrates is 43 % in terms of Young's modulus at the porosity of 0.5. The Young's modulus is the most sensitive indicator of microstructure stiffness in this particular case.

The grain of radius 10 $\mu$m was placed in the middle of the $50 \times 50 \times 50$ voxel microstructure. The elastic properties of a digital grain were that of $C_3S$: $E = 135.0$ GPa and $\nu = 0.3$. The grain occupies 0.03335 by volume. Again, two sets of RVE's were generated, with the

| Poros. | Percolation | | E [GPa] | | $\nu$ [-] | | $\mu$ [GPa] | | k [GPa] | |
| --- | --- | --- | --- | --- | --- | --- | --- | --- | --- | --- |
| - | uni | lin | uni | lin | uni | lin | uni | lin | uni | lin |
| 1.0 | 0.000 | 0.000 | 0.001 | 0.001 | 0.5 | 0.5 | 0.000 | 0.000 | 2.193 | 2.193 |
| 0.9 | 0.000 | 0.000 | 0.002 | 0.002 | 0.5 | 0.5 | 0.000 | 0.001 | 2.413 | 2.413 |
| 0.8 | 0.000 | 0.000 | 0.021 | 0.027 | 0.499 | 0.498 | 0.007 | 0.009 | 2.684 | 2.691 |
| 0.7 | 0.000 | 0.160 | 0.200 | 0.202 | 0.489 | 0.489 | 0.067 | 0.068 | 3.053 | 3.110 |
| 0.6 | 0.357 | 0.332 | 1.127 | 0.936 | 0.450 | 0.460 | 0.389 | 0.321 | 3.723 | 3.881 |
| 0.5 | 0.488 | 0.468 | 4.062 | 2.850 | 0.371 | 0.410 | 1.481 | 1.011 | 5.258 | 5.250 |
| 0.4 | 0.597 | 0.587 | 8.777 | 7.507 | 0.316 | 0.337 | 3.334 | 2.807 | 7.969 | 7.695 |
| 0.3 | 0.699 | 0.695 | 13.699 | 12.405 | 0.298 | 0.309 | 5.275 | 4.740 | 11.319 | 10.800 |
| 0.2 | 0.800 | 0.798 | 18.939 | 17.741 | 0.294 | 0.299 | 7.319 | 6.829 | 15.312 | 14.711 |
| 0.1 | 0.900 | 0.900 | 24.394 | 23.734 | 0.295 | 0.297 | 9.416 | 9.149 | 19.862 | 19.502 |
| 0.0 | 1.000 | 1.000 | 30. | 30. | 0.3 | 0.3 | 11.538 | 11.538 | 25. | 25. |

Table 7.1: Effective properties of uniform and linear decreasing distribution function in a two-phase material, $50 \times 50 \times 50$ $\mu$m, the results rounded to three digits

| (Poros.) · | Percolation | | E [GPa] | | $\nu$ [-] | | $\mu$ [GPa] | | k [GPa] | |
| --- | --- | --- | --- | --- | --- | --- | --- | --- | --- | --- |
| · (1-0.033) | uni | lin | uni | lin | uni | lin | uni | lin | uni | lin |
| 1.0 | 0.000 | 0.000 | 0.002 | 0.002 | 0.5 | 0.5 | 0.000 | 0.000 | 2.268 | 2.268 |
| 0.9 | 0.000 | 0.000 | 0.021 | 0.023 | 0.499 | 0.499 | 0.007 | 0.007 | 2.498 | 2.500 |
| 0.8 | 0.000 | 0.000 | 0.126 | 0.130 | 0.492 | 0.492 | 0.042 | 0.043 | 2.790 | 2.810 |
| 0.7 | 0.000 | 0.186 | 0.547 | 0.498 | 0.471 | 0.474 | 0.185 | 0.169 | 3.222 | 3.304 |
| 0.6 | 0.382 | 0.348 | 1.817 | 1.527 | 0.425 | 0.439 | 0.638 | 0.531 | 4.021 | 4.188 |
| 0.5 | 0.506 | 0.484 | 4.574 | 3.743 | 0.362 | 0.391 | 1.677 | 1.346 | 5.561 | 5.705 |
| 0.4 | 0.611 | 0.602 | 8.934 | 8.252 | 0.318 | 0.333 | 3.387 | 3.095 | 8.212 | 8.238 |
| 0.3 | 0.709 | 0.705 | 14.542 | 13.182 | 0.296 | 0.309 | 5.610 | 5.036 | 11.879 | 11.499 |
| 0.2 | 0.807 | 0.805 | 19.990 | 18.705 | 0.292 | 0.299 | 7.734 | 7.198 | 16.046 | 15.535 |
| 0.1 | 0.903 | 0.903 | 25.584 | 24.771 | 0.294 | 0.297 | 9.883 | 9.548 | 20.739 | 20.347 |
| 0.0 | 1.000 | 1.000 | 31.304 | 31.304 | 0.3 | 0.299 | 12.050 | 12.050 | 25.954 | 25.954 |

Table 7.2: Effective properties of uniform and linear decreasing distribution function in a three-phase material with grain fraction volume of 0.033352 (corresponds to 10 $\mu$m radius), the precision rounded to three digits. Size $50 \times 50 \times 50$ $\mu$m, porosity represents a fraction of pore space

uniform and the linearly decreasing distribution function, Tab. 7.2. The trend is similar as in the previous study, i.e. lower effective values of linearly spaced "hydration products".

Last study is performed with the particle radius of 20 $\mu$m, Tab. 7.3. The grain volume fraction is in this case 0.267. When compared with the case of smaller cement grain, the microstructure is generally stiffer. 500 iterations in the FFT-based method is not enough at the

| (Poros.) · | Percolation | | E [GPa] | | $\nu$ [-] | | $\mu$ [GPa] | | k [GPa] | |
|:---:|:---:|:---:|:---:|:---:|:---:|:---:|:---:|:---:|:---:|:---:|
| ·(1-0.267) | uni | lin | uni | lin | uni | lin | uni | lin | uni | lin |
| 1.0 | 0.000 | 0.000 | 0.006 | 0.006 | 0.500 | 0.500 | 0.002 | 0.002 | 2.985 | 2.985 |
| 0.9 | 0.000 | 0.000 | 0.058 | 0.063 | 0.497 | 0.497 | 0.019 | 0.021 | 3.302 | 3.317 |
| 0.8 | 0.000 | 0.000 | 0.290 | 0.308 | 0.487 | 0.486 | 0.098 | 0.104 | 3.737 | 3.791 |
| 0.7 | 0.339 | 0.387 | 1.124 | 1.164 | 0.457 | 0.458 | 0.385 | 0.399 | 4.446 | 4.651 |
| 0.6 | 0.531 | 0.513 | 3.326 | 3.241 | 0.404 | 0.414 | 1.185 | 1.146 | 5.751 | 6.259 |
| 0.5 | 0.625 | 0.613 | 7.599 | 6.870 | 0.347 | 0.371 | 2.821 | 2.506 | 8.278 | 8.871 |
| 0.4 | 0.705 | 0.699 | 13.732 | 12.214 | 0.310 | 0.335 | 5.241 | 4.575 | 12.054 | 12.320 |
| 0.3 | 0.780 | 0.777 | 20.888 | 18.606 | 0.297 | 0.315 | 8.052 | 7.077 | 17.154 | 16.717 |
| 0.2 | 0.853 | 0.852 | 27.910 | 25.979 | 0.293 | 0.304 | 10.791 | 9.960 | 22.485 | 22.112 |
| 0.1 | 0.927 | 0.926 | 34.800 | 33.637 | 0.294 | 0.300 | 13.443 | 12.937 | 28.191 | 28.034 |
| 0.0 | 1.000 | 1.000 | 41.487 | 41.486 | 0.298 | 0.298 | 15.976 | 15.976 | 34.284 | 34.284 |

Table 7.3: Effective properties of uniform and linear decreasing distribution function in a three-phase material with grain fraction volume of 0.267 (corresponds to 20 $\mu$m radius), 50 × 50 × 50 $\mu$m, the results rounded to three digits

beginning since the cement grain is isolated by water-filled porosity from the boundaries which causes a strain concentration problem.

The presented three-phase system (cement grain, hydration products, porosity) show the evolution of elastic properties and solid percolation threshold. Unhydrated cement brings considerable stiffness to the microstructure and acts as the filler.

### 7.1.2  Paste of Kamali et al., w/c = 0.5

This example covers an ordinary CEM I with $w/c = 0.5$. Input data of cement and correlation files according to NIST database are summarized in Tab. 7.4. PSD is recalculated according to Eq. (3.33).

| Component | $C_3S$ | $C_2S$ | $C_3A$ | $C_4AF$ | Gypsum |
|:---|:---:|:---:|:---:|:---:|:---:|
| Vol. content | 0.6994 | 0.1863 | 0.02073 | 0.0804 | 0.013 |
| Blaine fineness | 360 m$^2$/kg | | | | |
| Autocorrelation NIST files [83] | cm115x2f | | | | |

Table 7.4: Cement parameters for Kamali's microstructure reconstruction

In order to explore the effect of the microstructure size, three microstructures with the edge of 25, 50, 75 $\mu$m were generated using the same PSD curve with an appropriate truncation of large particles. The voxel edge size and the resolution is 1 $\mu$m and each RVE contained the

possibly largest cement grain, i.e. the diameter of the half RVE edge. The CEMHYD3D model ran 1500 cycles at a constant temperature of 20°C for each microstructure with the dissolution box of $3 \times 3 \times 3$ $\mu$m under saturated conditions. Fig. 7.2 displays the percolation of solids for one principal direction at early ages, determined as the connected solid volume to the total volume of solid phases. It is obvious that larger cement grains span the pore space better than smaller grains. Therefore, the larger microstructure percolates sooner but when the hydration degree exceeds 0.15, the percolations fall nearly on the same curve. Fig. 7.3 shows the Young modulus as predicted from the two-level analytical homogenization (Mori-Tanaka with SCS), where the phase fractions were taken from the microstructure $75 \times 75 \times 75$ $\mu$m. Since experimental elastic data are not directly available in the literature, the Young modulus is recalculated as a function of capillary porosity from the experiment to a fitted curve of the same author [57]

$$E = 46.03(1 - p_{cap})^{3.16}, \tag{7.1}$$

where $p_{cap}$ is the capillary porosity fraction of CEMHYD3D model.

The high final capillary porosity of this paste, 23 % at the $\alpha = 0.87$, makes the prediction less accurate and modulus underestimation is typical for the self-consistent scheme at the cement paste level.
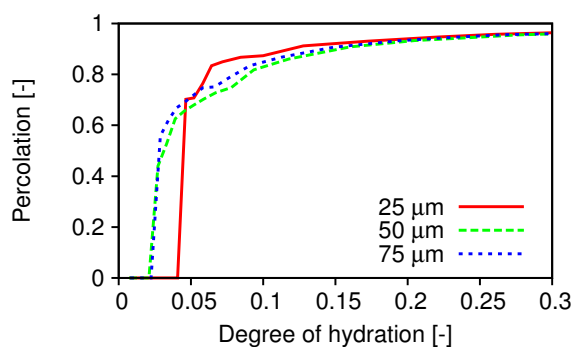


Figure 7.2: Effect of microstructure size on percolation
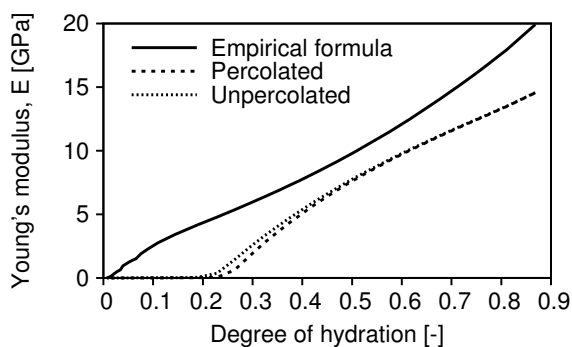
Figure 7.3: Young's modulus, analytical homogenization, un/percolated microstructure

The analytical bounds for this cement paste were studied as well. The cement paste level was considered with already homogenized C-S-H level. Fig. 7.4 displays the results of upper bounds. The lower bounds of Hashin-Shtrikman-Walpole or the Reuss bound yield values close to zero and are not displayed. The Voigt bound, corresponding to the parallel configuration of phases, is higher than other methods.

Fig. 7.5 demonstrates an effect of percolation on Young's modulus as calculated via the FEM with periodic boundary conditions in the RVE $25 \times 25 \times 25$ $\mu$m. Unpercolated regular
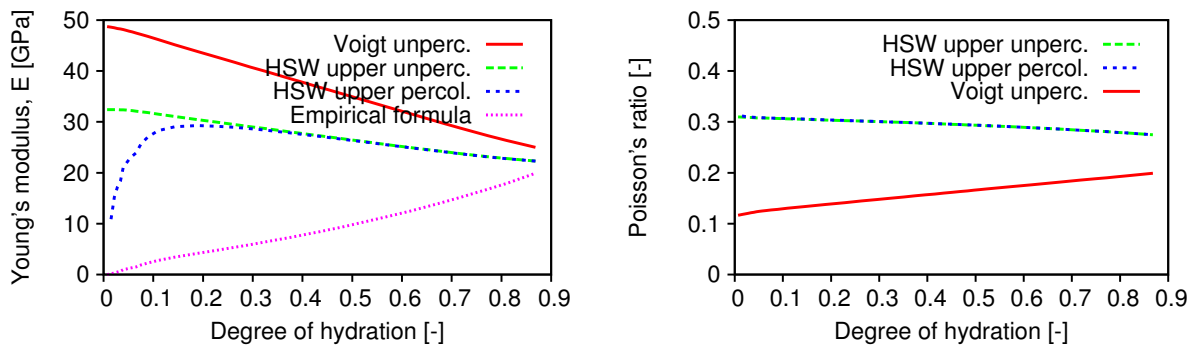
Figure 7.4: Hashin-Shtrikman-Walpole upper bounds and Voigt bound for un/percolated cement paste

microstructure yields non-zero apparent moduli from the sole beginning, i.e. when considering all phases. Overestimation of Young's modulus is the result of high stiffness of the microstructure. The results are improved, when only the spanning clusters with split nodes are taken into account.

Three sizes of microstructures were reconstructed with the maximum cement grain diameter as the half of the microstructure size and hydrated using the dissolution box of $3 \times 3 \times 3\ \mu$m. The effect of RVE size with split nodes is in Fig. 7.6. While the size of $25 \times 25 \times 25\ \mu$m is insufficiently small and leads to a lower stiffness due to the percolation, the difference between 50 and 75 $\mu$m size is negligible and the results correspond well to empirical formula during the whole hydration time. The FFT method on the $75 \times 75 \times 75\ \mu$m microstructure predicts slightly lower values than the FEM. The precision of FFT homogenization method had to fit within 2 % of correct value of elastic modulus, as obtained by many FFT iterations.
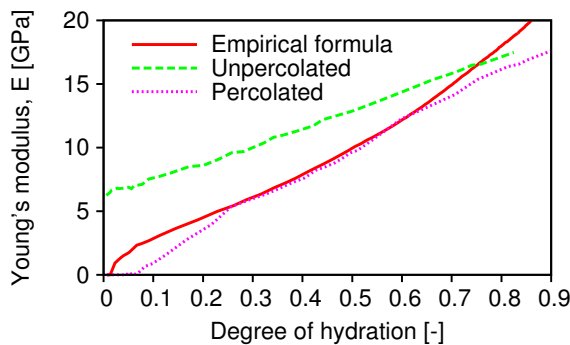


Figure 7.5: Effect of percolation on $E$ modulus, $25 \times 25 \times 25\ \mu$m, FEM - periodic
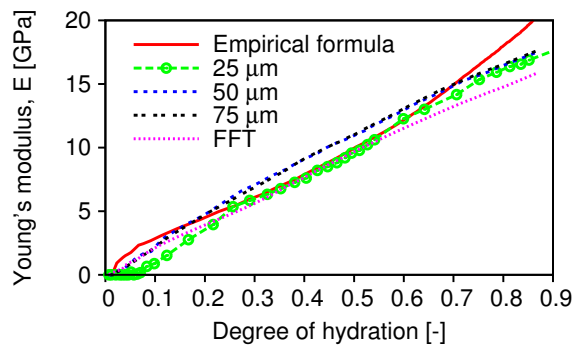
Figure 7.6: Effect of RVE size on $E$ modulus, FEM - periodic, split nodes, FFT

The effect of RVE size on the apparent elastic properties was explored on the microstructures with the edge of 10, 25, 50, 75 and 100 $\mu$m. Since the placement of digital spheres in initial

RVE is *per se* random, five microstructures from each size, with different spatial configurations were evaluated. The same dissolution box $3 \times 3 \times 3$ $\mu$m was used during all simulations.

Fig. 7.7 shows $E$ moduli from FEM with three types of boundary conditions at the degree of hydration of 0.3 and 0.9. The bars represent the 95 % confidence level from five random realizations of each size. Both figures follow bounds from Ineq. (6.25) although $E$ modulus is not linearly dependent on $k$ and $\mu$ moduli hence Ineq. (6.25) is satisfied only approximately. Periodic boundary conditions exhibit the lowest dependence on the RVE size and the size of 50 $\mu$m seems to be representative enough. However, going to earlier stages of hydration, the statistical homogeneity and isotropy fall away and the larger RVE would be probably necessary. Results from uniform, split node mesh and the FFT method are displayed in Fig. 7.8. The Figs. 7.7, 7.8 imply

- the lower the degree of hydration, the larger the size of RVE is necessary,
- the split node algorithm is un-exchangeable for lower degree of hydration in the FEM,
- the scatter decreases with larger RVE and more hydrated microstructure,
- the scatter is not generally the smallest under periodic boundary conditions.
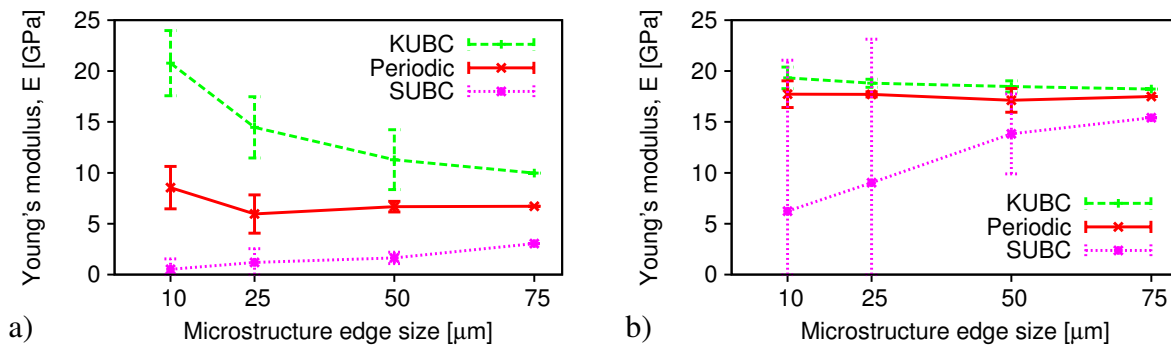


Figure 7.7: Effect of boundary conditions, $\alpha = 0.3$ (a) and 0.9 (b), FEM, split nodes

Tab. 7.5 shows computational requirements on a uniform mesh in the dependence on the microstructure size for the hydration degree of 0.9. 32-bit CPU with the frequency of 3.2 GHz and 3.2 GB memory was used. The precision is set as 1 % in the relative error. The periodic boundary conditions and the FFT method show remarkable difference, especially for larger microstructures. While the Gaussian elimination is proportional approximately to $\mathcal{O}(N^3)$, the conjugate gradient method approaches $\mathcal{O}(N^{1.5})$ and the FFT-based homogenization to $\mathcal{O}(N \log N)$, which is of tremendous difference at larger RVE's. The results from Tab. 7.5 roughly correspond to these estimates, including in addition other computational routines.
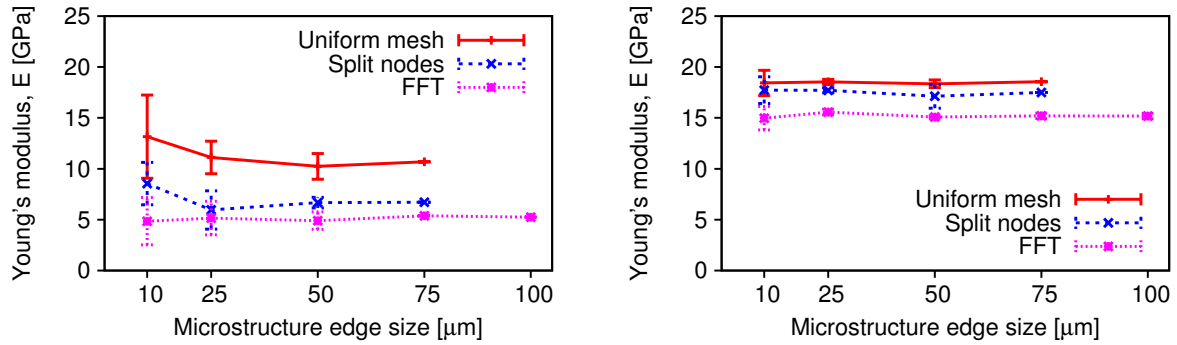
Figure 7.8: Difference among uniform, split node mesh and FFT, $\alpha = 0.3$ (left) and 0.9 (right), FEM - periodic

| Size [$\mu$m ] | DOF's | Memory [MB] | | Time [s] | |
|---|---|---|---|---|---|
| | | FEM | FFT | FEM | FFT |
| $10 \times 10 \times 10$ | 2 997 | 5.7 | 3.1 | 1.6 | 2.6 |
| $25 \times 25 \times 25$ | 46 872 | 71.2 | 6.9 | 24.3 | 6.3 |
| $50 \times 50 \times 50$ | 374 997 | 503 | 35.5 | 218 | 62 |
| $75 \times 75 \times 75$ | 1 265 622 | 1713 | 109 | 787 | 93 |
| $100 \times 100 \times 100$ | - | - | 256 | - | 183 |

Table 7.5: Approximate computational requirements on CPU 3.2 GHz, FEM - periodic, FFT

### 7.1.3  *Paste of Kamali et al., w/c = 0.25*

The dense microstructure of $w/c = 0.25$ was generated in the RVE size of $75 \times 75 \times 75$ $\mu$m and hydrated with 1 $\mu$m voxel resolution, in the $3 \times 3 \times 3$ $\mu$m dissolution box [57]. Tab. 7.4 again summarizes all input data for the same cement.

Fig. 7.9 shows the results for the C-S-H level as obtained via analytical Mori-Tanaka homogenization. The majority of C-S-H$_{LD}$ is later changed to the C-S-H$_{HD}$ type which causes an increase of $E$ modulus at this level. Self-consistent homogenization at the cement paste level is in Fig. 7.10. The experimental data come from the same source as the previous paste with $w/c = 0.5$ [57], originating in recalculation of Young's modulus from the fitted relationship with the capillary porosity according to Eq. (7.1). The percolation threshold plays significant role and, in this particular case, corresponds to the degree of hydration as low as 0.015. Low *w/c* means that high portion of cement remains unhydrated during all hardening process, which means that the maximum degree of hydration attains approximately 0.62. The unhydrated clinker minerals boost the stiffness of the cement paste together with the higher

portion of C-S-H$_{HD}$.
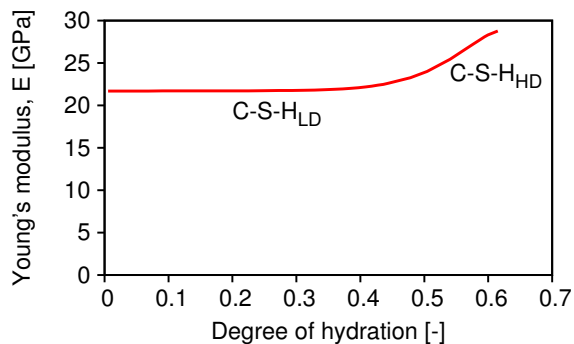


Figure 7.9: Analytical results from the C-S-H level
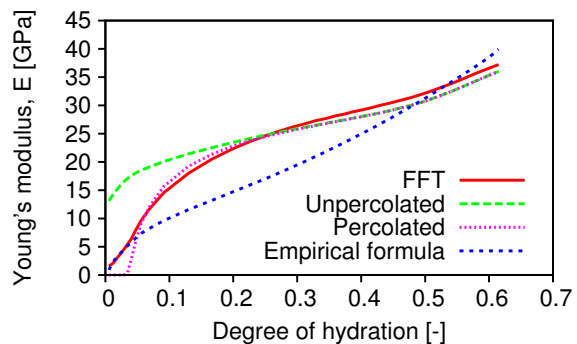


Figure 7.10: Analytically predicted Young's modulus of cement paste, compared to FFT

The percolation of solids in different RVE sizes is depicted in Fig. 7.11. The difference is not significant and all solid phases are connected around the degree of hydration of 0.3. Fig. 7.12 shows the evolution of Young's modulus for the RVE sizes of 25, 50 and 75 $\mu$m under periodic boundary conditions. Since there would be a big discrepancy between an empirical formula, Eq. (7.1), and the results, comparison with analytical homogenization is preferred. The FFT homogenization on the $75 \times 75 \times 75$ $\mu$m microstructure predicts lower $E$ modulus in the middle region. It must be emphasized that the FFT runs on uniform mesh of the percolated microstructure while the FEM mesh contains in addition split nodes. Early and late values correspond well to the empirical formula and to the results from analytical homogenization. The difference between $50 \times 50 \times 50$ and $75 \times 75 \times 75$ $\mu$m RVE's is again not significant for the whole hydration period. If unpercolated microstructures were used, the initial $E$ modulus of the $75 \times 75 \times 75$ $\mu$m would start at 26.2 GPa.
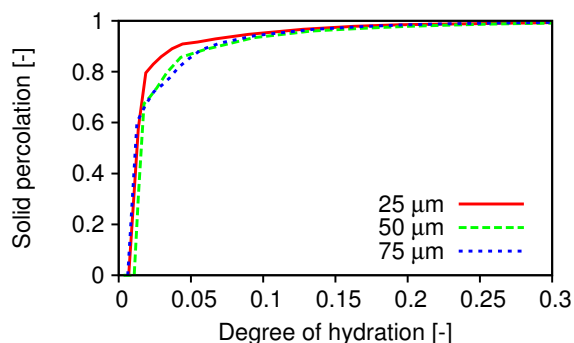


Figure 7.11: Solid percolation of microstructures of different sizes
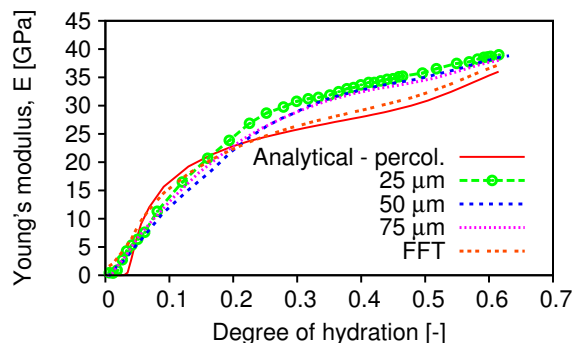


Figure 7.12: Effect of RVE size on $E$ modulus, FEM - periodic, split nodes, FFT

The apparent moduli of different RVE sizes were explored again on microstructures with the

edge sizes of 10, 25, 50 and 75 $\mu$m. Five randomly generated and hydrated samples were used for each RVE size and the hydration parameters had the same values as in the same previous case. Fig. 7.13 shows the effect of boundary conditions on apparent elastic properties for the hydration degree of 0.3 and 0.62, respectively. The widest 95 % confidence level was found for the static uniform boundary condition, the other configurations are comparable for the scatter. The lower hydration degree corresponding to the higher porosity needs larger RVE, as evident from the bias.
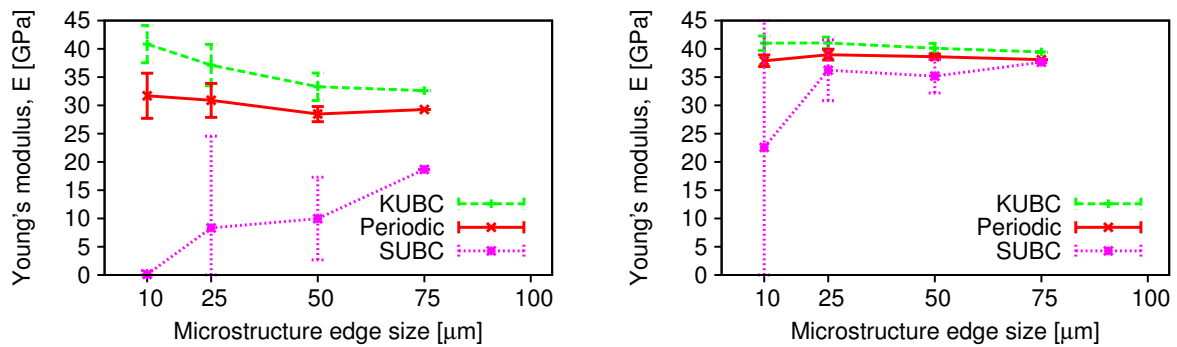


Figure 7.13: Effect of boundary conditions, $\alpha = 0.3$ (left) and 0.62 (right), FEM, split nodes

Fig. 7.14 shows the difference among uniform mesh, split nodes and FFT method for two hydration degrees. All tree configurations with periodic boundary conditions are close in a well-hydrated microstructure while lower hydration degree separates the results from both meshes. The convergence of apparent moduli was tested on the $100 \times 100 \times 100$ $\mu$m microstructures by means of the FFT homogenization. No decrease of average Young's modulus was found against the smaller size of 75 $\mu$m, and 0.6 % difference was against the size of 50 $\mu$m. This suggests that the RVE of 50 $\mu$m is sufficient, at least for later hydration stages.
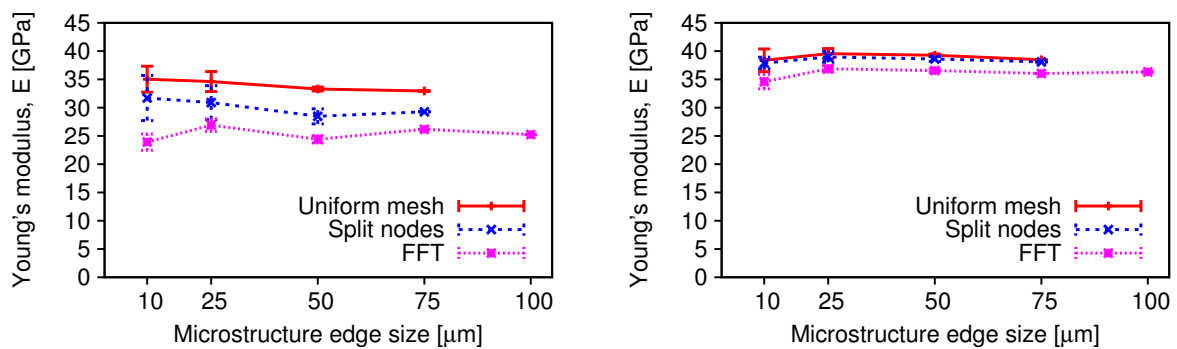


Figure 7.14: Difference among uniform, split node mesh and FFT, $\alpha = 0.3$ (left) and 0.62 (right), FEM - periodic

### 7.1.4  Paste of Boumiz, w/c = 0.40

Boumiz *et al.* [20] measured acoustic wave velocities and the heat of hydration on white cement paste of $w/c = 0.4$ and 0.35. The chemical and physical properties, as recalculated from a mineral composition according to Bogue, are summarized in Tab. 7.6. The gypsum content is estimated as 5 % of volume.

| Component | $C_3S$ | $C_2S$ | $C_3A$ | $C_4AF$ | Gypsum |
|---|---|---|---|---|---|
| Vol. content | 0.7353 | 0.1321 | 0.1239 | 0.0087 | 0.05 |
| Blaine fineness | 370 m²/kg | | | | |
| Autocorrelation NIST files [83] | danwhite | | | | |

Table 7.6: Cement parameters for Boumiz's microstructure reconstruction

The volumetric content of phases during hydration is depicted in Fig. 7.15. The voids represent an empty porosity caused by chemical shrinkage. The C-S-H$_{HD}$ evolves at later stages of hydration due to the confinement as predicted with CEMHYD3D hydration model. To test the resolution of FFT-based homogenization method, the generated set of unpercolated microstructures of $25 \times 25 \times 25$ $\mu$m was rescaled 2, 4 and 8 times. If the homogenization is exact, the results will be the same. Although the FFT-based method can handle an arbitrary continuous field, the discontinuities in stress field cause dominantly the differences, Fig. 7.16. The homogenized Young's modulus is nearly the same in all four RVE's.
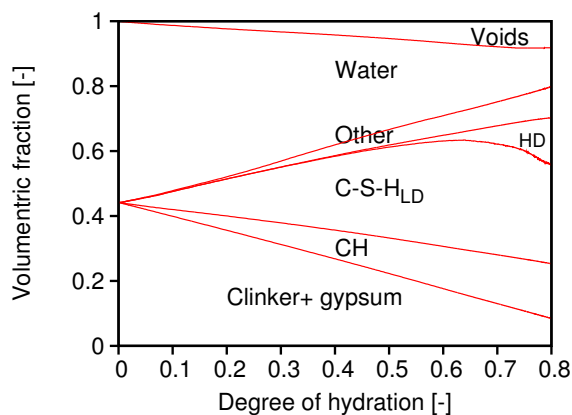


Figure 7.15: Volumetric content of chemical phases during hydration
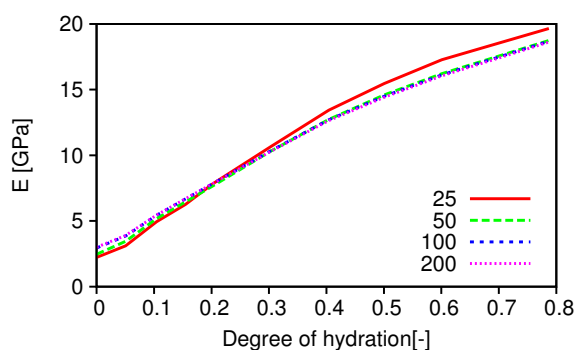


Figure 7.16: Homogenization of rescaled images from $25 \times 25 \times 25$, FFT-based homogenization

Experimental UPV data were recalculated in terms of Young's modulus, Poisson's ratio and the degree of hydration from the released heat. Percolated images of the microstructure $75 \times$

$75 \times 75$ $\mu$m were used during a FFT-based homogenization. The results for Young's modulus, Poisson's ratio and experimental data are in Fig. 7.17.
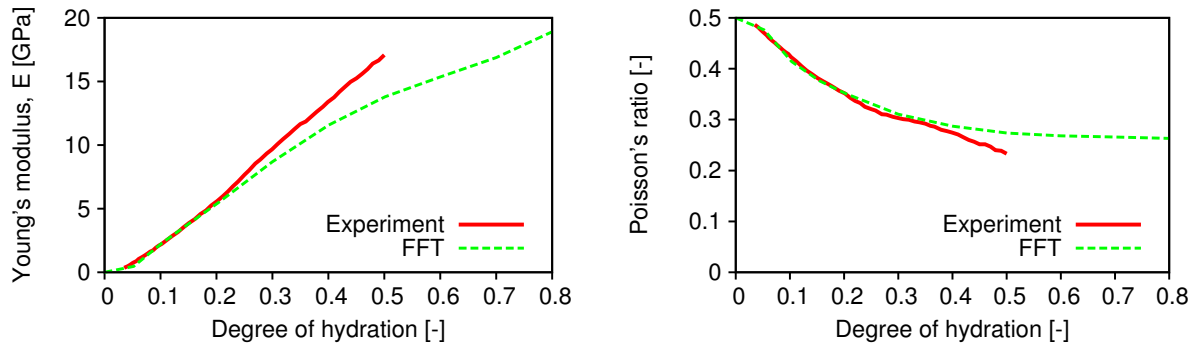


Figure 7.17: Results from FFT-based homogenization, percolated $75 \times 75 \times 75$ $\mu$m, $w/c = 0.4$

### 7.1.5  Paste of Boumiz, w/c = 0.35

A cement paste microstructure was reconstructed with the help of Tab. 7.6. Simulation of this microstructure runs on $75 \times 75 \times 75$ $\mu$m with $3 \times 3 \times 3$ $\mu$m dissolution box with the voxel resolution of 1 $\mu$m. The results from the two-level analytical homogenization are in Figs. 7.18, 7.19 for un/percolated microstructures. The *w/c* of this paste corresponds roughly to 0.318 that was found to correspond for the percolation threshold of the self-consistent scheme [17]. Fig. 7.19 shows in addition the result of the percolated microstructure when the elastic properties of water-filled porosity are set as those of a void. It is clear that such selection does not correspond to the experimental data. The difference in Young's moduli from chosen properties of the water-filled porosity is negligible (not showed).
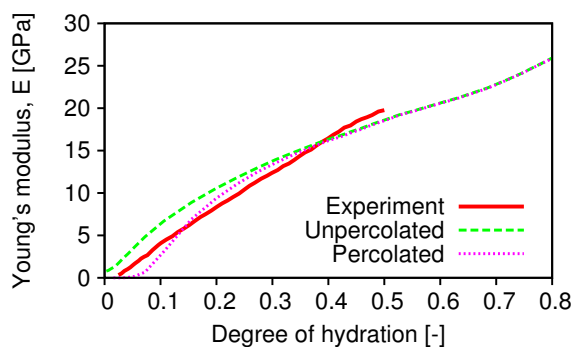


Figure 7.18: Analytically predicted Young's modulus, $w/c = 0.35$
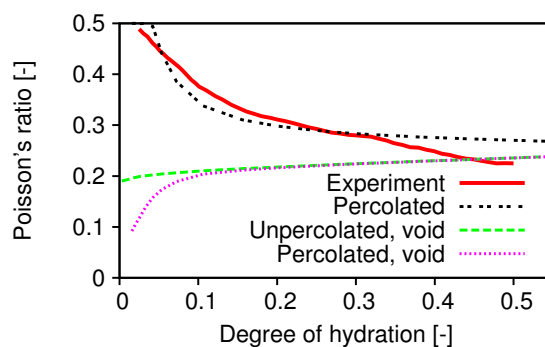
Figure 7.19: Analytically predicted Poisson's ratio, $w/c = 0.35$

One microstructure $25 \times 25 \times 25$ $\mu$m was generated and consequently resized two and three times. This corresponds to the voxel resolution of 1, 0.5 and 0.33 $\mu$m. In order to maintain the affinity between these microstructures, which was assumed, the dissolution box had to be resized from 6 to 26 neighbors. Larger dissolution box than $3 \times 3 \times 3$ $\mu$m is physically unjustified since a dissolved phase might have to jump over a solid voxel [37]. FEM homogenization was performed on the RVE with split nodes and periodic boundary conditions. The results from Fig. 7.20 show that the most critical parameter is the RVE size, corresponding to a voxel resolution, and secondly the dissolving box. The smaller the dissolving box, the more hydration is necessary for small particles in order to obtain the same hydration degree. Then the morphology contains a large unhydrated portion of larger cement grains that are much stiffer than the hydrated phases, which brings less homogeneous body.
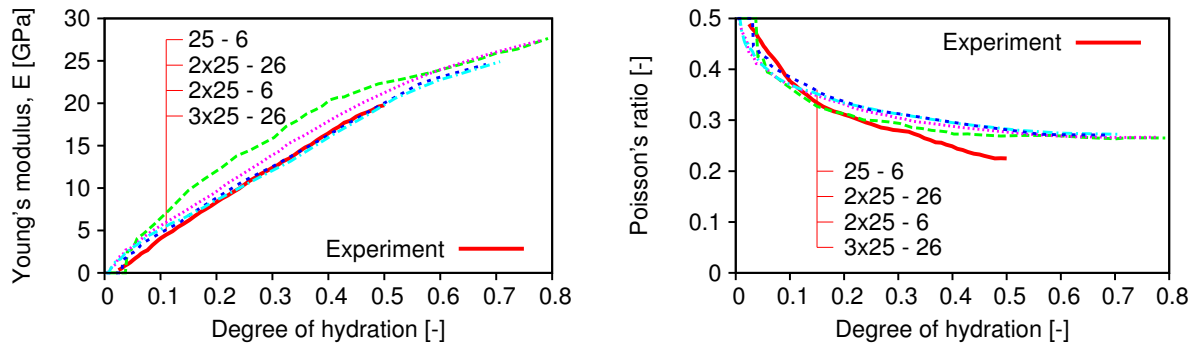


Figure 7.20: Effect of resolution, dissolution neighborhood and RVE size on $E$ modulus and Poisson's ratio, periodic FEM with split nodes

### 7.1.6   BAM cement paste, w/c = 0.3

CEM I 42.5 R with the Bogue composition according to the Tab. 7.7 hydrated at $22^\circ$C, first days in the water and then under sealed conditions. The PSD is known and the amount of particles for each diameter was taken directly from the PSD curve. The tests were conducted in BAM (Bundesanstalt für Materialforschung und -prüfung) under Patrick Fontana.

The heat of hydration was determined in isothermal calorimeter TAM Air at $22^\circ$C. There was no superplasticizer added to the paste, therefore a suspicion was focused on particle flocculation. The simulation with one flocculated particle did not succeed. At later stages, the non-evaporable water content was determined as the mass amount of water that evaporated between 105 and $1000^\circ$C.

Fig. 7.21 displays the normalized released heat, non-evaporable water content and the calorimetric results. In addition, the released heat in $50 \times 50 \times 50$ $\mu$m RVE with 6 dissolution voxels

| Component | C$_3$S | C$_2$S | C$_3$A | C$_4$AF | Gypsum | Anhydrite |
|---|---|---|---|---|---|---|
| Composition | 0.492 | 0.243 | 0.090 | 0.076 | 0.025 (wt.) | 0.025 (wt.) |
| Vol. content | 0.5164 | 0.2496 | 0.100 | 0.0687 | 0.0345 | 0.0307 |
| Blaine fineness | 420 m$^2$/kg | | | | | |
| Autocorr. NIST files [83] | cm115x2f | | | | | |

Table 7.7: Input parameters for German cement microstructure reconstruction
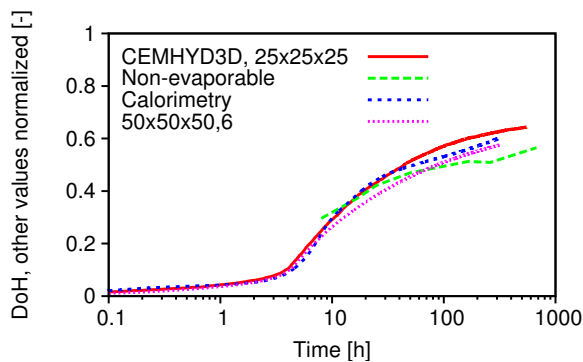


Figure 7.21: Results from simulations and experiments
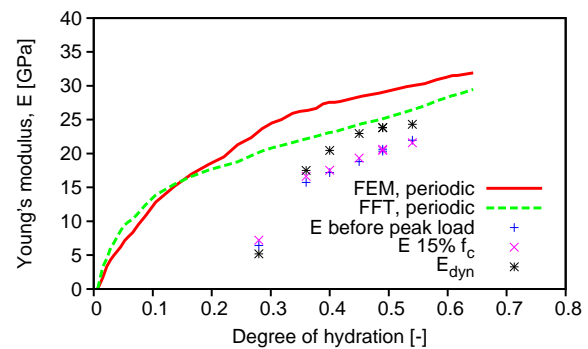


Figure 7.22: Predicted and measured elastic properties, FEM, FFT

neighborhood is plotted, too. In this particular case, there is a better agreement with the measured data after 10 hours of hydration. The parameter $\beta$, Eq. (3.40), for cycle to time conversion is 0.00021 for the full dissolution box and 0.00012 for 6 adjacent voxels. The calorimetric results captured the released heat during early reactions, shortly after mixing with water. On the other hand, when only the heat after minimum heat release in the dormant period is accounted for, the difference is about 20 J/g of cement. The potential heat was assumed as 480 J/g of cement. Non-evaporable water content was recalculated to the degree of hydration, assuming water consumption of 23 % by cement weight.

The percolated microstructure $25 \times 25 \times 25$ $\mu$m was used for homogenization, Fig. 7.22. Experimental Young's modulus was recalculated from the stress-strain diagram of compressive tests at various levels: shortly before the peak load and in 15 % level of the compressive strength. As the second method, ultrasonic pulse velocities were measured. Although the data from both methods are very similar, the discrepancy with numerical homogenization is large, especially at early ages. The secant moduli are definitely lower then the true tangent moduli and the results point rather to difficulties in specimen preparation and to some possible defects, e.g. cracking. In spite of several discussions, there has not been found any reasonable explanation of the discrepancies.

### 7.1.7    Pignat's paste, w/c = 0.45

Pignat used in the experimental program two finenesses of pure $C_3S$ cements [88]. He measured the resonance frequency of $C_3S$ samples of $w/c = 0.45$, where the hydration before testing resembled rather a sealed type of curing. The PSD for coarse and fine cements are in Fig. 7.23.
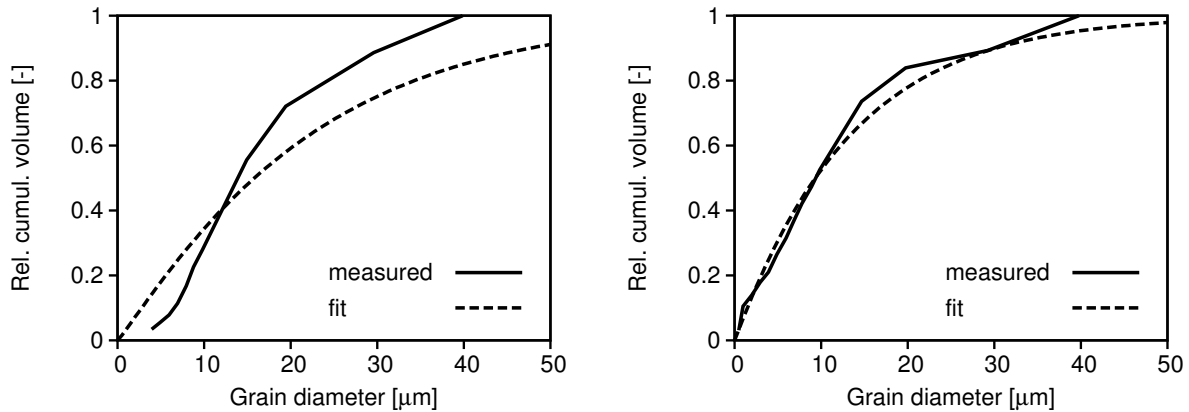


Figure 7.23: PSD fit for coarse (left) and fine (right) cement, according to R-R distribution

Since the Pignat and Navi's hydration model is not limited by a resolution limit, both microstructures were generated and the spherical cement grains thresholded to the smallest sphere diameter of 0.25 $\mu$m. The surface area calculated from the spherical particles yielded directly 146 and 443 m$^2$/kg. These values are rather underestimated since the roughness of cement particles and their shapes are always bigger than those taken from the ideal spheres.

The best fit of points according to Rosin-Rammler distribution with van Breugel's parameters [21] yielded the Blaine fineness of 365 m$^2$/kg for the coarse cement and 573 m$^2$/kg for the fine one, respectively, Fig. 7.23. The fit to the fine cement was good as opposed to the coarse cement due to the truncation of fine particles. If the same roughness and the shape of particles are assumed, the ratio of theoretical finenesses may be rescaled according to the fine cement fit. This gives data of 573 m$^2$/kg for fine and $573 \cdot \frac{146}{443} = 189$ m$^2$/kg for the coarse cement.

The data for elastic moduli were measured from the flexural frequencies on a simply supported cylinders with the diameter of 20 mm and the length of 130 mm for some hydration stages [88]. The self-consistent method yields the Young's modulus around 16 GPa for the degree of hydration at 28 days, estimated as 0.73 by the vector model. Unfortunately, the experimental results yielded value of only 10.8 GPa, therefore these results were not further considered and only a numerical study was conducted.

The coarse microstructures were reconstructed in the vector and the NIST hydration model in $100 \times 100 \times 100$, Fig. 7.24. The volume fractions of four chemical phases were the same
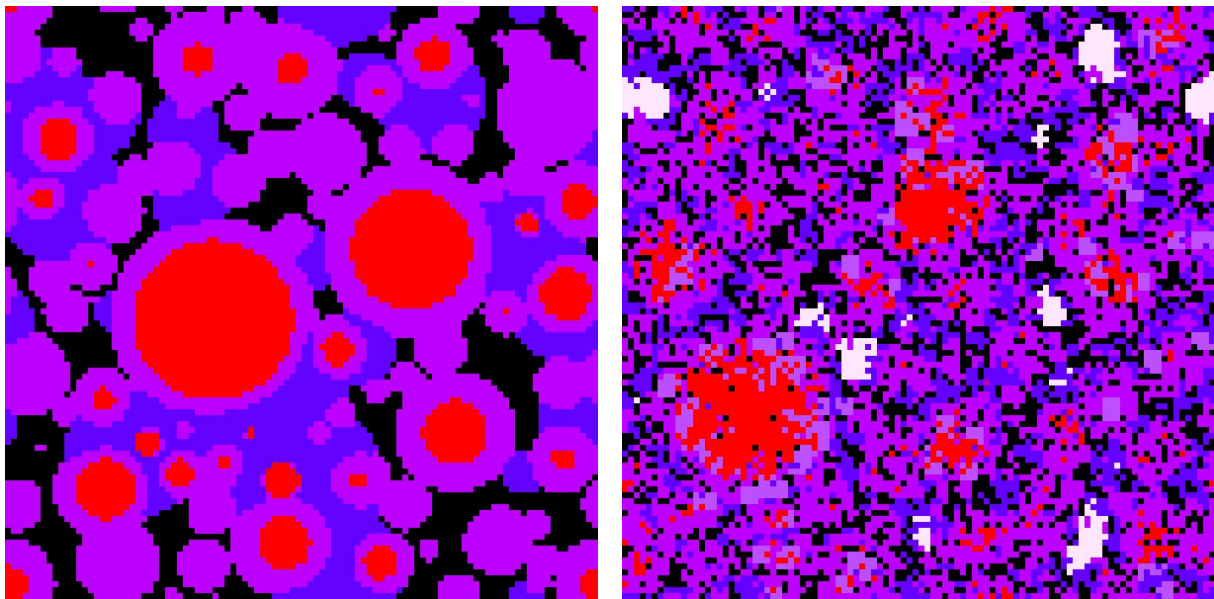
Figure 7.24: Typical microstructure slice $100 \times 100$ from the $C_3S$ cement paste for both models of coarse cements, red = $C_3S$, purple = C-S-H, blue = CH, black = water-filled porosity, white = empty porosity. Degree of hydration is 0.7

in both models, Eq. (3.16), with the difference only in the morphology. The FFT-based homogenization had run on the digital images with the resolution of 1 $\mu$m. Moreover, the 2 $\mu$m resolution was checked for the vector model. The homogenized Young's moduli and Poisson's ratios for both unpercolated microstructures are in Fig. 7.25.
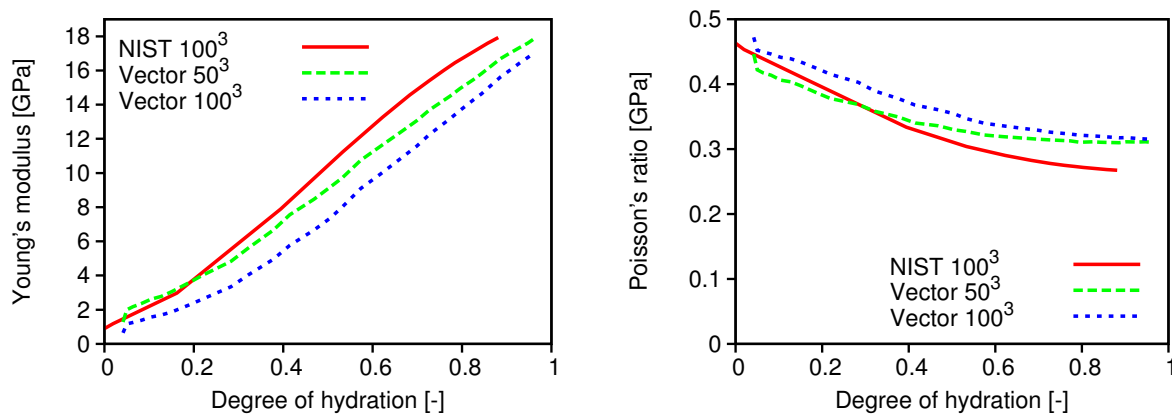


Figure 7.25: Young's modulus and Poisson's ratio for the coarse $C_3S$ cement paste

In this particular case, the vector model with 1 $\mu$m resolution underestimates Young's modulus values and overestimates Poisson's ratio. This effect may be attributed only to morphology. The same conclusion was obtained in the preliminary study of distribution, section 7.1.1.

### 7.1.8   *Performance of two hydration models, w/c = 0.5*

Performance of Pignat and Navi's vector hydration model and NIST discrete hydration model was tested on coarse and fine pure $C_3S$ cement. Two microstructures in each model with $w/c = 0.5$ were reconstructed, in the RVE $200 \times 200 \times 200$ $\mu$m. The Blaine fineness was chosen to correspond to 250 and 500 m$^2$/kg and the PSD was obtained according to parameters from Eqs. (3.33), (3.35), (3.36). The hydration of $C_3S$ was set up in CEMHYD3D model in such a way that it corresponded volumetrically to Eq. (3.16) with the same densities of four phases of Pignat and Navi's model. The sealed conditions and isothermal curing at $20°C$ was prescribed. In order to maintain the volumetric content at the same hydration time, the diffusing voxels has to be transferred to solid counterparts. The empty porosity was always transformed to the water-filled porosity during homogenization. Fig. 7.26 shows the situation for the degree of hydration of 0.8.

Fig. 7.27 displays the comparison of phase fractions for both models in both cements. Generally, due to digitization of a vector image, the tiny CH and C-S-H spheres yield higher volumetric values than the porosity of concave-like structure. In addition, the empty porosity is plotted for NIST hydration model.

The homogenization of FFT-based method ran on unpercolated images. The iterations were set in such a manner that after 50 cycles the relative error had to reach up to 0.8 %. This condition was tested in a variety of Portland cement pastes during all hydration stages against solution after thousands of iterations and it corresponds to max. 2 % of relative error. The vector model generally needed more iterations due to less homogeneous microstructure.

The effective bulk modulus points to a volumetrically softer microstructure from the NIST model in the case of coarse cement. The explanation lies probably in large voids that this hydration model creates in the places of minimal hydraulic radius. Therefore, the largest cavities do not contain under sealed conditions any water which leads to an immobilization of hydration products, Fig. 7.26. Also, the vector model may place portlandite around the nucleation sites distributed randomly within the RVE. Therefore, the hydration products can be brought beyond the C-S-H layer causing additional stiffening. If fine cement is used, no large voids appear and the concentrical microstructure of the vector model is indeed volumetrically softer, Fig. 7.27. On the other hand, the Young's modulus does not reflect this change and Poisson's ratios lay indeed further apart. The shear moduli behave as Young's moduli in both cements.

To conclude these comparisons, the concentrically grown microstructure is generally less stiff than the digital one. The difference in water withdrawal mechanism and nucleation in both models causes an exception, which is remarkable in coarse cements of higher *w/c* where great areas of empty porosity are present, visible as white regions in Fig. 7.26.
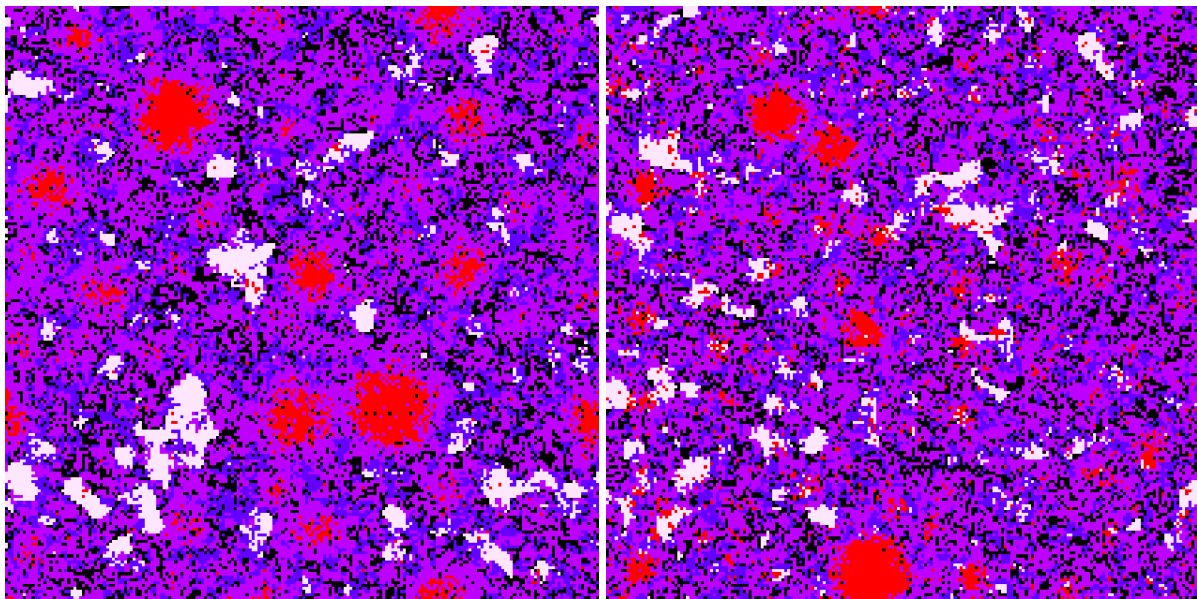
a) NIST discrete model
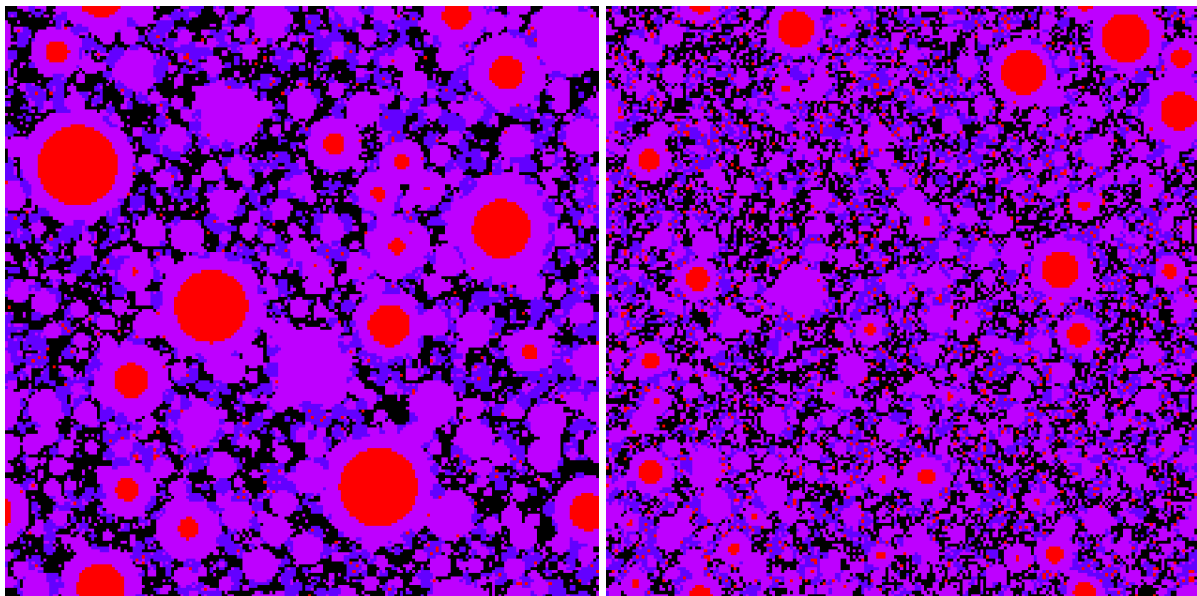


b) Pignat and Navi's vector model

Figure 7.26: Coarse (left) and fine (right) microstructure of $C_3S$ paste at degree of hydration of 0.8, $200 \times 200 \ \mu$m, $w/c = 0.5$, legend in Fig. 7.24

### 7.1.9 Leaching of cement pastes

Parametric study of cement pastes and their degraded counterparts was conducted by Kamali *et al.* [57]. The study was already analyzed with a FEM code Elas3D [36]. They concluded that the Young modulus of degraded cement paste without portlandite may reach only 50 % by
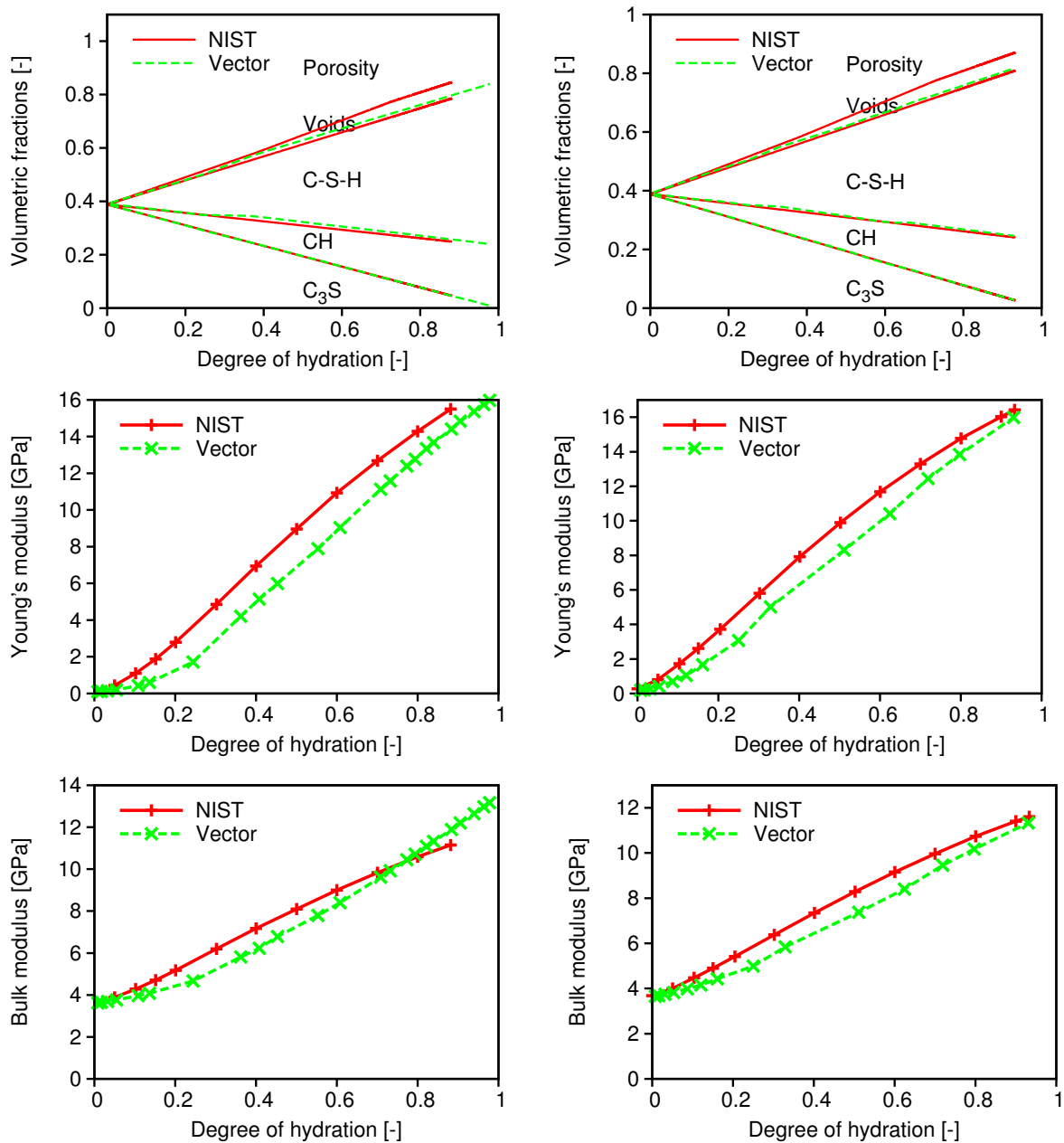
Figure 7.27: Volumetric fractions, Young's modulus and bulk modulus as determined for coarse (left) and fine (right) $C_3S$ powder in discrete NIST and vector hydration model, $w/c = 0.5$

the sound paste. They developed an empirical equation relating the Young modulus to capillary porosity fraction $p_{cap}$ of CEMHYD3D model of sound and degraded cement pastes, Eq. (7.1).

As degradation proceeds, the portlandite, AFt, AFm, C-S-H$_{LD}$ and C-S-H$_{HD}$ become attacked [48]. In this section, we limit the study only to the dissolution of portlandite. Input cement data are the same as in section 7.1.2. It is assumed that degraded cement paste does not

contain any portlandite therefore the water filled porosity is increased by its content.

The $100 \times 100 \times 100$ well-hydrated microstructures of $w/c = 0.25$ and 0.5 were used with a $3 \times 3 \times 3$ dissolution box. The C-S-H$_{HD}$ prediction is again based on a confinement box of 3 $\times$ 3 $\times$ 3 voxels. Calibration to cycles was done on the basis of CH content. Degradation means in our case the dissolution of CH in the cement paste without affecting C-S-H or AFm.

| Item | $w/c = 0.25$ | | $w/c = 0.5$ | |
|---|---|---|---|---|
| | undegraded | degraded | undegraded | degraded |
| Degree of hydration | 0.527 | 0.527 | 0.870 | 0.870 |
| Porosity (vol.) | 9.7 | 25.4 | 23.2 | 39.6 |
| CH (vol.) | 15.7 | 0 | 16.4 | 0 |
| C-S-H$_{LD}$ (vol.) | 22.4 | 22.4 | 39.4 | 39.4 |
| C-S-H$_{HD}$ (vol.) | 18.5 | 18.5 | 12.6 | 12.6 |
| E, Elas3D [GPa] | 32.7 | 19.0 | 18.6 | 8.7 |
| E, analytical [GPa] | 32.27 | 19.51 | 15.27 | 6.70 |
| E, FFT [GPa] | 32.408 | 19.008 | 15.244 | 6.576 |
| $\nu$, analytical [-] | 0.260 | 0.264 | 0.275 | 0.325 |
| $\nu$, FFT [-] | 0.255 | 0.260 | 0.268 | 0.325 |

Table 7.8: Results from sound and leached cement pastes [57]

The results from two-level analytical homogenization combining the Mori-Tanaka and self-consistent scheme are in a good agreement with the results from FFT-based homogenization on percolated images, Tab. 7.8. The FEM code Elas3D predicts slightly higher values than our FEM routine with percolation filtering and split node algorithm.

### 7.2   Initial stress concentration

The results for elastic calculations may point to locations where a stress may concentrate, causing some damage at the next load increment. The failure initializes at some material point already during an elastic behavior. Bearing this fact in mind, several material models may be used to identify this point. The simplest 3D model without additional parameters is the Mieses-Huber-Hencky (MHH) condition in the form of equivalent stress

$$\sigma_{eq} = \sqrt{3J_2} = \frac{\sqrt{2}}{2} \left[ (\sigma_x - \sigma_y)^2 + (\sigma_y - \sigma_z)^2 + (\sigma_z - \sigma_x)^2 + 6(\tau_{xy}^2 + \tau_{yz}^2 + \tau_{zx}^2) \right]^{1/2}, \quad (7.2)$$

where $J_2$ is the second deviatoric invariant. Although the MHH plasticity is not appropriate for brittle materials and for materials with different compressive and tensile ultimate stress, the

trends can be traced down. The well-hydrated cement with $w/c = 0.5$ and $0.25$ were examined using the MHH condition. The equivalent stress was calculated in all integration points across all elements. This corresponds to a monophase porous material where all solid phases are not distinguished. This is justified by Fagerlund's approximation [32] that the strength is proportional to a load-carrying area thus corresponding to the degree of hydration. The microstructure $10 \times 10 \times 10~\mu$m was loaded by the same six components of the eigenstrain vector, with the values of 1.0. Tab. 7.9 summarizes the results.

| *w/c* | 0.5 | 0.25 |
|---|---|---|
| $\sigma_{max}$ [MPa] | -214.6 | -440.6 |
| $\tau_{max}$ [MPa] | -71.5 | -139.5 |
| $\varepsilon_{max}$ [-] | -4.41 | -4.51 |
| $\gamma_{max}$ [-] | -5.4 | -5.78 |
| Internal energy [J] | 61.65 | 126.7 |
| Effective Young's modulus [GPa] | 19.22 | 39.45 |
| $\sigma_{eq,max}$ [MPa] | 169.4 | 330.1 |
| $|\sigma_{max}/\sigma_{eq,max}|$ | 1.267 | 1.335 |

Table 7.9: Results of MHH analysis for $w/c = 0.5$ and $0.25$

It is obvious that the ratio of $\sigma_{max}$ to $\sigma_{max,eq}$ is about the same for both cement pastes thus the MHH condition makes no improvement for the strength prediction simply by some limiting equivalent stress for all phases. In other words, the maximum stress concentration factor is about the same in both cement pastes. Since the macroscopic stiffness ratio is around two, the total accumulated mechanical energy by the same eigenstrain is also two times higher in these RVE's. If the paste with $w/c = 0.5$ was loaded by approximately two-times higher eigenstrain, very similar results would come out as in the case of $w/c = 0.25$. Under the uniaxial loading, the loading force is calculated as $F = EA\varepsilon$, where $E$ and $A$ take into account the whole cross-sectional area. Since $A$ is a constant and the ultimate linear elastic stress is to be the same for two different *w/c*'s, the strength is then proportional to $E$ therefore to the degree of hydration. This is partially supported by experiments of Igarashi *et al.* [53] for each sample where porosity is directly proportional to the degree of hydration, Fig. 7.28.
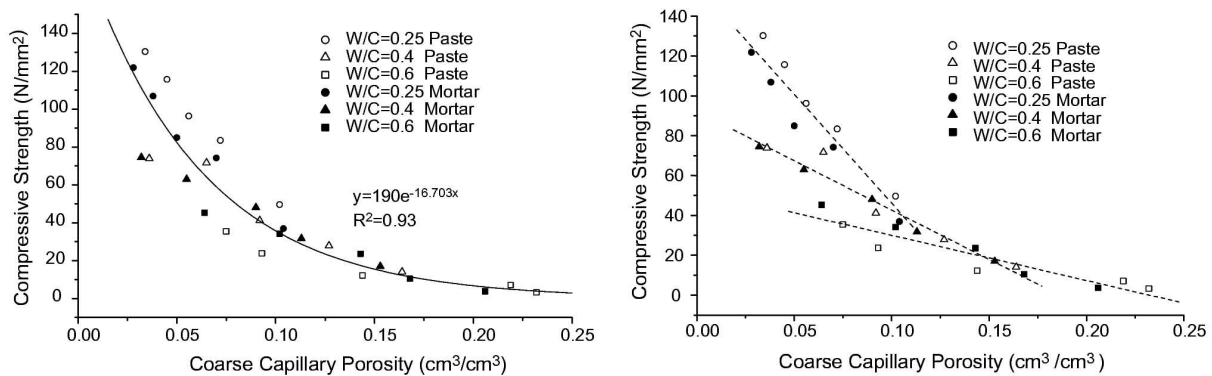
Figure 7.28: Relationship between compressive strength and coarse capillary porosity, exponential and linear regressions on each *w/c* set [53]

## 7.3 *Mortar level incorporating ITZ*

Mortar, as a composite medium, can be considered as a three phase system: cement paste, interfacial transition zone (ITZ) and aggregates including sand and other inert materials. Elastic effective response of such a composite is given, as in the case of cement paste, by arrangement and intrinsic properties of individual components. Considerable number of experiments explored an effect of each phase in concrete with conclusions used further in this section. Numerical and analytical modeling of concrete was done in a considerably smaller amount of cases. As an example, a three-layer built-in analytical model [68] and numerical 2D model [81] validated experiments on real mortar or concrete samples. Yang [131] studied the mortars using combination of two analytical methods: firstly he homogenized a spherical aggregate together with an ITZ by means of the double-inclusion method, and secondly using the Mori-Tanaka theory of homogenized inclusion and bulk cement paste.

The generally accepted thickness of ITZ is $20 - 50$ $\mu$m, where the cement paste composition differs significantly from the bulk one. The direct observation via an image analysis of maturing concrete was carried out by Diamond and Huang [27] with the statement of low cement particle content in the ITZ compared to the bulk paste. They observed the wall-effect around an aggregate but found an increase of porosity from 6 to 9 % when compared to the mature paste. However, they attributed the reduced mechanical properties dominantly to the wall-effect, Fig. 7.29. Since a great mechanical contrast of intrinsic properties exists between unhydrated cement clinker and hydrated phases, the reduction of effective Young's modulus is quite obvious. This was supported by experiments that showed important role of this transition zone and significant change of mechanical properties, e.g. a polymer film on the surface of aggregates [99].

Neubauer *et al.* [81] found by inverse numerical simulation from the experimental values,
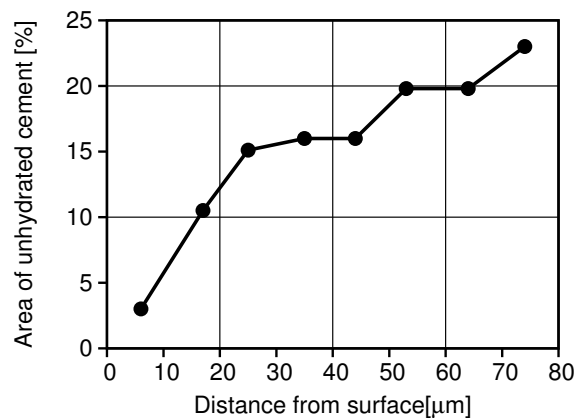
Figure 7.29: The morphology of ITZ of the concrete in dependence of distance from aggregate, $w/c = 0.5$, [27]

that Young's modulus of the ITZ lies between one third and one half of the modulus of bulk cement paste. This was supported by independent experiments on leached cement pastes [48]. Similar results were found by Yang [131] for the ITZ thickness of 20 $\mu$m, where Young's modulus lies between 20 and 40 % of the bulk paste, while for the ITZ thickness of 40 $\mu$m being from 50 to 70 % of the Young's modulus of the bulk paste. He concluded that the effective elastic properties are influenced the most by the volume fraction of sand in the mortar. Hashin and Monteiro [45] studied the effect of thickness and moduli reduction of the ITZ on a three-phase axisymmetric model. They used the ITZ thickness of 25 $\mu$m and concluded that Young's modulus and Poisson's ratio are reduced by 50 % in the ITZ.

Li *et al.* [68] developed a three-phase model, based on a 3-layer sphere assemblage, section 5.5. Neubauer, Jennings and Garboczi [81] developed a 2D, three phase, numerical model embedding a spherical coarse aggregate with a shell of given thickness in a matrix of a cement paste.

### 7.3.1 *Mortar by Yang, w/b = 0.3*

The effect of the ITZ will be studied on a typical well-hydrated cement mortar. The homogenization scheme of Hervé and Zaoui [47] will be used to find the elastic properties of equivalent homogeneous medium. The derivation and assumptions of the analytical homogenization scheme were derived and discussed in section 5.5. The data from Yang's study will be used in order to be able to reproduce the results [131]. He assumed the average diameter of Otawa sand as 450 $\mu$m and the thickness of the ITZ being 20 $\mu$m. OPC paste with $w/b = 0.3$ (including silica fume) has Young's modulus of 20.76 GPa, Poisson's ratio of 0.2. Young's

modulus of aggregate is 80 GPa, Poisson's ratio 0.21. He measured elastic response of that mortar, containing volume fractions of sand as 0, 0.1, 0.2, 0.3, 0.4, and 0.5.

The first study assumes a two-phase composite: a sand grain covered with a thin layer of ITZ of 20 $\mu$m thickness. The volume fraction of sand is $225^3/245^3 = 0.7745$. The ITZ occupies the rest of available space, i.e. 0.2255. Such inclusion is embedded in an equivalent homogeneous medium. The ITZ zone will have Young's modulus as a fraction of that of the bulk cement paste, Poisson's ratio will remain the same in the ITZ, i.e. $\nu = 0.2$. Since the well-ordered moduli are maintained for these two phases (disregarding the reference phase), the Herve-Zaoui scheme corresponds to Hashin-Shtrikman estimation of a lower bound for a two-phase medium. The results are in Tab. 7.10, together with Hori and Nemat-Nasser's scheme used by Yang [131]. The lower Hashin-Shtrikman bound is significantly lower than the estimation from Hori and Nemat-Nasser's model.

| Sand | ITZ | | Results | | | | |
|---|---|---|---|---|---|---|---|
| | $E_{ITZ}/E_{paste}$ | $E_{ITZ}$ | $E$ | $\nu$ | $k$ | $\mu$ | $E^{Hori}$ |
| $E = 80.000$ | 0.0 | 0.000 | 0.000 | 0.200 | 0.000 | 0.000 | - |
| $\nu = 0.210$ | 0.1 | 2.076 | 13.611 | 0.212 | 7.604 | 5.663 | 35.783 |
| $k = 45.977$ | 0.2 | 4.152 | 23.351 | 0.203 | 13.097 | 9.707 | 38.563 |
| $\mu = 33.058$ | 0.3 | 6.228 | 30.692 | 0.204 | 17.264 | 12.749 | 41.140 |
| | 0.4 | 8.304 | 36.442 | 0.203 | 20.544 | 15.129 | 43.535 |
| | 0.5 | 10.380 | 41.083 | 0.205 | 23.202 | 17.048 | 45.768 |
| | 0.6 | 12.456 | 44.920 | 0.205 | 25.406 | 18.634 | 45.768 |
| | 1.0 | 20.760 | 55.473 | 0.206 | 31.490 | 22.991 | - |

Table 7.10: Effect of ITZ properties in a cement mortar. A sand particle with 450 $\mu$m diameter is covered with a 20 $\mu$m thick ITZ. $E^{Hori}$ are results from Hori and Nemat-Nasser's model [131]

In a real mortar, there are two parameters which remain unknown: the ITZ thickness and elastic modulus in the ITZ phase (assuming the same Poisson's ratio). Yang [130] found that increasing the ITZ thickness is somehow equivalent to increasing the elastic modulus of the ITZ zone. For the ITZ thickness of 20 $\mu$m, he found the results between $0.2 - 0.4$ $E_{paste}$ and for the thickness of 40 $\mu$m, he deduced that Young's modulus lies between 0.5 and 0.7 of $E_{paste}$. The results for a 3-layered concentric spheres are in Fig. 7.30. A reasonable reduction of Young's modulus of the ITZ zone seems to be 0.5. The results that are in accordance with Yang [131] and Neubauer [81].
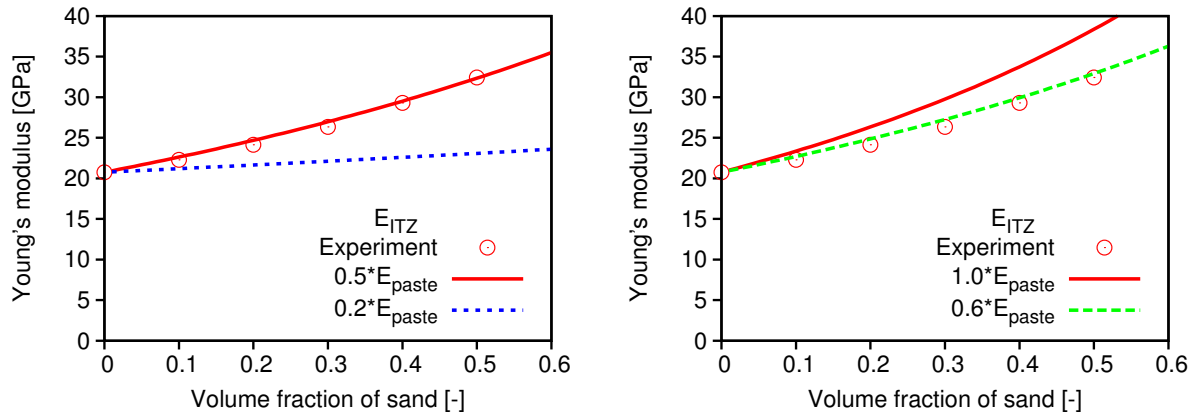
Figure 7.30: Effect of ITZ thickness and Young's modulus reduction in the ITZ on effective properties, for ITZ thickness of 20 $\mu$m (left) and 40 $\mu$m (right)

### 7.3.2 Mortar B60 of Boumiz, w/c = 0.387

Boumiz *et al.* [20] studied the elastic properties of cement mortars with the grey OPC and with added superplasticizer. The input parameters are in Tab. 7.11. Siliceous filler was added in order to correct granulometric curve of sand and the plasticizer to improve workability (slightly increased the amount of water). The more adequate name would be the concrete mortar since grains bigger than 2 mm are used as well in the mixtures, see Tab. 7.12. The specific surface of the cement is not known, but Bernard *et al.* [17] use the value of 760 $m^2$/kg since the cement is fast and of high performance type. The 5 vol. % content of gypsum is assumed to be added to the cement for the setting regulation. The clinker minerals as recalculated according to Newkirk [80], corresponding well to the input parameters as used in work of Bernard *et al.* [17].

| Component | $C_3S$ | $C_2S$ | $C_3A$ | $C_4AF$ | Gypsum |
|---|---|---|---|---|---|
| Newkirk composition | 0.643 | 0.096 | 0.083 | 0.06 | - |
| Vol. content | 0.697 | 0.101 | 0.095 | 0.056 | 0.05 |
| Blaine fineness | | | 760 $m^2$/kg | | |
| Autocorr. NIST files [83] | | | cm115x2f | | |

Table 7.11: Input parameters for Boumiz's cement in B60 mortar

The simulation ran on $50 \times 50 \times 50$ microstructure and with the 26 voxel dissolving neighborhood. Fig. 7.31 shows the development of $E$ modulus depending on previous percolation filtering before the FFT-based homogenization. The values from the percolated microstructure are used further. The sand is considered as $E = 70$ GPa, $\nu = 0.17$, the average grain radius is

| Component | Size range | Weight | Density | Volume |
|---|---|---|---|---|
| - | [$\mu$m, mm] | [kg] | [g/cm$^3$] | [dm$^3$] |
| Cement | 0.1 – 40 $\mu$m | 729.6 | 3.15 | 231.6 |
| Water | – | 257.5 | 1.0 | 257.5 |
| Sand | 0 – 5 mm | 1244.7 | 2.65 | 469.8 |
| Siliceous filler | 2 – 200 $\mu$m | 51.5 | 2.65 | 19.4 |
| Plasticizer (melamine-based) | – | 25.4 | 1.17 | 21.7 |

Table 7.12: Mortar composition in 1 m$^3$, $w/c = 0.387$ [20]

assumed as 400 $\mu$m, the thickness of ITZ is assumed as 20 $\mu$m so the volume fraction of ITZ is 8.24 %. The coefficient of reduction of $E$ modulus in the ITZ is 0.6 or 1.0, i.e. no reduction in the second case. The results together with the experimental ultrasonic data are in Fig. 7.32.
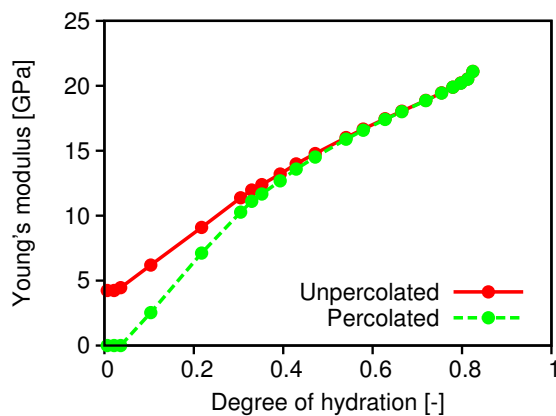


Figure 7.31: Development of $E$ modulus in plain cement paste, FFT homogenization
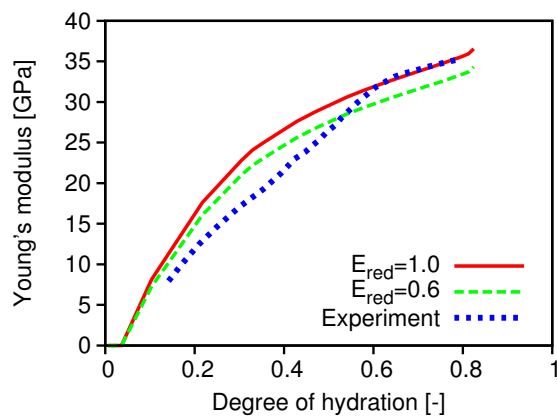


Figure 7.32: Effect of ITZ on the homogenized elastic properties of mortar

### 7.3.3 Mortar B35 of Boumiz, w/c = 0.524

The experiments are similar as in the previous section with slightly different cement composition but with the same sand [20]. The sand grain is in the range of 0 – 5 mm with an average grain radius of 400 $\mu$m. The composition of cement and mortar is summarized in Tabs. 7.13, 7.14.

The microstructure 50 $\times$ 50 $\times$ 50 $\mu$m ran with the 26 voxel dissolving neighborhood. The coefficient for cycle to time scaling is 0.0003 and the dormant period was determined as 5 hours

| Component | $C_3S$ | $C_2S$ | $C_3A$ | $C_4AF$ | Gypsum |
|---|---|---|---|---|---|
| Newkirk composition | 0.660 | 0.0714 | 0.0625 | 0.0626 | - |
| Vol. content | 0.720 | 0.077 | 0.094 | 0.058 | 0.05 |
| Blaine fineness | | | 760 m$^2$/kg | | |
| Autocorr. NIST files [83] | | | cm115x2f | | |

Table 7.13: Input parameters for Boumiz's cement in B35 mortar

| Component | Size range | Weight | Density | Volume |
|---|---|---|---|---|
| - | [$\mu$m, mm] | [kg] | [g/cm$^3$ ] | [dm$^3$] |
| Cement | $0.1 - 40 \ \mu$m | 567.6 | 3.15 | 180.2 |
| Water | – | 292 | 1.0 | 292.1 |
| Sand | $0 - 5$ mm | 1335.4 | 2.65 | 503.9 |
| Siliceous filler | $2 - 200 \ \mu$m | 50.1 | 2.65 | 18.9 |
| Plasticizer (melamine-based) | – | 5.7 | 1.17 | 4.9 |

Table 7.14: Mortar composition in 1 m$^3$, $w/c = 0.524$ [20]

by fitting to calorimetric data, Fig. 7.33. The amount of readily soluble alkali was also fitted to that heat curve. In addition, the affinity model with parameters from Tab. 3.2 was plotted. Homogenized values for the cement paste together with the ITZ at the mortar level are plotted in Fig. 7.34. Percolated cement microstructure was used, with a guaranty of nearly zero $E$ modulus at early ages.
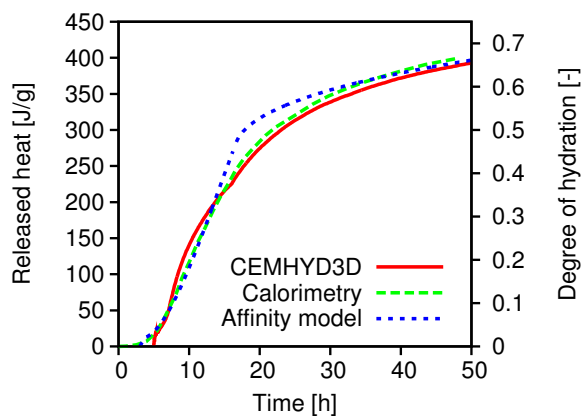


Figure 7.33: Released heat during early-ages
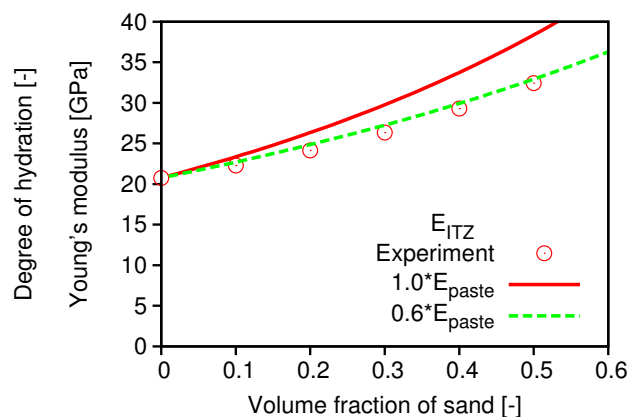
Figure 7.34: Effect of ITZ properties on the homogenized elastic properties of mortar

### 7.4  Concrete level

The results from homogenization at the cement paste or mortar level may be further upscaled to the concrete level. Presented results are based on experiments conducted by Lee *et al.* [67]. A series of concrete batches was prepared and the specimens were measured in a compression test for elastic response according to ACTM C469. The mixture proportions and cement specifications are summarized in Tab. 7.15, the unknown parameters included: amount of gypsum in the cement, elastic properties and average radii of fine and coarse aggregates, and the ITZ thickness.

| Component | $C_3S$ | $C_2S$ | $C_3A$ | $C_4AF$ | Gypsum |
|---|---|---|---|---|---|
| Blaine composition | 0.54 | 0.1852 | 0.0857 | 0.0919 | - |
| Vol. content | 0.588 | 0.197 | 0.0987 | 0.086 | 0.03 |
| Blaine fineness | 345 m$^2$/kg | | | | |
| Autocorr. NIST files [83] | cm115x2f | | | | |

| W/c | | 0.5 | | 0.27 | |
|---|---|---|---|---|---|
| Component | Density | Weight | Volume | Weight | Volume |
| - | [g/cm$^3$] | [kg/m$^3$] | [dm$^3$] | [kg/m$^3$] | [dm$^3$] |
| Cement | 3.15 | 370 | 117.4 | 550 | 174.6 |
| Water | 1.0 | 185 | 185 | 148 | 148 |
| Plasticizer | 1.0 | 0 | 0 | 3.55 | 3.55 |
| Air | - | 0 | 30.1 | 0 | 26.5 |
| Fine aggregates | 2.51 | 754 | 300.4 | 617 | 245.8 |
| Coarse aggregates | 2.64 | 969 | 367.05 | 1060 | 401.5 |

Table 7.15: Cement specification and concrete composition in 1 m$^3$, $w/c = 0.5$ and 0.27 [67]

For both $w/c = 0.5$ or 0.27, the properties were chosen in the following manner: the fine aggregate was a siliceous sand $E = 60$ GPa, $\nu = 0.2$, average diameter 1 mm and the ITZ thickness 20 $\mu$m. The coarse aggregate was a crushed granite, $E = 40$ GPa, $\nu = 0.2$, average diameter 15 mm and the ITZ thickness 20 $\mu$m.

Since some air is present in the mixture, the first homogenization approach put the air at the cement paste level, considered as an entrained air. The Mori-Tanaka scheme with the reference medium of cement paste was used for this purpose. The self-consistent scheme provided very similar results since the air content was up to 3 % (vol). The multi-scale homogenization

employed further two times Hervé and Zauoi's scheme for the mortar and concrete level. The fine aggregate at the center with an associated ITZ zone were homogenized with cement paste including air. The reduction of Young's modulus in the ITZ was considered as 0.5, unaffecting the Poisson ratio. After that, the coarse aggregate at the center with an associated ITZ zone were added to the homogenized mortar level. The elastic properties of ITZ were based again on the cement paste. This uncoupled approach arrived to the elastic properties of concrete with entrained air at the cement paste level.
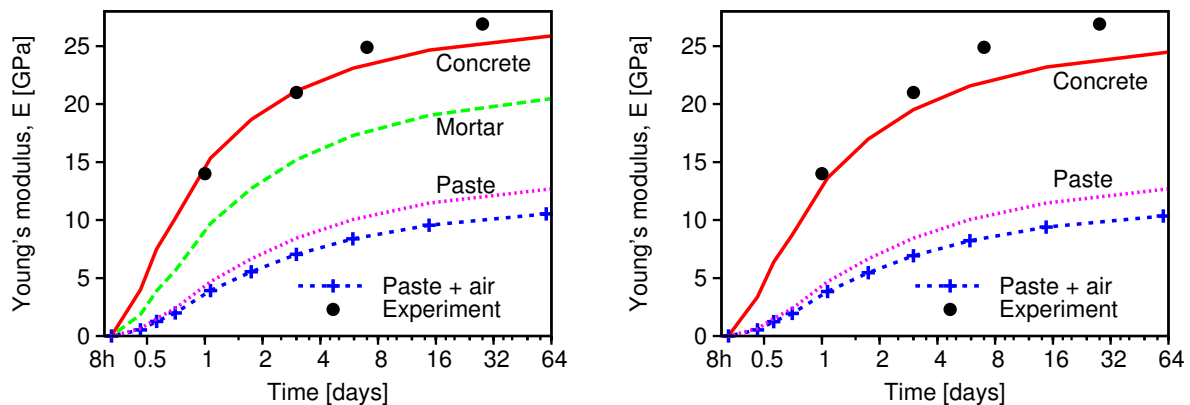


Figure 7.35: Young's modulus of cement paste, mortar and concrete. Multi-scale homogenization (left) and all-in-one (right), $w/c = \mathbf{0.5}$

To check the assumption of level separation, all phases above the cement paste level were homogenized at one step (from center): coarse aggregates, associated ITZ, fine aggregates, associated ITZ, cement paste + air. The Hervé and Zaoui scheme with five spheres in a reference medium was used again, Fig. 7.35. Although a different physical meaning of both schemes exists, the results are not far apart. The results show a similar trend for different homogenization levels, compare with Tab. 5.1. When the porosity from all levels, excluding intrinsic porosities of phases, is taken to the highest level, the reduction of elastic properties is the most significant.

The set point of concrete was determined from the cement paste level and corresponds to unrealistically high dormant period (8 and 9 hours). As long as the cement paste does not reach the solid percolation threshold, the Hervé and Zauoi scheme will predict nearly the same low stiffness. Therefore, this homogenization scheme always guarantees that the initial period will be treated correctly. Since no early experimental points are known, the calibration of the CEMHYD3D hydration model was based on late experimental data only. The calibration would not be problematic and might be used for the prediction of concrete elastic properties during the whole hydration period.

The same experiments with the same parameters were conducted for concrete with $w/c =$

0.27. In this particular case, the differences in the Young modulus should be more obvious since the cement paste has a higher stiffness. The results are again in a good agreement with experiments, again with unrealistically long dormant period Fig. 7.36.
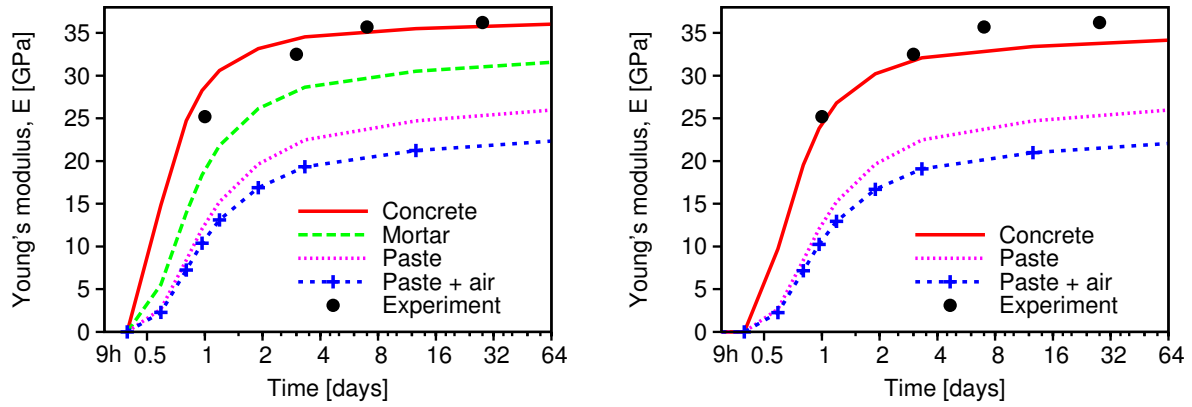


Figure 7.36: Young's modulus of cement paste, mortar and concrete. Mortar and concrete level (left) and all-in-one (right), $w/c = \mathbf{0.27}$

Chapter 8

# CONCLUSION AND FUTURE WORK

The following research objectives were accomplished in the Ph.D. thesis:

- evolving microstructures of cement paste were predicted from initial reconstructed cement paste image. CEMHYD3D, affinity, Pignat and Navi's hydration models were considered for this purpose and mutually compared. Implemented cement reactions were based on the theories of Powers and his coworkers, extended with contemporary knowledge of cement hydration,

- evolving microstructures were adapted for consecutive linear elastic homogenization. A new algorithm, separating C-S-H$_{LD}$ and C-S-H$_{HD}$ at the C-S-H level was proposed and validated for cement pastes. Proposed confinement condition is easy for implementation and calibration, the later hydration stages agree well with the J-T model [113],

- the solid percolation filtering was introduced in order to treat early hydration ages shortly after the solid percolation threshold. The filtering has significant effect up to the degree of hydration of approximately 0.3,

- the microstructure of cement paste reflects an effect of chemical cement composition, particle size distribution, hydration temperature and curing conditions in CEMHYD3D model. The homogenization results depend upon these factors,

- analytical homogenization found perfect application at the C-S-H level, where the elastic properties of building C-S-H units were obtained by means of inverse analysis. In addition, good results were obtained for later hydration stages of various cement pastes. The conspherical scheme of Hervé and Zauoi is indispensable for mortar and concrete level where the appropriate morphology including ITZ is well represented. The multiscale approach in cement-based materials can be based reasonably on analytical methods,

- numerical elastic homogenization methods provided more accurate results for the whole hydration time at the cement paste level. The results from FEM or FFT-based approach are mutually comparable. An introduction of split nodes in the FEM homogenization releases a stress concentration at sharp corners without the need of RVE remeshing,

- FFT-based homogenization method was found as the fastest for the RVE with periodic boundary conditions. Good representation of stress and strain periodic fields paves the way for precise analysis,

- FEM allows the calculation of apparent properties via static or kinematic uniform boundary conditions over the RVE. The periodic boundary conditions yielded the lowest fluctuation of apparent properties at various RVE sizes but not necessarily the lowest scatter,

- the need for larger RVE is remarkable especially at early ages and in higher *w/c*, reasonable size is up to $50 \times 50 \times 50$ $\mu$m in a typical cement paste.

Fig. 8.1 summarizes the Young modulus of analyzed cement pastes from this work via the FFT-based approach. The linearity is observed when $w/c \geq 0.35$, while a more progressive growth of $E$ modulus is observed in early hydration stages when $w/c < 0.35$. The reason of such behavior is the solid percolation, significant at lower *w/c*'s.
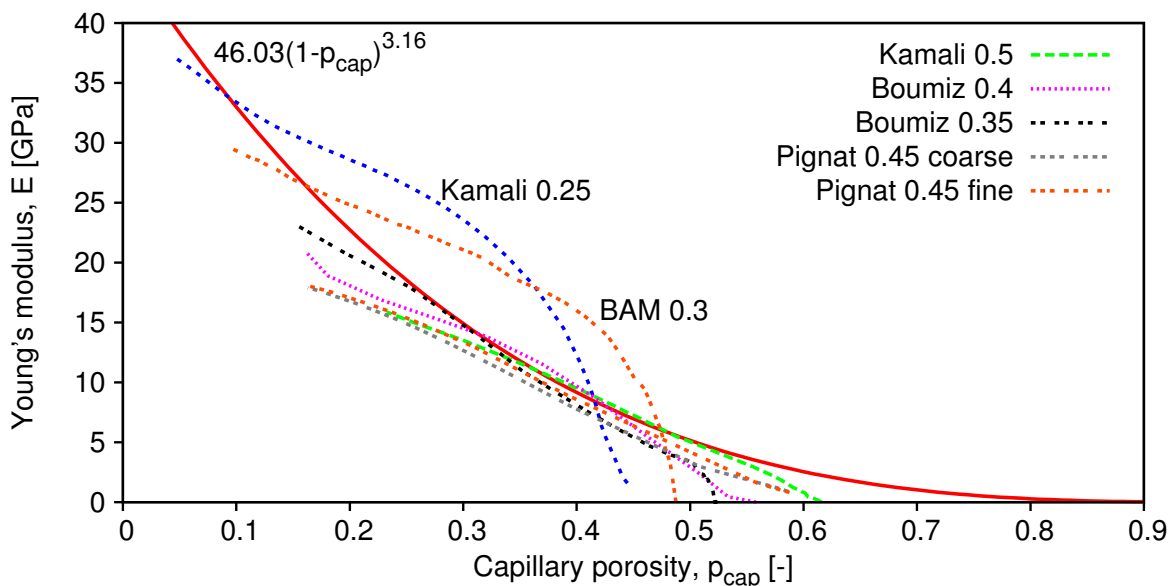


Figure 8.1: Young's moduli of analyzed cement pastes, FFT homogenization, RVE size 25–100 $\mu$m, empirical relation according to Eq. (7.1)

The results of FFT homogenization for the cement paste were replotted in terms of the degree of hydration as well. The fit to the following formulae, covering the range $w/c \in (0.25, 0.5)$

and for the whole hydration period with asymptotic properties, yields

$$\text{Young's modulus [GPa]} = a(\alpha - \alpha_p)^b \geq 0.001, \tag{8.1}$$

$$\alpha_p = 0.0485 \ w/c, \text{ see Eq. (4.4)}, \tag{8.2}$$

$$a = \frac{1}{0.14 \ w/c^{1.35}}, \tag{8.3}$$

$$b = 2.15 \ w/c - 0.08, \ b \leq 1. \tag{8.4}$$

with the correlation coefficient of 0.989 for all disrete points in Fig. 8.2. The maximum degree of hydration for Portland cement paste according to Hansen [41] is $\frac{w/c}{0.36}$, Fig. 8.2.
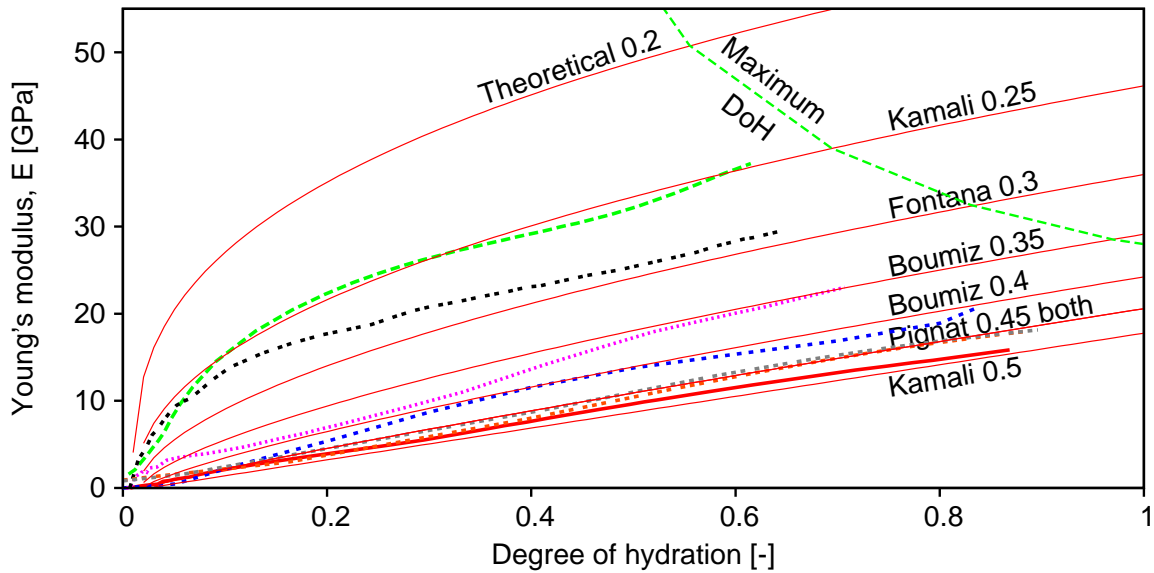


Figure 8.2: Young's moduli from the FFT homogenization, RVE size 25–100 $\mu$m, and the fit according to Eq. (8.1)

The linear elastic homogenization model may be extended to a nonlinear material model, e.g. creep behavior. The success of Bažant's creep models [3] based on microprestress could be physically justified at the C-S-H level of cement paste. The inverse analysis of experimental data might provide intrinsic creep parameters for C-S-H and predict micromechanically the concrete creep.

# BIBLIOGRAPHY

[1] P. Acker: **Micromechanical analysis of creep and shrinkage mechanisms.** In: F.-J. Ulm, Z.P. Bažant, F.H. Wittmann (Eds.), Creep, Shrinkage and Durability Mechanics of Concrete and Other Quasi-Brittle Materials. Proc. of Sixth Int. Conference CON-CREEP6, Elsevier, Oxford, UK, pp. 15–25, 2001.

[2] M. Avrami: **Kinetics of Phase Change I.** Journal of Chemical Physics, pp. 1103–1108, 1939.

[3] Z.P. Bažant, A.B. Hauggaard, S. Baweja, F.-J. Ulm: **Microprestress-Solidification Theory for Concrete Creep. I: Aging and Drying Effects.** Jornal of Engineering Mechanics, pp. 1188–1194, 1997.

[4] Z.P. Bažant, and S. Prasannan: **Solidification theory for concrete creep: I. Formulation.** J. Engng. Mech., 115 (8), pp. 1691–1703, 1989.

[5] J.J. Beaudoin: **Comparison of mechanical properties of compacted calcium hydroxide and Portland cement paste systems.** Cement and Concrete Research 13, pp. 319–324, 1983.

[6] A. van Beek: **Dielectric properties of young concrete, non-destructive dielectric sensor for monitoring the strength development of young concrete.** PhD Thesis, Delft University of Technology, Delft, 2000.

[7] F.G. Bell: **A survey of the engineering properties of some anhydrite and gypsum from the north and midlands of England.** Engineering Geology 38 (1-2), pp. 1–23, 1994.

[8] D.P. Bentz: **CEMHYD3D: A Three-Dimensional Cement Hydration and Microstructure Development Modeling Package. Version 2.0.** Building and Fire Research Laboratory Gaithersburg, Maryland 20899, 2000.

[9] D.P. Bentz: **A Three-Dimensional Cement Hydration and Microstructure Program. I. Hydration Rate, Heat of Hydration, and Chemical Shrinkage.** National Institute

of Standards and Technology, Building and Fire Research Laboratory, NISTIR 5756, Gaithersburg, Maryland 20899, 1995.

[10] D.P. Bentz: **CEMHYD3D: A Three-Dimensional Cement Hydration and Microstructure Development Modeling Package. Version 3.0.** Building and Fire Research Laboratory Gaithersburg, Maryland 20899, June 2005.

[11] D.P. Bentz, E.J. Garboczi, C.J. Haecker, O.M. Jensen: **Effect of cement particle size distribution on performance properties of Portland cement-based materials.** Cement and Concrete Research 29, pp. 1663–1671, 1999.

[12] D.P. Bentz, E.J. Garboczi, K.A. Snyder: **A Hard Core/Soft shell Microstructural Model for Studying Percolation and Transport in Three-Dimensional Composite Media.** Building and Fire Research Laboratory Gaithersburg, NIST, Maryland 20899, 1999.

[13] D.P. Bentz: **Influence of Alkalis on Porosity Percolation in Hydrating Cement Pastes.** Cement and Concrete Composites 28 (5), pp. 427-431, 2006.

[14] D.P. Bentz: **Modeling the Influence of Limestone Filler on Cement Hydration Using CEMHYD3D.** Cement and Concrete Composites 28 (2), pp. 124–129, 2006.

[15] D.P. Bentz, D.A. Quenard, V. Baroghel-Bouny, E.J. Garboczi, H.M. Jennings: **Modelling drying shrinkage of cement paste and mortar. Part I. Structural models from nanometres to milimetres.** Materials and Structures 28, pp. 450–458, 1995.

[16] R. Berliner, M. Popovici, K. W. Herwig, M. Berliner, H. M. Jennings, J. J. Thomas: **Quasielastic Neutron Scattering Study of the Effect of Water-to-Cement Ratio on the Hydration Kinetics of Tricalcium Silicate.** Cem. Concr. Res. 28 (2), pp. 231–243, 1998.

[17] O. Bernard, F.-J. Ulm, E. Lemarchand: **A multiscale micromechanics-hydration model for the early-age elastic properties of cement-based materials.** Cement and Concrete Research 33 (9), pp. 1293–1309, 2003.

[18] J.G. Berryman: **Mixture Theories for Rock Properties**, in Rock Physics and Phase Relations - A Handbook of Physical Constants, edited by T.J. Ahrens (American Geophysical Union, Washington DC), pp. 205–228., 1995.

[19] A. Bezjak, I. Jelenic: **On the determination of rate constants for hydration process in cement pastes.** Cem. Concr. Res. 10 (4), 553–563, 1980.

[20] A. Boumiz, C. Vernet, F.C. Tenoudji: **Mechanical Properties of Cement Pastes and Mortars at Early Ages.** Advanced Cement Based Materials, pp. 94–106, 1996.

[21] K. van Breugel: **Simulation of hydration and formation of structure in hardening cement-based materials.** Second edition, Delft University Press, 1997. Parts of it reprinted as **Numerical simulation of hydration and microstructure development in hardening cement-based materials.** Cement and Concrete Research 25 (2), pp. 319–331 & 25 (3), pp. 522–530, 1995.

[22] S. Broadbent, J. Hammersley: **Percolation processes. I. Crystals and mazes.** Proc. Camb. Phil. Soc. 53, pp. 629–641, 1957.

[23] R.M. Christensen, K.H. Lo: **Solutions for effective shear properties in three phase sphere and cylinder models**, J. Mech. Phys. Solids, 27, 315–330, 1979; ibid., Erratum, J. Mech. Phys. Solids, 34, 639, 1986.

[24] G. Constantinides, F.-J. Ulm: **The effect of two types of C-S-H on the elasticity of cement-based materials: results from nanoindentation and micromechanical modeling.** Cement and Concrete Research, 34 (1), pp. 67–80, 2004.

[25] W. Czernin: **Cement Chemistry and Physics for Civil Engineers.** Bauverlag GmbH, Wiesbaden und Berlin, second edition, 1980.

[26] S. Diamond, D. Bonen: **Microstructure of hardened cement paste - a new interpretation.** J. Am. Ceram. Soc. 76 (12), pp. 2993–2999, 1993.

[27] S. Diamond, J. Huang: **The ITZ in concrete - a different view based on image analysis and SEM observations.** Cement and Concrete Composites 23, pp.179–188, 2001.

[28] D.D. Double, A. Hellawell, S.J. Perry: **The hydration of Portland cement.** Proc. R. Soc. London A369, 1978.

[29] W. J. Drugan, J. R. Willis: **A micromechanics-based nonlocal constitutive equation and estimates of representative volume element size for elastic composites.** J. Mech. Phys. Solids 44, pp. 497–524, 1996.

[30] R.J. van Eijk, H.J.H. Brouwers: **Study of the relation between hydrated Portland cement composition and leaching resistance.** Cement and Concrete Research 28, pp. 815–828, 1998.

[31] J.D. Eshelby: **The determination of the elastic field of an ellipsoidal inclusion and related problems.** Proc. of Royal Society, Series A 241, pp. 376–396, 1957.

[32] G. Fagerlund: **Relations between the Strength and the Degree of Hydration or Porosity of Cement Paste, Cement Mortar and Concrete.** Cementa Report T87023, Danderyd, 1987.

[33] R.F. Feldman, P.J. Sereda: **A new model for hydrated Portland cement and its practical implications.** Engineering Journal (Canada) 53 (8/9), pp. 53–59,1970.

[34] S. Feng, B.I. Halperin, P.N. Sen: **Transport properties of continuum systems near the percolation threshold.** Phys. Rev. B 35, pp. 197–214, 1987.

[35] K. Fuji, W.J. Kondo, J. Am. Ceram. Soc. 57, pp. 492–502, 1974.

[36] E.J. Garboczi: **Finite Element and Finite Difference Programs for Computing the Linear Electric and Elastic Properties of Digital Images of Random Materials.** NIST, Building and Fire Research Laboratory, Gaithersburg, MD, 1998.

[37] E.J. Garboczi, D.P. Bentz: **The effect of statistical fluctuation, finite size error, and digital resolution on the phase percolation and transport properties of the NIST cement hydration model.** Cem. Conc. Res. 31 (10), pp. 1501–1514, 2001.

[38] M. Geiker: **Studies of Portland Cement Hydration: Measurement of Chemical Shrinkage and a Systematic Evaluation of Hydration Curves by Means of the Dispersion Model.** PhD. Thesis, Technical University of Denmark, Lyngby, 1983.

[39] N.M. Ghoniem *et al.* : **Multiscale modelling of nanomechanics and micromechanics: an overview.** Philosophical Magazine, pp. 3475–3528, 2003.

[40] A.A. Gusev: **Representative volume element size for elastic composites: A numerical study.** J. Mech. Phys. Solids, 45 (9), pp. 1449–1459, 1997.

[41] T.C. Hansen: **Physical structure of hardened cement paste. A classical approach.** Matèriaux et Constructions 114 (19), pp. 423–436, 1986.

[42] Z. Hashin: **Analysis of composite materials - a survey.** ASME J. Appl. Mech. 50, pp. 481–505, 1983.

[43] Z. Hashin: **The elastic moduli of heterogeneous materials.** Journal of Applied Mechanics 29, pp. 143–150, 1962.

[44] Z. Hashin, S. Shtrikman: **A variational approach to the theory of the elastic behavior of multiphase materials.** Journal of Mechanics and Physics of Solids 10, pp. 343–352, 1963.

[45] Z. Hashin, P.J.M. Monteiro: **An inverse method to determine the elastic properties of the interphase between the aggregate and the cement paste.** Cement and Concrete Research 32, pp. 1291–1300, 2002.

[46] S. Hazanov, C. Huet: **Order relationships for boundary-conditions effect in heterogeneous bodies smaller than the representative volume.** Journal of the Mechanics and Physics of Solids 42 (12), pp. 1995–2011, 1994.

[47] E. Hervé, A. Zaoui: **N-layered Inclusion-based Micromechanical Modelling.** Int. J. Engng Sci. 31, pp. 1–10, 1993.

[48] F.H. Heutkamp, F.-J. Ulm: **Chemomechanics of calcium leaching of cement-based materials at different scales : the role of CH-dissolution and C-S-H degradation on strength and durability performance of materials and structures.** PhD thesis, Department of Civil and Environmental Engineering, MIT, 2002.

[49] R. Hill: **Continuum micro-mechanics of elastoplastic polycrystals.** J. Mech. Phys. Sol. 13, pp. 89–101, 1965.

[50] R. Hill: **Elastic properties of reinforced solids - Some theoretical principles.** Journal of the Mechanics and Physics of Solids 11, pp. 357–372, 1963.

[51] R. Hill: **Theory of mechanical properties of fiber-strengthened materials. - III: Self-consistent model.** J. Mech. Phys. Solids 13, 189–198, 1965.

[52] C. Huet: **Application of variational concepts to size effects in elastic heterogeneous bodies.** J. Mech. Phys. Solids 38, pp. 813–841, 1990.

[53] S. Igarashi, M. Kawamura, A. Watanabe: **Analysis of cement pastes and mortars by a combination of backscatter-based SEM image analysis and calculations based on the Powers model.** Cement and Concrete Composites 26, pp. 977–985, 2004.

[54] I. Jawed, J. Skalny, J.F. Young: **Hydration of Portland cement.** in P. Barnes: Structure and Performance of Cements. Applied Science Publisher, 1983.

[55] H.M. Jennings: **A model for the microstructure of calcium silicate hydrate in cement paste.** Cement and Concrete Research 30 (6), pp. 101–116, 2000.

[56] J.G. de Jong, H.N. Stein, J.M. Stevels: **Hydration of tricalcium silicate**. J. Appl. Chem. 17, 1967.

[57] S. Kamali, M. Moranville, E.G. Garboczi, S. Prené, B. Gérard: **Hydrate Dissolution Influence on the Young's Modulus of Cement Paste.** Proc. Fracture Mechanics of Concrete Structures (FraMCoS-V), Li et al. (Eds.), Vail, 2004.

[58] T. Kanit *et al.*: **Determination of the size of the representative volume element for random composites: statistical and numerical approach.** International Journal of Solids and Structures 40, pp. 3647–3679, 2003.

[59] H.J. Kim, C.C. Swan: **Algorithms for automated meshing and and unit cell analysis of periodic composites with hierarchical tri-quadric tetrahedral elements.** International Journal for Numerical Methods in Engineering, 2003.

[60] E.A. Koenders, K. van Breugel: **Numerical modelling of autogenous shrinkage of hardening cement paste**. Cement and Concrete Research 30 (12), pp. 1911–1914, 2000.

[61] K. Kolář, T. Klečka, J. Kolísko: **Vliv superplastifikátorů nové generace na objemové změny cementových kompozitů.** XI. mezinárodní sympozium Sanace betonových konstrukcí, květen 2001.

[62] M. Krauss, K. Hariri, F.S. Rostásy: **Non-Destructive Assessment of Mechanical Properties of Concrete at Very Early Age by US Techniques - Method, Results and Modelling.** IPACS, report BE96-3843/2001:12–5, 2001.

[63] G.T. Kuster, M.N. Toksöz: **Velocity and attenuation of seismic waves in two-phase media: I. Theoretical formulation.** Geophysics 39, pp. 587–606, 1974.

[64] D.A. Lange, H.M. Jennings, S.P. Shah: **Image analysis techniques for characterization of pore structure of cement-based materials.** Cem. Concr. Res. 24 (5), pp. 841–853, 1994.

[65] J.L. Laugesen: **Density functional calculations of elastic properties of portlandite, CaOH$_2$.** Cem. Concr. Res. 35 (2), pp. 199-203, 2005.

[66] F. Lea: **Lea's Chemistry of Cement and Concrete.** Elsevier, fourth edition, 2004.

[67] H.K. Lee, K.M. Lee, Y.H. Kim, H. Yim, D.B. Dae: **Ultrasonic in-situ monitoring of setting process of high-performance concrete.** Cement and Concrete Research 34, pp. 631–640, 2004.

[68] G. Li, Y. Zhao, S.S. Pang: **A Three-layer Built-in Analytical Modeling of Concrete.** Cement and Concrete Research 28, pp. 1057–1070, 1998.

[69] F.W. Locher, W. Richartz, S. Sprung: **Erstarren von Zement. Teil II: Einfluss des Calciumsulfatzusatzes.** Zement-Kalk-Gips 33 (6), pp. 271–277, 1980.

[70] K. Maekawa, R. P. Chaube, T. Kishi: **Modeling of Concrete Performance.** E & FN SPON (London), 1999.

[71] P.K. Mehta, P.J.M. Monteiro: **Concrete - Microstructure, Properties and Materials.** Prentice-Hall, Englewood Cliffs, New Jersey, 1993.

[72] J.C. Michel, H. Moulinec, P. Suquet: **Effective properties of composite materials with periodic microstructure: a computational approach.** Comput. Methods Appl. Engrg. 172, pp. 109–143, 1999.

[73] S. Mindness, J.F. Young: **Concrete.** Prentice Hall, Inc., New Jersey, 1981.

[74] H. Moosberg-Bustnes, B. Lagerblad, E. Forssberg: **The function of fillers in concrete.** Mat. Struct. 37, pp. 74–81, 2004.

[75] T. Mori, K. Tanaka: **Average stress in matrix and average elastic energy of materials with misfitting inclusions.** Acta Metallurgica 21 (5), pp. 1605–1609, 1973.

[76] H. Moulinec and P. Suquet: **A fast numerical method for computing the linear and nonlinear mechanical properties of composites.** Comptes Rendus de l'Academie des Sciences Serie II 318 (11), pp. 1417–1423, 1994.

[77] J.C. Nadeau: **A multiscale model for effective moduli of concrete incorporating ITZ water-cement ratio gradients, aggregate size distributions, and entrapped voids.** Cement and Concrete Research 33, pp. 103–113, 2003.

[78] A. Nagy: **Determination of E-modulus of Young Concrete With Nondestructive Method.** Journal of Materials in Civil Engineering, pp. 15–20, 1997.

[79] A.M. Neville: **Properties of concrete.** John Wiley & Sons, fourth edition, 1997.

[80] T. F. Newkirk: **The alkali phases in Portland cement clinker.** Proc. of the 3rd Int. Symp. on the Chem. of Cem., London, pp.151–171, 1952.

[81] C.M. Neubauer, H.M. Jennings, E.J. Garboczi: **A Three-Phase Model of the Elastic and Shrinkage Properties of Mortar.** Advanced Cement-based Materials 4, pp. 6–20, 1996.

[82] L.F. Nielsen: **Strength development in hardened cement paste: examination of some empirical equations.** Materials and Structures 26, pp. 255-260, 1993.

[83] NIST, visible cement database http://visiblecement.nist.gov/

[84] I. Odler: **Discussion of the paper "A model for the microstructure of calcium silicate hydrate in cement pastes" by H. M. Jennings.** Cement and Concrete Research 30, pp. 1337–1338, 2000.

[85] R.A. Olson, B.J. Christensen, R.T. Coverdale, S.J. Ford, G.M. Moss, H.M. Jennings, T.O. Mason, E.J. Garboczi: **Interpretation of the impedance spectroscopy of cement paste via computer modelling: III. Microstructural analysis of frozen cement paste.** J. Mater. Sci. 30, pp. 5078–5086, 1995.

[86] K.-B. Park, T. Noguchi, J. Plawsky: **Modeling of hydration reactions using neural networks to predict the average properties of cement paste.** Cement and Concrete Research 35 (9), pp. 1676-1684, 2005.

[87] C. Pignat, P. Navi, K. Scrivener: **Characterization of the pore space in hardening cement paste to predict the autogenous shrinkage.** Laboratory of Construction materials, Lausanne, Switzerland, 2002.

[88] C. Pignat: **Simulation numérique de l'hydratation du silicate tricalcique, caractérisation de la structure poreuse et de la perméabilité.** Thèse No. 2763, EPFL, Lausanne, 2003.

[89] S. Popovics: **Effect of Porosity on the Strength of concrete.** Journal of Material 4 (2), June, pp. 356–371, 1969.

[90] C. Porteneuve, H. Zanni, C. Vernet, K.O. Kjellsen, J.-P. Korb, D. Petit: **Nuclear magnetic resonance characterization of high- and ultrahigh-performance concrete. Application to the study of water leaching.** Cem. Con. Res. 31, pp. 1887–1893, 2001.

[91] C. Porteneuve, J.-P. Korb, D. Petit, H. Zanni: **Structure - texture correlation in ultrahigh-performance concrete. A nuclear magnetic resonance study.** Cem. Con. Res. 32, pp. 97–101, 2002.

[92] T.C. Powers, T.L. Brownyards: **Studies of physical properties of hardened Portland cement paste.** Research Laboratories of the Portland Cement Association, Chicago, March, Bulletin 22, 1948.

[93] S.J. Preece *et al.*: **On the initial stages of cement hydration.** School of Mathematics and Statistics, University of Birmingham, Edgbaston, B15 2TT, Kluwer Academic Publishers, 2000.

[94] A. Princigallo, K. van Breugel, G. Levita: **Influence of the aggregate on the electrical conductivity of Portland cement concretes.** Cement and Concrete Research 33 (11), pp. 1755–1763, 2003.

[95] I.G. Richardson: **The nature of C-S-H in hardened cements.** Cement and Concrete Research 29, pp. 1131–1147, 1999.

[96] I.G. Richardson: **The nature of the hydration products in hardened cement pastes.** Cement and Concrete Composites 22, pp. 97–113, 2000.

[97] M.D. Rintoul, S. Torquato: **Precise determination of the critical threshold and exponents in a three-dimensional continuum percolation model.** J. Phys. A:Math. Gen. 30, pp. 585–592, 1997.

[98] A.P. Roberts, E.J. Garboczi: **Elastic properties of model porous ceramics**. J. Amer. Ceram. Soc., 83, No. 12, pp. 3041–3048, (2000). National Institute of Standards and Technology, Gaithersburg, MD 20899, USA, 2000.

[99] E. Sakai, J. Sugita: **Composite Mechanism of Polymer Modified Cement.** Cement and Concrete Research 25, pp. 127–135, 1995.

[100] E.M. Schulson: **Ice Damage to Concrete.** Special report 98-6, US Army Corps of Engineers, 1998.

[101] F. Schüth, K.S.W. Sing, J. Weitkamp (eds.): **Handbook of Porous Solids.** Chapter 6.11. Cement as porous material, $1^{st}$ edition, Wiley-vch, 2002.

[102] G. De Schutter, L. Taerwe: **Degree of hydration-based description of mechanical properties of early age concrete.** Materials and Structures, 29 (7), pp. 335–344, 1996.

[103] G. De Schutter, L. Taerwe: **General hydration model for Portland cement and blast furnace slag.** Cement and Concrete Research 25 (3), pp. 593–604, 1995.

[104] K. Scrivener, P. Pratt: **Back-scattered electron images of polished cement sections in scanning electron microscope.** Proceeding of the 6th International Conference on Cement Microscopy. New Mexico; pp.145–155, 1984.

[105] SIFEL. **SImple Finite ELements.** Open-source C++ package. *http://cml.fsv.cvut.cz/ ˜sifel/index.html*

[106] P. Simeonov, S. Ahmad: **Effect of transition zone on the elastic behavior of cement-based composites.** Cement and Concrete Research 25, pp. 165–176, 1995.

[107] T. Slamečka, F. Škvára: **The Effect of Water Ratio on Microstructure and Composition of the Hydration Products of Portland Cement Pastes.** Ceramics - Silikáty 46 (4), pp. 152–158, 2002.

[108] V. Šmilauer, Z. Bittnar: **Effects of representative cube size on the simulation of Portland cement hydration in CEMHYD3D model.** in: J. Walraven, J. Blaauwendraad, T. Scarpas, B. Snijder (Eds.), $5^{th}$ International PhD Symposium in Civil Engineering, A. A. Balkema Publishers, pp. 581-587, 2004.

[109] Z. Sun, G. Ye, T. Voigh, S.P. Shah, K. van Breugel: **Microstructural aspects of cement hydration - ultrasonic waves and numerical simulation.** In: J. Walraven, J. Blaauwendraad, T. Scarpas, B. Snijder (Eds.), $5^{th}$ International PhD Symposium in Civil Engineering, A. A. Balkema Publishers, pp. 971–979, 2004.

[110] H.F.W. Taylor: **Cement Chemistry.** Academic Press, New York, 1990.

[111] K. Theisen, F.L. Smidth: **Quantitative determination of clinker phases and pore structure using image analysis.** World Cement Resarch and Development, 1997.

[112] J.J. Thomas, H.M. Jennings, A.J. Allen: **Determination of the Neutron Scattering Contrast of Hydrated Portland Cement Paste Using $H_2O/D_2O$ Exchange.**, Advn. Cem. Based Mat. 7, pp. 119–122, 1998.

[113] P.D. Tennis, H.M. Jennings: **A model for two types of calcium silicate hydrate in the microstructure of Portland cement pastes.** Cement and Concrete Research 30, pp. 855–863, 2000.

[114] F. Tomosawa, T. Noguchi, K. Onoyama: **Investigation of Fundamental Mechanical Properties of High-strength Concrete.** Summaries of Technical Papers of Annual Meeting of Architectural Institute of Japan, pp. 497–498, 1990.

[115] S. Torquato: **Connection between the morphology and effective properties of heterogeneous materials.** Macroscopic Behavior of Heterogeneous Materials for the Microstructure 147, Am. Soc. Mech. Eng., pp. 53–65, 1992.

[116] S. Torquato: **Modeling of physical properties of composite matrials.** International Journal of Solids and Structures, vol. 37, pp. 411–422, 2000.

[117] S. Torquato: **Random Heterogenous Materials. Microstructure and Macroscopic Properties.** Springer-Verlag, 2001.

[118] J.M. Torrenti, F. Benboudjema: **Mechanical threshold of cementitious materials at early age.** Materials and Structures, vol. 38, no. 277, pp. 299–304, 2005.

[119] F. Tzschichholz, H. J. Herrmann, H. Zanni: **Reaction-Diffusion Model for the Hydration and Setting of Cement.** Phys. Rev. E vol. 53, pp. 2629–37, 1996.

[120] L.J. Walpole: **On the overall elastic moduli of composite materials.** J. Mech. Phys. Solids 17, pp. 235–251, 1969.

[121] J. Wang, J. Lubliner, P. Monteiro: **Effect of ice formation on the elastic moduli of cement paste and mortar.** Cement and Concrete Research 18, pp. 874–885, 1988.

[122] F. Vallee: **Modeling Drying, hydration, carbonation in thin mortars using CEMHYD3D.** Building and Fire Research Laboratory NIST, June 2000.

[123] K. Velez *et al.*: **Determination by nanoindentation of elastic modulus and hardness of pure constituents of Portland cement clinker.** Cement and Concrete Research 31, pp. 555–561, 2001.

[124] G.J. Verbeck, R.H. Helmuth: **Structures and Physical Properties of Cement Paste.** Proceedings of the 5th International Symposium on the Chemistry of Cement, V. 3, pp. 1–37, 1969.

[125] G. Washer, P. Fuchs, B. Graybeal: **Elastic Properties of Reactive Powder Concrete**. International Symposium (NDT-CE 2003) of Non-Destructive Testing in Civil Engineering, 2003.

[126] M. Wierer: **Multiscale Analysis of Woven Composites.** PhD thesis, Czech Technical University in Prague, CTU, 2004.

[127] E. Wirquin, M. Broda, B. Duthoit: **Determination of the apparent activation energy of one concrete by calorimetric and mechanical means. Influence of a superplasticizer.** Cement and Conrete Research 32, pp. 1207–1213, 2002.

[128] F.H. Wittmann: **Estimation of the modulus of elasticity of calcium hydroxide.** Cement and Concrete Research 16 (6), pp. 971–972, 1986.

[129] C.K. Yan: **On homogenization and de-homogenization of composite materials.** Ph.D. Thesis. Drexel University, Philadelphia, PA, 2003.

[130] C.C. Yang, R. Huang: **A Two-phase Model for Predicting the Compressive Strength of Concrete.** Cement and Concrete Research 10, vol. 26, pp. 1567–1577, 1996.

[131] C.C. Yang: **Effect of the transition zone on the elastic moduli of mortar.** Cement and Concrete Research 28 (5), pp. 727–736, 1998.

[132] G. Ye, K. van Breugel, A.L.A. Fraaij: **Three-dimensional microstructure analysis of numerically simulated cementitious materials.** Cem. Concr. Res. 33, pp. 215–222, 2003.

[133] A. Zaoui: **Continuum Micromechanics: Survey.** Journal of Engineering Mechanics, pp. 808–816, 2002.

[134] J. Zeman: **Analysis of composite materials with random microstructure.** CTU reports, ČVUT, Prague, 2003.

## Appendix A

# HERVÉ-ZAOUI SCHEME

The problem of split spherical inclusions was solved by Hervé and Zaoui [47]. The interaction between adjacent phases may be reduced to stress, strain or displacement continuity, resulting in a recurrent scheme of $n$ layers. First, consider a pure volumetric displacement in infinity. The radial displacement field reads:

$$u_r^i = F_i r + \frac{G_i}{r^2},$$ (A.1)

where $F_i$ and $G_i$ are unknown constant. The corresponding stresses are:

$$\sigma_{rr}^i = 3k_i F_i - \frac{4\mu_i}{r^3} G_i,$$ (A.2)

$$\sigma_{\theta\theta}^i = \sigma_{\phi\phi}^i = 3k_i F_i + \frac{2\mu_i}{r^3} G_i,$$ (A.3)

$$\sigma_{r\theta}^i = \sigma_{r\phi}^i = \sigma_{\theta\phi}^i = 0.$$ (A.4)

The interface between two spheres has the radius $r = R_k$. The continuity of $\sigma_{rr}^k$ and displacement $u_r^k$ is maintainted. This may be written in the compact form:

$$\boldsymbol{J}_k(R_k)\boldsymbol{V}_k = \boldsymbol{J}_{k+1}(R_k)\boldsymbol{V}_{k+1},$$ (A.5)

$$\boldsymbol{J}_i(R_i) = \begin{bmatrix} r & \frac{1}{r^2} \\ 3k_i & -\frac{4\mu_i}{r^3} \end{bmatrix}, \boldsymbol{V}_i = \begin{bmatrix} F_i \\ G_i \end{bmatrix}.$$ (A.6)

The reccurent scheme for the phase $k + 1$ is determined from the $k$-th phase:

$$\boldsymbol{N}_k = \boldsymbol{J}_{k+1}^{-1}(R_k)\boldsymbol{J}_k(R_k),$$ (A.7)

$$\boldsymbol{V}_{k+1} = \boldsymbol{N}_k\boldsymbol{V}_k,$$ (A.8)

$$\boldsymbol{V}_{k+1} = \prod_{j=k}^{1} \boldsymbol{N}_j\boldsymbol{V}_1 = \boldsymbol{Q}_k\boldsymbol{V}_1.$$ (A.9)

Eq. (A.9) leads to:

$$F_1 = \frac{1}{Q_{11,n}} F_{n+1},$$ (A.10)

and the coefficients $F_k$ and $G_k$ for $k \in [1, n]$ are derived as:

$$F_k = \frac{Q_{11,k-1}}{Q_{11,n}} F_{n+1},$$ (A.11)

$$G_k = \frac{Q_{21,k-1}}{Q_{11,n}} F_{n+1},$$ (A.12)

in $n + 1$ layer where the radius is infinite, $\boldsymbol{G}_{n+1} = 0$, thus Eq. (A.9) may be reformulated:

$$\boldsymbol{V}_{n+1} = \boldsymbol{N}_n \prod_{j=n-1}^{1} \boldsymbol{N}_j \boldsymbol{V}_1 = \boldsymbol{N}_n \boldsymbol{Q}_{n-1} \boldsymbol{V}_1. \tag{A.13}$$

Substituing the terms for $\boldsymbol{N}$ yields the effective bulk modulus:

$$k = \frac{3k_n R_n^3 Q_{11,n-1} - r\mu_n Q_{21,n-1}}{3R_n^3 Q_{11,n-1} + 3Q_{21,n-1}}, \tag{A.14}$$

where the load of $n + 1$ sphere of $F_{n+1}$ may be arbitrary.

Having solved the radial displacement, the shear contributions are to be solved in the similar manner:

$$u_r^i = U_r^i(r) \sin^2\theta \cos 2\phi, \tag{A.15}$$

$$u_\theta^i = U_\theta^i(r) \sin\theta \cos\theta \cos 2\phi, \tag{A.16}$$

$$u_\phi^i = U_\phi^i(r) \sin\theta \cos 2\phi. \tag{A.17}$$

$$\tag{A.18}$$

The unknowns parameters $U_r^i(r), U_\theta^i(r), U_\phi^i(r)$ are obtained from equilibrium equations and yield in the matrix notation:

$$\boldsymbol{L}_k(R_k)\boldsymbol{W}_k = \boldsymbol{L}_{k+1}(R_k)\boldsymbol{W}_{k+1} \qquad, \tag{A.19}$$

$$\boldsymbol{L}_i(r) = \begin{bmatrix} r & -\frac{6\nu_i}{1-2\nu_i}r^3 & \frac{3}{r^4} & \frac{5-4\nu_i}{r^2-2\nu_i r^2} \\[2mm] r & -\frac{7-4\nu_i}{1-2\nu_i}r^3 & -\frac{2}{r^4} & \frac{2}{r^2} \\[2mm] \mu_i & \frac{3\nu_i}{1-2\nu_i}\mu_i r^2 & \frac{-12}{r^5}\mu_i & \frac{2\nu_i\mu_i-10\mu_i}{r^3-2\nu_i r^3} \\[2mm] \mu_i & -\frac{7+2\nu_i}{1-2\nu_i}\mu_i r^2 & \frac{8}{r^5}\mu_i & \frac{2\mu_i+2\mu_i\nu_i}{r^3-2\nu_i r^3} \end{bmatrix}, \boldsymbol{W}_i = \begin{bmatrix} A_i \\[2mm] B_i \\[2mm] C_i \\[2mm] D_i \end{bmatrix}. \tag{A.20}$$

The recurent scheme for the phase $k + 1$ is determined from the $k$-th phase:

$$\boldsymbol{M}_k = \boldsymbol{L}_{k+1}^{-1}(R_k)\boldsymbol{L}_k(R_k), \tag{A.21}$$

$$\boldsymbol{W}_{k+1} = \boldsymbol{M}_k \boldsymbol{W}_k, \tag{A.22}$$

$$\boldsymbol{W}_{k+1} = \prod_{j=k}^{1} \boldsymbol{M}_j \boldsymbol{W}_1 = \boldsymbol{P}_k \boldsymbol{W}_1. \tag{A.23}$$

Considering $B_{n+1} = 0$, Eq. (A.23) leads to:

$$A_1 = P_{22,n} \frac{A_{n+1}}{P_{11,n}P_{22,n} - P_{12,n}P_{21,n}}, \tag{A.24}$$

$$B_1 = -P_{21,n} \frac{A_{n+1}}{P_{11,n}P_{22,n} - P_{12,n}P_{21,n}}, \tag{A.25}$$

and the coefficients in vector $\boldsymbol{W}_i$ for $i \in [1, n+1]$ are derived as:

$$\boldsymbol{W}_i = \frac{A_{n+1}}{P_{22,n}P_{11,n} - P_{12,n}P_{21,n}} \boldsymbol{P}_{i-1} \begin{bmatrix} P_{22,n} \\ P_{21,n} \\ 0 \\ 0 \end{bmatrix}, \tag{A.26}$$

in $n+1$ layer where the radius is infinite, $B_{n+1} = 0$ and $D_{n+1} = 0$, thus Eq. (A.23) leads to:

$$P_{41,n}P_{22,n} - P_{42,n}P_{21,n} = 0, \tag{A.27}$$

which may be formulated as a quadratic equation that provides directly the effective shear modulus. The missing parameter is $A_{n+1}$ that may be selected arbitrary for the homogenization.